POLITECNICO
MILANO 1863

SCUOLA DI INGEGNERIA INDUSTRIALE
E DELL'INFORMAZIONE

Depth Sensitivity in Diffuse Raman Spectroscopy based on a Time Domain Compressive Sensing approach

Tesi di Laurea Magistrale in
Physics Engineering - Ingegneria Fisica

Author: **Valerio Gandolfi**

Student ID: 970090
Advisor: Prof. Antonio Giovanni Pifferi
Co-advisors: Dr. Alessandro Bossi, Prof. Fabrizio Martelli
Academic Year: 2021-22

Abstract

In many fields, from biomedicine to industry and material research, the problem of analyzing the chemical composition of deep layers of a sample with depth profiling capabilities is often encountered. Diffuse Raman spectroscopy, a recently growing technique which unifies the chemical specificity of Raman Spectroscopy and the penetration depth of Diffuse Optics, allows solving this problem. In fact, it has been already demonstrated that with this technique it is possible to measure Raman spectra of different layers in a multilayered sample. However, a quantification of the probing depth in relation to other measurement parameters, such as time, source detector distance or optical properties of the sample, has not yet been obtained.
In this work, we faced the problem of depth probing in Time Domain Diffuse Raman Spectroscopy. We developed a theoretical model, based on Diffusion Equation, to link the average generation depth of detected Raman photons with their detection time. Simulations derived from the theoretical model were compared to experimental measurements of a bilayered sample obtained with a spectrometer which exploits a single pixel camera and the compressive sensing approach to retrieve both a spectrum and its temporal evolution on a sub-nanosecond scale. This instrument has been improved with respect to a previous version by the addition of a new operation mode to make the alignment more precise and by the integration of all the program code needed to obtain and reconstruct a measure in a unique software which allows a nearly real time monitoring of the instrumentation (refresh rate 0.3 Hz). Thanks to these improvements we have been able to reach a spectral resolution of 0.8 nm. From the comparison of the experimental measurement and the theoretical simulations we can confirm the model developed, although it is not still possible to completely ensure its validity. Nevertheless, our model can be used as a starting point for future developments of depth quantification in Diffuse Raman Spectroscopy.

Keywords: Diffuse Raman Spectroscopy, Raman Spectroscopy, Diffuse Optics, Compressive Sensing, Single-Pixel Camera, Digital Micromirror Device.

Abstract in lingua italiana

In molti campi, dalla biomedicina all'industria e alla ricerca sui materiali, si incontra spesso il problema di analizzare la composizione chimica degli strati in profondità di un campione con una quantificazione della profondità stessa. La spettroscopia Raman nei mezzi diffondenti, una tecnica di recente sviluppo che unisce la specificità chimica della spettroscopia Raman e la profondità di penetrazione dell'ottica diffusa, consente di risolvere questo problema. Infatti, è già stato dimostrato che con questa tecnica è possibile misurare gli spettri Raman relativi ai diversi strati di un campione multistrato. Tuttavia, non è stata ancora ottenuta una quantificazione della profondità da cui proviene il segnale misurato in relazione ad altri parametri di misura come il tempo, la distanza sorgente-rivelatore o le proprietà ottiche del campione.
In questo lavoro, abbiamo affrontato il problema della determinazione della profondità da cui proviene il segnale misurato nella spettroscopia Raman nei mezzi diffondenti nel dominio del tempo. Abbiamo sviluppato un modello teorico, basato sull'equazione di diffusione, per collegare la profondità media di generazione dei fotoni Raman rilevati con il loro tempo di rilevamento. Le simulazioni derivanti dal modello teorico sono state confrontate con le misure sperimentali di un campione a doppio strato ottenute con uno spettrometro che sfrutta una single pixel camera e l'approccio del compressive sensing per misurare uno spettro e la sua evoluzione temporale su una scala inferiore al nanosecondo. Questo strumento è stato migliorato rispetto ad una versione precedente con l'aggiunta di una nuova modalità per rendere più preciso l'allineamento e con l'integrazione di tutto il codice di programma necessario a ottenere e ricostruire una misura in un unico software che permette il monitoraggio della strumentazione quasi in tempo reale (frequenza di aggiornamento 0,3 Hz). Grazie a questi miglioramenti siamo riusciti a raggiungere una risoluzione spettrale di 0,8 nm. Dal confronto tra le misure sperimentali e le simulazioni teoriche possiamo confermare il modello sviluppato, anche se non è ancora possibile assicurarne completamente la validità. Tuttavia, il nostro modello può essere utilizzato come punto di partenza per futuri sviluppi sulla quantificazione della profondità nella spettroscopia Raman in mezzi diffondenti.

Parole chiave: Spettroscopia Raman nei mezzi diffondenti, Spettroscopia Raman, Ottica Diffusa, Compressive Sensing, Single Pixel Camera, Digital Micromirror Device.

Contents

1 | Introduction

A really fascinating aspect of science is the possibility to use light as a mean to investigate materials and get knowledge about their chemical composition and properties in a non-invasive and non-destructive way. What makes this aspect even more interesting are its applications not only to the field of research but also to biomedicine and to industry. In fact, the possibility to analyze or detect a specific material without a mechanical interaction with the sample can be required very often in daily situations: for example, during a non-invasive medical analysis of deep tissues, in a chain process of an industry to check the purity of finished products or in cases in which the contact between the sample could be dangerous for the operator or for the sample itself such as during security controls of potential explosives in airports or during research analysis on art works.

Optical spectroscopy is a branch of science which pioneered the field of non-invasive and non-destructive analysis of materials. Through the years many techniques and instruments have been improved and optimized so as to become today the standard ones for specific analysis. Hence, we have spectrophotometers and absorption spectroscopy that allow determining in an easy and reliable way the contents of an almost transparent sample with low optical absorption. If we need more precise information about the chemical composition, we have Raman spectrometers and Raman emission spectroscopy which allow a precise determination of the chemical species in our material. In case we want to analyze inclusions and internal layers of a turbid and highly diffusive sample, the new instrumentation and measurement techniques of the recently growing field of Diffuse Optics allow detecting light that has travelled deep in the material and gives information about inclusions and internal content of the sample for both spectroscopy and tomographic reconstructions.

Despite the various possible analytic techniques, we are now lacking an analysis method to get the chemical composition in deep regions of turbid materials since Raman Spectroscopy has sensitivity only near the surface of the sample and Diffuse Optical Spectroscopy gives only partial information about the chemical components of the sample. However, in the last years some research groups tried to combine the techniques of Diffuse Optics and Raman Spectroscopy in a union, called Diffuse Raman Spectroscopy

(DIRS), that could be the right way to fill this lack and improve once more the field of Optical Spectroscopy.
In this thesis, after an introduction about Diffuse Raman Spectroscopy, its techniques and applications, we show some theories and theoretical calculations about Time Domain DIRS with a particular attention to depth sensitivity. We present then our novel instrumentation for Time Domain DIRS describing its characteristics and showing its performances in experimental measurements. Finally, we compare the measurements with the theoretical model to verify its validity.

1.1. Overview of Diffuse Raman Spectroscopy

Before facing the theory and principles of Diffuse Raman Spectroscopy, we need to introduce, in the next sections, some concepts of Diffuse Optics and Raman Spectroscopy. In the following, we will see how and why the union of these two techniques in Diffuse Raman Spectroscopy can be so effective and important to advance the frontiers of Optical Spectroscopy.

1.1.1. Diffuse Optics

With Diffuse Optics we refer to the field of optics which deals with the propagation of light in turbid media. These types of media, also known as diffusive materials, are characterized by a high scattering coefficient and a relatively low absorption coefficient so that they look opaque. These characteristics are due to the structure of turbid media: in fact, they typically consist in a background medium with its own absorption and scattering properties in which a big number of diverse particles are included. These particles have different refractive index than the background medium thus light does not travel a straight line but, according to the law of refraction, it is deviated at each of their boundaries producing a complex path and leading to a high scattering coefficient, as shown in Figure 1.1.
The study of turbid media is very important because many materials such as plastics, wood, rocks and even human tissue can be classified under this category.
The particularity of diffusive media is that, because of the multiple deviations of light, the propagation of light inside them is very difficult to be modelled with Maxwell equations and electromagnetic waves: in fact, the model of Radiative Transfer is used and light is treated in a corpuscular way, as a flow of photons.
The Radiative Transfer model is derived from the more general Boltzmann Transport Theory to describe the photon migration inside turbid media. Its fundamental equation

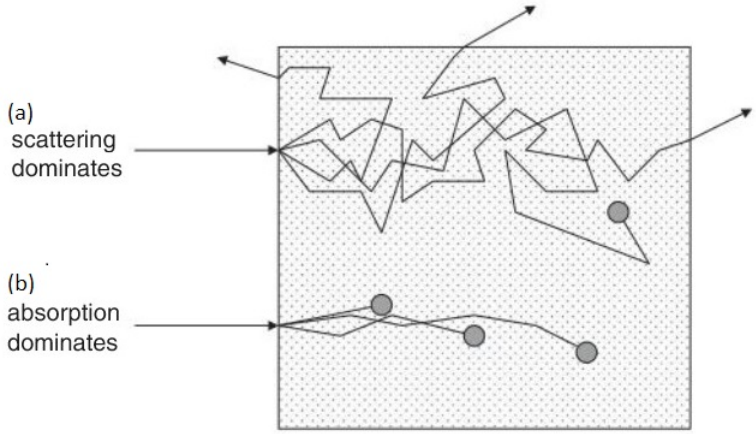

Figure 1.1: Light propagation paths for high scattering (a) and low scattering (b) [1]

is the Radiative Transfer Equation (RTE) that describes how the radiance $I(\vec{r}, \hat{s}, t)$, defined as the average power of light at time t in a specific point $\vec{r}$ with a specific direction $\hat{s}$, evolves in the medium, given a light source $q(\vec{r}, \hat{s}, t)$ and the properties of the medium, namely absorption and scattering [2].

$$\begin{aligned}\frac{\partial}{\partial t}\frac{I(\vec{r}, \hat{s}, t)}{v} = -\nabla \cdot [\hat{s} I(\vec{r}, \hat{s}, t)] - (\mu_a + \mu_s) I(\vec{r}, \hat{s}, t) + \\ + \mu_s \int_{4\pi} p(\hat{s}, \hat{s}') I(\vec{r}, \hat{s}', t) d\hat{s}' + q(\vec{r}, \hat{s}, t)\end{aligned} \tag{1.1}$$

To model the absorption in the RTE we use the absorption coefficient μ_a which is defined as the probability that a photon is absorbed after travelling an infinitesimal path (note that the definition of the absorption coefficient from Lambert-Beer's law is still valid but we need to consider the complex path travelled by the photon rather than a straight line). To model the scattering, we use the scattering coefficient μ_s, defined as the probability that a photon is scattered after travelling an infinitesimal path, and the phase function $p(\hat{s}, \hat{s}')$, which represents the probability that a photon is deflected with a certain angle in a scattering event.
Although the RTE is very powerful, it has no analytical solution for a general case and it is usually approximated with a simpler form, called Diffusion Equation (DE), which can be solved analytically, in particular geometries.

$$\left(\frac{1}{v}\frac{\partial}{\partial t} - D\nabla^2 + \mu_a\right)\Phi(\vec{r}, t) = q(\vec{r}, t) \tag{1.2}$$

Note that in this equation the quantity of interest is the fluence $\Phi(\vec{r}, t)$ which is defined as

the average power of light at a certain time in a specific point of the space in all directions. Fluence is obtained by integrating radiance over the entire solid angle.

$$\Phi(\vec{r}, t) = \int_{4\pi} I(\vec{r}, \hat{s}, t) d\hat{s} \tag{1.3}$$

The properties of the medium are embodied by the absorption coefficient μ_a and the diffusion coefficient D defined as

$$D = \frac{1}{3\mu_s'} \tag{1.4}$$

The coefficient μ_s' is called reduced scattering coefficient and is equal to $g(1 - \mu_s)$ where g is the anisotropy factor, a pure number which represents the average angle of deflection during a single scattering event, calculated as $g = \langle \cos\theta \rangle$.

It is important to remember that the approximation of DE is valid only if scattering is much higher than absorption and if the light flux in the medium does not change abruptly in time. However, fortunately, these requirements are satisfied for many plastics and for human tissues allowing the use of DE to describe the propagation of light in real situations.

We have then the possibility to use this theory both as a forward model to predict the propagation of light in a certain medium or, more interestingly, as an inverse model to determine the characteristics of the material (namely absorption and scattering coefficients) from measurements of light that propagated inside the medium.

In this last case, two main approaches of measurement are possible: Continuous Wave and Time Domain.

In Continuous Wave (CW) approach a constant (not-time varying) light, usually from a laser, is delivered to the sample and collected at a certain distance from the injection point. The attenuation of light gives information about absorption and scattering coefficients of the material while the variation of the distance between the injection and the collection point allows selecting photons that have travelled at different depths in the medium. Although the simplicity, in this modality it is not possible to obtain both the absorption and the scattering coefficient from a single measurement but we need to take many measurements at different source-detector spatial offsets or with different wavelengths.

In Time Domain (TD) approach a pulsed laser provides a train of pulses that is delivered to the sample and collected with fast detectors or Time Correlated Single Photon Counting (TCSPC) technique. The material will broaden each pulse and will change its shape depending on its absorption and scattering properties. The analysis of the detected

pulse shape, thanks to the theoretical model of DE, gives independently the absorption and scattering coefficients with a single measurement at the cost of a more complex instrumentation. Moreover, since from theory we know that photons arriving later at the detector (late photons) have a greater probability to come from deeper layers of the sample than the first detected photons (early photons), selecting a time gate on the measurement allows isolating the signal coming from different layers of the sample.
Whatever the measure approach is, the field of Diffuse Optics can be divided into subfields depending on the final aim of the measurement.
Diffuse Optical Spectroscopy (DOS) refers to the measure of absorption and scattering coefficient locally and their variation with the wavelength. This type of measurement allows identifying the average composition of a material, according to the absorption bands in the spectrum, and the average size of particles, according to the scattering variation with wavelength.
Diffuse Optical Imaging (DOI) and Diffuse Optical Tomography (DOT) indicate instead the measure of the spatial variation of optical properties in two or three dimensions respectively. This allows obtaining 2D or 3D maps of the inclusions present in the sample.
Summing up, Diffuse Optics has the big advantage of analyzing the depth of a material in a non-invasive and non-destructive way with imaging and tomographic opportunities. However, as main disadvantage, it is possible to retrieve only an average chemical composition and often the high scattering reduces so much the signal that becomes very difficult to obtain a reliable measurement.

1.1.2. Raman Spectroscopy

Up until now, we considered only elastic scattering: meaning that scattered light has the same wavelength λ and frequency ν of incident light. However, scattered light can have a different wavelength than incident light, in this situation we speak of inelastic scattering. This is the case of Raman effect, firstly reported in 1928 by the Indian physicist Chandrasekhara Venkata Raman, who won the Nobel prize in 1930 because of this discovery and gave birth to Raman Spectroscopy. This spectroscopy technique aims at measuring the spectrum of inelastically scattered light by Raman effect and identify the composition of a material according to the measured spectral features.
Since the inelastic scattering of Raman effect is due to the interaction between light and molecules, in particular molecular vibrations, in order to have a better understanding of this effect, we need to introduce some concepts of Molecular Physics, that branch of Physics which deals with physical properties of molecules and molecular dynamics.
We need to start from the quantum mechanical description of a molecule according to

which a stationary state of a molecule is defined by the time independent Schrödinger's equation involving the Hamiltonian $H(\vec{r},\vec{R})$ of the whole molecule, representing the total energy E_{TOT}, and the wavefunction $\Psi(\vec{r},\vec{R})$, representing the state of the molecule, namely the position of electrons $\vec{r}$ and nuclei $\vec{R}$.

$$H(\vec{r},\vec{R})\Psi(\vec{r},\vec{R}) = E_{TOT}\Psi(\vec{r},\vec{R}) \tag{1.5}$$

The Hamiltonian of the molecule is given by the sum of the kinetic energy of electrons T_e and nuclei T_n and the potential energy of the nuclei-nuclei V_{nn}, electron-electron V_{ee} and electron-nuclei V_{en} interactions.

$$H(\vec{r},\vec{R}) = T_e(\vec{r}) + T_n(\vec{R}) + V_{ee}(|\vec{r_{ij}}|) + V_{en}(\vec{r_i},\vec{R_j}) + V_{nn}(|\vec{R_{ij}}|) \tag{1.6}$$

Thanks to the Born-Oppenheimer approximation, which states that the electronic motion and the nuclei motion can be considered independent because of the mass difference of these particles ($m_n >> m_{el}$), the equation (1.5) can be divided in two separated equations.

$$[T_e(\vec{r}) + V_{ee}(|\vec{r_{ij}}|) + V_{en}(\vec{r_i},\vec{R_j})]\Psi_{el}(\vec{r};\vec{R}) = E_{el}\Psi_{el}(\vec{r};\vec{R}) \tag{1.7}$$

$$[T_n(\vec{R}) + V_{eff}(|\vec{R_{ij}}|)]\Psi_n(\vec{R};\vec{r}) = E_n\Psi_n(\vec{R};\vec{r}) \tag{1.8}$$

The first one involves only the electrons and solving it one finds the electronic states of the molecule. There are many quantized states, each one with a precise energy, like the electronic states one obtains for an atom.
However, to explain the Raman effect, we are more interested in equation (1.8), which involves only the nuclei with a parametric dependence on the positions of electrons. By fixing an electronic state, it is possible to solve the equation for the nuclei for that fixed electronic configuration. Considering that the function for V_{eff}, which involves the nuclei-nuclei V_{nn} and electrons-nuclei V_{en} interactions, can be approximated with a harmonic potential ($1/2m\omega^2|\vec{R}|^2$), this equation has the same form of the quantum harmonic oscillator one (1.9). So we obtain a set of harmonic oscillators as solution each one for a different value of E_n.

$$\Big(-\frac{\hbar^2}{2m} + \frac{1}{2}m\omega^2|\vec{R}|^2\Big)\Phi(\vec{R}) = E\Phi(\vec{R}) \tag{1.9}$$

These oscillators represent the vibrations of the molecule also called vibrational states. There are 3N-6 (3N-5 for a linear molecule) vibrational states, where N is the number of atoms in the molecule, each one corresponding to a specific collective oscillatory motion of the nuclei with a certain frequency and energy.
Summing up, quantum mechanics tells us that a molecule can be represented schematically by a set of electronic states each one composed of a set of vibrational states: these are the unique states and energies the molecule can assume. Usually we exploit a representation like the one in Figure 1.2.

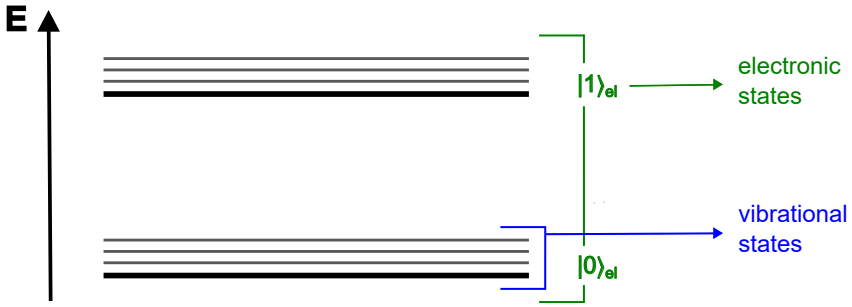

Figure 1.2: Energy levels diagram for a molecule

In normal conditions, at room temperature and when no energy from an external source is supplied to the system, almost all the molecules are in the lowest energetic level called ground state. Only a few molecules can be found in higher levels because of thermal effects.
When we excite the system with an external source of energy, for example light in our case, some molecules can absorb energy and reach higher energy states. The mechanism and rules according to which the transitions occur are described by the theory of Second Order Perturbations. Nevertheless, this theory would lead to very complex calculations we are not going to analyze as, to give a rough explanation of the Raman effect, it is sufficient to use the elements we introduced up to now.
As we said before, by shining light on our sample the molecules can absorb a photon and reach an excited state. If the energy of the incoming photon $E_{ph} = h\nu_0 = hc/\lambda_0$ is different than any gap between energetic levels of the molecule, the transition brings the molecule in a virtual excited state. In any case, this is an unstable condition and the molecule will find a way to release energy, typically by emitting a photon, and return to the ground state.
There are now different possibilities for the de-excitation, shown in Figure 1.3.
If the molecule returns directly to the starting state, it will emit a photon with the same

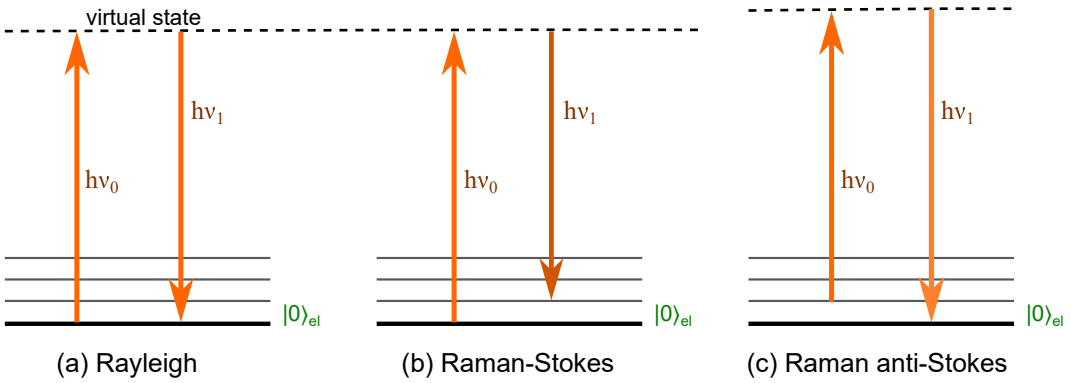

Figure 1.3: Diagram of photon absorption and emission in case of Rayleigh scattering (a), Raman-Stokes scattering (b) and Raman anti-Stokes scattering (c)

energy of the incoming one ($h\nu_1 = h\nu_0$). This is the Rayleigh effect or elastic scattering explained with a quantum description.
More interestingly, if the molecule decays in a higher energy level than the starting one, a photon with lower energy than the incident photon ($h\nu_1 < h\nu_0$) will be emitted: this is the case of inelastic scattering or Raman-Stokes effect. At the end of the process the molecule is in an excited vibrational state and it will decay to the ground state because of thermal relaxation.
There is also the possibility that a molecule initially not in the ground state absorbs the incoming photon, is brought to a virtual excited state and then decays to the ground state. The emitted photon will have higher energy than the incoming one ($h\nu_1 > h\nu_0$): this is also a case of inelastic scattering called Raman anti-Stokes effect. However, the probability of this event is very small since in normal conditions only very few molecules are not in the ground state.
The difference between the wavelength of impinging light λ_0 and the wavelength of the emitted one λ_1 is called Raman shift and it is the main object of interest for Raman Spectroscopy. It is worth to note that this quantity is independent of the wavelength of excitation light and depends only on the vibrational energy levels of the molecule.
In Raman spectroscopy it is typical to express frequencies or wavelengths with a particular quantity called wavenumber measured in cm^{-1} and defined as:

$$\tilde{\nu} = \frac{\nu}{c} = \frac{1}{\lambda} \tag{1.10}$$

so the Raman shift is:

$$\Delta\tilde{\nu} = \left(\frac{1}{\lambda_0} - \frac{1}{\lambda_1}\right) \tag{1.11}$$

Raman spectroscopy consists then in exciting a sample with a monochromatic light, collecting the spectrum of light emitted for Raman effect and identifying the composition of our sample by evaluating the Raman shifts of the peaks. In fact, since different peaks encode Raman-Stokes transitions between the virtual state and different vibrational energy levels of a molecule and since vibrational states are distinct for different molecules, it is possible to identify the chemical species in the sample in analysis.

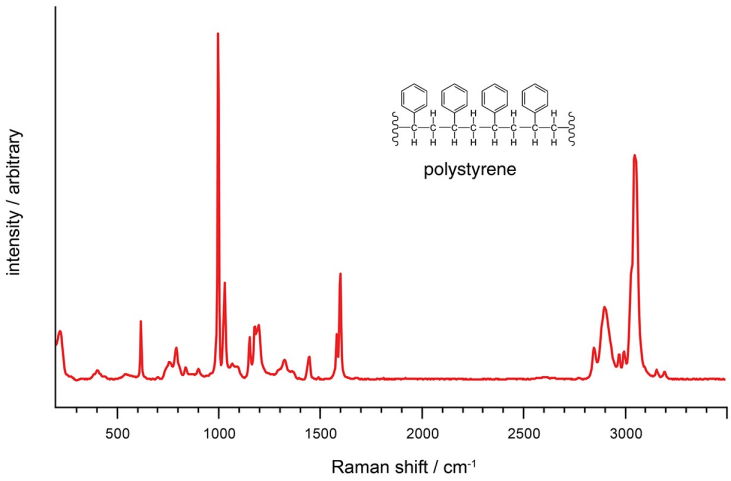

Figure 1.4: Example of Raman spectrum of polystyrene taken from renishaw.it

In particular the region between 300 and 1900 cm^{-1} is called fingerprint region because it contains the spectral lines related to transitions which allow the discrimination between different types of molecules and the univocal identification of the chemical composition of the sample.

In conclusion, although Raman scattering is a valid and powerful tool for a precise analysis of materials, it has also some difficulties to be considered during measurements.

First of all, its efficiency is very low: in fact, approximately only one photon over a million is converted by Raman effect so the intensity of Raman scattered light is very low and high excitation power or high sensitivity detectors are often needed.

Moreover, this high power also enables a competitive phenomenon with Raman scattering: fluorescence.

Fluorescence is due to the emission of a photon when a molecule decays from an excited electronic state to the ground electronic state. Because of selection rules which govern the transitions between energy levels, also the light of fluorescence gives photons with lower energy than impinging ones. Thus fluorescence can contaminate the signal of Raman scattering. Then it is important to choose carefully the excitation wavelength and power in order to reduce the contamination of fluorescence.

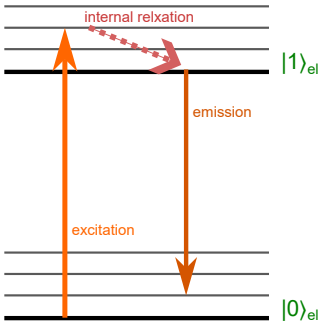

Figure 1.5: Diagram of the phenomenon of fluorescence

1.1.3. Diffuse Raman Spectroscopy

The background idea of Diffuse Raman Spectroscopy is to exploit the theory and the techniques of Diffuse Optics in order to observe Raman scattered light coming from deep layers in a material. In fact, since Raman scattering occurs anywhere the material receives light, if we consider a turbid medium, there will be Raman photons generated in depth because of the elastic diffusion of light in the material. These generated photons will propagate in the material according to Diffusion theory and they can be detected with Diffuse Optics techniques. The Raman photons will bring information about the place where they were generated so we can identify the chemical composition of different layers of our sample by isolating the Raman spectra of each layer. Moreover, Diffuse Optics also enables the possibility to do a tomographic reconstruction thus obtaining a tridimensional model in which it is possible to distinguish the chemical composition of different zones in the material.
However, even though Diffuse Raman Spectroscopy can make feasible novel and interesting types of measurements, there are some experimental difficulties which hinder its fast development. The main one is that the signal is very low. In fact, Raman effect has itself a low efficiency and the diffusion in the turbid medium decreases even more the detectable signal. Moreover, the signal from deeper layers is often overcome by Raman signal or fluorescence from the surface making the identification of these layers very challenging.

1.2. DIRS Techniques

Although the instrumentation for Diffuse Raman Spectroscopy always involves a laser source, optical systems to deliver and collect light from the sample, a spectrometer and a detector, one can use different techniques of measurement. In this section the DIRS techniques explored over the years as well as those at the state of art are presented.

1.2.1. SORS

Spatially Offset Raman Spectroscopy (SORS), firstly demonstrated by Matousek et al. in 2005 [3], is nowadays the most diffused and most developed DIRS technique.
This technique is able to provide Raman spectra of deep layers of a medium by collecting reflectance measurements at different source-detector distances (or spatial offsets) with a monochromatic CW laser focused on the surface of the sample.
The underlying principle of this technique is that, increasing the spatial offset between source-detector, because of the properties of random walk of photons in diffusive media, one collects photons which have travelled longer in the medium both in terms of space and time, so, on average, they had more scattering events and reached deeper regions than photons collected at small source-detector distance. For this reason, at a large spatial offset, it will be more likely to observe Raman photons generated in the deepest layers of the material than those generated near the surface.
The *original configuration of SORS* consists of a point illumination by a CW laser focused on the sample and a point collection at different distances from the light injection point. An alternative, already proposed in the first demonstration of SORS [3], is a ring detection scheme in which photons are collected from concentric rings with variable radius around a unique light injection point.
Since the first demonstration many variations of the original experimental scheme have been explored with the aim of tailoring SORS to various applications:

- *inverse SORS*: "inverse" refers to the inversion of the illumination and collection regions with respect to original SORS. In fact, in inverse SORS an axicon is exploited to spread the illumination over a ring centered on a point where an optical system or a fiber collects the signal. Changing the position of the axicon, the radius of the illumination ring changes thus giving different source-detector spatial offsets. This technique allows having lower illumination power on the sample by spreading the laser power on a larger area than on a point, thus being suitable for applications where a maximum power limit is fixed such as the medical field [4];

- *transmission Raman spectroscopy (TRS)*: this is a particular case of SORS in which the light injection point and the collection one are at opposite sides of the sample. This configuration, instead of a layer analysis, allows a volume analysis of the whole chemical composition of the sample [5];

- *surface-enhanced SORS (SESORS)*: in this technique the depth profiling capability of SORS is used to detect the enhanced Raman effect, given by surface plasmon resonance, of metallic nanoparticles injected in the sample. As a consequence, the

maximum achievable depth is increased (up to 5 cm) and, since the nanoparticles can be designed to bind with specific molecules, also chemical selectivity and sensitivity are improved. In addition, SESORS imaging has been demonstrated thus enabling, not only the detection, but also the localization of a specific molecule inside the sample [6, 7];

- *micro-SORS*: by passing both the illumination and detection beam in a microscope objective, micro-SORS reduces the scale of SORS to tens of micrometers, thus allowing the analysis of the stratification of thin scattering layers with different chemical composition [8];
- *stand-off SORS*: "stand-off" refers to the distance between the instrumentation for the measurement and the sample. In fact, it was demonstrated that inserting a telescope in the SORS scheme allows taking the measurement of a sample at a distance of more than 10 m [9].

It is worth to point out that there are also *commercially available SORS instruments* already used by many companies, in particular in the field of pharmaceutics, and by security officers at airports. The main producer is Cobalt Light Systems Ltd, founded in 2008 from a startup by Matousek's laboratory and now part of Agilent Technologies Inc which acquired it in 2017. Only a few other companies managed to enter the market of SORS instruments because Cobalt and Agilent own many patents for SORS and its variations [10, 11].
As we saw, SORS requires a quite simple instrumentation but it also suffers from some important limitations. The first is a worsening of spatial resolution and S/N ratio when the spatial offset is increased that hampers a tomographic reconstruction. The second is a low rejection of fluorescence and signal from the surface so that measurements need a mathematical processing to retrieve the pure Raman spectrum of a single layer.

1.2.2. FORS

Frequency-offset Raman Spectroscopy (FORS) is a DIRS technique demonstrated by Sekar et al. in 2017 [12].
The technique is able to provide Raman spectra of deep layers exploiting a CW laser beam, operated at different wavelengths (or frequencies), to take reflectance measurements on the sample. In contrast to SORS, here the source-detector distance is fixed and the capability of depth profiling is given only by the different wavelengths used. This solves the limitations of SORS on spatial resolution and on the variation of S/N ratio with the spatial offset, so that FORS is able to give better measurements than SORS.

The principle that makes FORS work has to be found in the dependence of optical properties (absorption and scattering) of a medium on the wavelength of the incident light. In fact, changing the wavelength of the incident light involves a change in the optical properties, thus also the propagation of photons in the medium is different. For example, if one sets a wavelength for which the absorption of the medium is lower with respect to another wavelength, the injected photons will go deeper and Raman photons from a deeper layer will be collected. Then, choosing an appropriate set of wavelengths it is possible to do a depth profiling of the chemical composition of the sample and retrieve the Raman spectra of the different layers.
However, there are several limitations of FORS. The first and most important is that absorption and scattering coefficients of the sample and their dependence on wavelength must be known before the measurement and, in particular, a strong dependence of these coefficient on wavelength is needed to reach an effective depth sensitivity. Then, once the measurement is taken, forward models based on the Diffusion Equation are needed to retrieve the Raman spectrum, instead of the simpler algorithms used in SORS. Secondly, there is an increased complexity of the instrumentation that needs to work with different wavelengths. And lastly, there is still a contribution of fluorescence from the sample which contaminates the measure and that could be also greater than in SORS because of the use of more than one wavelength.
Probably due to these limitations, in particular the first one which requires an additional previous measure on the sample, there have been no further research on FORS.

1.2.3. TD-DIRS

With Time Domain Diffuse Raman Spectroscopy (TD-DIRS) we identify all the techniques that involve a pulsed laser source and a time domain measurement to retrieve the Raman spectra at different depths.
The principle at the basis of these techniques is that in a time domain measurement of reflectance the photons detected at late times come on average from a deeper region of the sample. So, by gating the signal at different delays it is possible to collect Raman photons coming from different depths and retrieve the Raman spectra of those layers of our sample.
There are many possible approaches to this technique:

- *Kerr gating*: this is the first approach in this field, demonstrated by Matousek et al. in 2005, where a fast optical Kerr gate (4 ps) is used to collect only a small portion of the temporal signal [13];

- *gated ICCD*: in this approach the temporal gate is obtained by varying the gain of an intensified CCD camera (ICCD). This approach has a longer gate (250 ps) and then a lower temporal resolution than the first one. However, the retrieval of Raman spectra at different depths is still possible and with a much simple instrumentation than a Kerr gate [14];
- *TCSPC*: the Time Correlated Single Photon Counting allows collecting both temporal and spectral information in a single measurement. The whole temporal curve is registered and the gating can be applied during post-processing of data. The spectral information is collected thanks to a particular TCSPC camera [15], an array of detectors [16] or a compressive sensing system with a single pixel detector [17] (this last approach is the one exploited also in this thesis).

Thanks to gating, the TD-DIRS technique gives a better suppression of fluorescence than SORS and allows retrieving the pure Raman spectra of deep layers without applying any algorithm to the measurements. Moreover, the contrast between different layers is much higher with respect to the other techniques.
As a drawback, the instrumentation is more complex than that required by SORS and that is why over the years there have been only a little research on TD-DIRS systems. However, during the recent years, thanks to the new technologies of TCSPC and compress sensing, the instrumentation has become simpler and the interest in TD-DIRS has increased again.

1.2.4. Hybrid techniques

For completeness, here are reported some hybrid techniques coming from the combination of some previous approaches:

- *SORS + FORS*: in this combination a FORS measurement is taken also at different spatial offsets of source and detector. This improves the S/N ratio with respect to SORS and FORS both [12];
- *SORS + TD-DIRS*: this combination consists in a TD-DIRS measurement with a ICCD camera taken at different spatial offsets. The spatial offset allows a better depth selectivity than the pure TD-DIRS ICCD measurement [18].

1.3. Applications of DIRS

The ability of DIRS to provide information about the chemical composition of deep layers of a material in a non-invasive way finds plenty of applications in many fields. For now, SORS and its derivative techniques have been the most studied and tested for applications,

however, FORS and TD-DIRS can be easily adapted to the same applications. The next subsections report the main fields of application of DIRS and each one contains the main research explored in that particular field.

1.3.1. Medicine

DIRS can give a big advance in the field of Medicine, in particular in diagnostics, making many analyses less invasive, improving the precision of other ones and enabling innovative measurements. SORS and SESORS are the techniques mainly applied in this field and the main applications explored are [19]:

- analysis of bone tissue in a non-invasive way allowing the identification of organic and inorganic components to monitor bone strength and detect diseases such as osteoporosis at early stages;
- quality assessment of blood in transfusion bags before the transfusion for improving the control and safety of this practice;
- detection of cancer and margins analysis after surgical treatment of cancer, in particular for breast cancer, with a higher sensitivity and less harm than actual techniques;
- detection of neurotransmitters for monitoring mental and physical conditions like schizophrenia and Parkinson's disease;
- measuring changes in temperature and pH in deep tissue: a very important information to have feedback during photo-thermal therapy.

Since only a few of these applications were experimented in vivo and none of them reached the clinical environment, the actual research in the medical field aim at filling these lacks.

1.3.2. Pharmaceutics

The field of Pharmaceutic industry experienced a great benefit from DIRS: SORS and TRS have been demonstrated as very reliable techniques for controls on drugs and their production. Explored applications concern:

- analysis of packed raw materials at the beginning of the production of a drug in a non-invasive and rapid way for preserving the package integrity and increasing the throughput of controls [20];
- detection of intrusions in packed drugs at the end of the production allowing controls without opening the package [5];

- detection of counterfeits without need to extract the drugs from their package [21];
- through-package quantification of components [22, 23].

The success of these studies led to the development of commercial devices and its diffusion in many pharmaceutic industries [10].

1.3.3. Defense and Security

The ability of detecting a substance in a package without opening or even touching it makes DIRS a very suitable technique for applications in the field of Defense and Security. This allows the personnel to avoid the direct contact of hazardous substances as well as the contamination of a possible evidence in investigations. SORS and stand-off SORS are the main techniques used in this field for [24, 25]:

- detection of explosives;
- detection of chemical warfare agents (CWAs);
- detection of illegal drugs.

Commercial devices have been already developed for these applications and are nowadays employed for security controls at airports or similar structures [10].

1.3.4. Cultural Heritage

DIRS can give an important help in studying and preserving Cultural Heritage. With DIRS it is possible to do a layer analysis of the artwork obtaining, not only information about the technique of the artist, but also knowledge of the materials used in order to better define the conservation strategy. Micro-SORS has found a solid application in this field to accomplish common problems in Cultural Heritage like [26]:

- painted stratigraphies;
- hidden paintings or drawings covered by a superimposed layer;
- layers covered by other intensely fluorescing layers.

A lot of demonstrations have been carried out both on real sculptures or paintings and on mock-up samples giving successful results. Recent developments aim at building a portable system which allows in situ measurements even in not optimal conditions thus avoiding completely the removal of samples from art pieces.

1.3.5. Food and Beverages

This field experienced a great increase only in the recent years, that probably goes together with the growing interest in sustainability and food. DIRS can be used to obtain through-package analysis for quality assurance, quality control and authentication of food and drinks. In particular, SORS has been demonstrated to succeed in [10]:

- estimate the grade of maturity of fruits;
- detect contaminants in food;
- assess the quality of fish and meat;
- distinguish different cuts of meat or varieties of potatoes;
- verify the authenticity of spirit drinks or Protected Denomination of Origin (PDO) foodstuffs.

Further research is going also towards the detection of diseases in food crops by measurements taken on leaves or seeds. However, although all of these applications can easily find an arrangement in the food industry, SORS is not yet largely diffused in this field. Probably, this is due to the fact that SORS is still an emerging technique and it is not ready to substitute other consolidated techniques of food industry.

1.4. Overview of the thesis work

After the previous introduction about the general topic of this thesis work, now we present an overview of the work done during the thesis period as well as a picture of the organization of the thesis itself.
The thesis work consisted in three main parts:

- the study of the theoretical models to describe Diffuse Raman and the development, for the first time, of an approach, based on these models, to determine the average depth of the detected signal with respect to detection time (Chapter 2)
- the improvement of the instrumentation used, a system for Time Domain Diffuse Raman Spectroscopy based on a spectrometer made of a time domain single pixel camera, and its characterization after the improvements (Chapter 3)
- the validation of the instrumentation and the developed theoretical model through experimental measurements of different samples (Chapter4)

Chapter 5 collects the final conclusions of our work and some future perspectives.

2 | Theoretical Elements

Some theoretical descriptions for Diffuse Raman, in particular in Time Domain, have already been given, nevertheless there are many interesting theoretical aspects which remain unexplored. One of these is the link between the time or the source-detector distance to the depth at which detected Raman photons are generated.
In this chapter we report a recent and rigorous model to describe Diffuse Raman, based on the Diffusion Equation, that we will then use to calculate the average generation depth of detected Raman photons.
In the following we will always consider only the Time Domain case. The theory for CW can be obtained by integrating over time the formulas for Time Domain.

2.1. Diffuse Raman model

The theoretical description of Diffuse Raman is based on what was developed by Martelli et al. in reference [27].
This approach directly analyzes the propagation of light in the medium as shown in figure 2.1. Raman photons are generated by excitation photons that have been diffused in

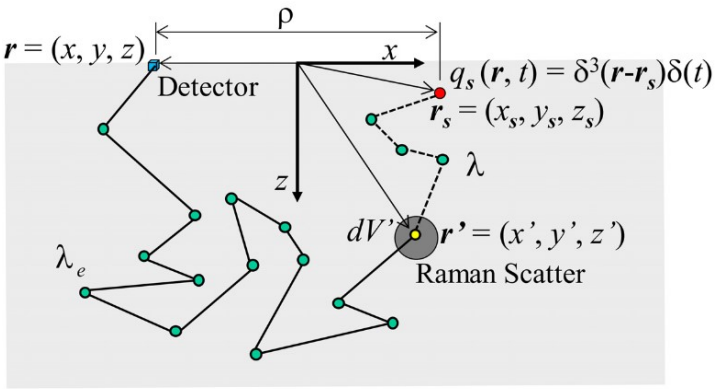

Figure 2.1: Propagation of Rayleigh and Raman photons in a medium (figure from [27])

the material and, after generation, they will in turn diffuse in the material before being detected. For this reason the model is based on two coupled diffusion equations: one for

the propagation of photons injected in the material (2.1a), the other for the propagation of Raman photons generated by those injected photons (2.1b).

$$\begin{cases} \left(\frac{1}{v}\frac{\partial}{\partial t} - D\nabla^2 + \mu_a\right)\Phi(\vec{r},t) = q(\vec{r},t) & \text{(2.1a)} \\ \left(\frac{1}{v_e}\frac{\partial}{\partial t} - D_e\nabla^2 + \mu_{ae}\right)\Phi_e(\vec{r},t) = q_e(\vec{r},t) & \text{(2.1b)} \end{cases}$$

These two diffusion equations deal with two different wavelengths: λ for injected photons and λ_e for Raman photons. Note that refractive index, absorption coefficient and scattering coefficient, because of their dependence on the wavelength, assume different values in the two equations. n_i, μ_{ab}, μ'_{sb} indicate the properties of the background medium at wavelength λ while n_{ie}, μ_{abe}, μ'_{sbe} indicate the properties of the background medium at wavelength λ_e. As a consequence there are two different diffusion coefficients D and D_e respectively calculated as $1/3\mu'_{sb}$ and $1/3\mu'_{sbe}$ and two different photon propagation velocities v and v_e, calculated respectively as c/n_i and c/n_{ie} with c the speed of light.
In the first equation Raman scattering is considered equivalent to an absorption event since it subtracts photons at wavelength λ. For this reason, the absorption coefficient is calculated as $\mu_a = \mu_{ab} + \mu_{sR}$. μ_{sR} is the Raman scattering coefficient and is equal to the probability to have a Raman scattering event in an infinitesimal path length.
In the second equation, instead, Raman scattering is considered in the source term q_e which couples the two equations and represents the conversion of photons for Raman effect. In fact, this term depends both on μ_{sR} and on the fluence of injected photons $\Phi(\vec{r},t)$, that can be calculated from the first equation. Its expression is:

$$q_e(\vec{r},t) = \mu_{sR}\Phi(\vec{r},t) \tag{2.2}$$

With this model it is possible to derive, by means of the Green's function method, the solution of Raman signal for any desired geometry either if the Raman scattering centers are homogeneously distributed in the medium or concentrated in a restricted region.
The validity of this model has been confirmed by Monte Carlo simulations reported in the same article [27] and it is strengthened by the fact that from this model it is possible to derive and justify the first theoretical description of Diffuse Raman, based on a heuristic approach, developed by Everall et al. in reference [28].
In fact, considering the optical properties of the medium seen by Raman photons at λ_e equal to that at wavelength λ of injected photons (meaning that Raman photons propagate as Rayleigh scattered photons) and applying the scaling properties of DE for the absorption coefficient, it is possible to calculate the Raman fluence as the difference

of Rayleigh fluence without and with Raman scattering.

$$\Phi_e(\vec{r},t) = \Phi(\vec{r},t) - \Phi(\vec{r},t)\exp\{-\mu_{sR}vt\} \tag{2.3}$$

Considering the very small value of μ_{sR} (typically 10^{-6} mm^{-1}) the equation (2.3) can be approximated with

$$\Phi_e(\vec{r},t) \approx \Phi(\vec{r},t)\mu_{sR}vt \tag{2.4}$$

This last expression allows calculating the Raman signal from the Rayleigh one multiplied by $\mu_{sR}vt$ and it has the same form of that obtained by Everall et al. in their heuristic model [28]. Thus, we can consider this as a simplified Diffuse Raman model valid when optical properties of the medium do not vary much with respect to wavelength.

2.1.1. Solution for semi-infinite medium

To give a better insight of this theoretical model for Diffuse Raman, we will calculate as example the solution for the Raman signal in the case of a point-like instantaneous injection source and a semi-infinite homogeneous medium.
Starting from equation (2.1a) the solution for the fluence can be obtained, according to the Green's function method, from the convolution of the source term and the Green's function of the problem. Since the considered source is point-like and instantaneous $q(\vec{r},t) = \delta(\vec{r})\delta(t)$, the solution for $\Phi(\vec{r},t)$ is directly the Green's function $G(\vec{r},t)$ of the semi-infinite medium.

$$\Phi(\vec{r},t) = G(\vec{r},t) * \delta(\vec{r})\delta(t) = G(\vec{r},t) \tag{2.5}$$

The solution of the second equation, namely the fluence of the Raman signal, is then obtained with the same method, using equation (2.2) for the source term $q_e(\vec{r},t)$.

$$\begin{aligned}\Phi_e(\vec{r},t) = G_e(\vec{r},t) * q_e(\vec{r},t) = G_e(\vec{r},t) * \mu_{sR}G(\vec{r},t) = \\ = \mu_{sR}\int G_e(\vec{r},\vec{r'},t,t')G(\vec{r'},t')\end{aligned} \tag{2.6}$$

So $\Phi_e(\vec{r},t)$ is the convolution of two Green's functions. We have to use for both the Green's TD function for the semi-infinite medium but we must pay attention to the variables in the convolution integral. In fact, the function for Raman signal depends on the coordinate $\vec{r}$ and the convolution variable $\vec{r'}$ while the function of Rayleigh scattered light depends on the convolution variable $\vec{r'}$ and the position of the excitation source, that in this case does not appear because it coincides with the origin of the reference system.
As Green's function for semi-infinite medium we will use:

$$G(\vec{r},t) = \frac{v}{(4\pi Dvt)^{3/2}} \exp\left\{-\frac{x^2+y^2}{4Dvt} - \mu_a vt\right\} \times \\ \times \left[\exp\left\{-\frac{(z-z_0^+)^2}{4Dvt}\right\} - \exp\left\{-\frac{(z-z_0^-)^2}{4Dvt}\right\}\right] \tag{2.7}$$

with

$$z_0^+ = z_S \\ z_0^- = -z_S - 2z_E \tag{2.8}$$

This solution was derived with the method of images and extrapolated boundary conditions (EBC) so in equations (2.8), z_S represents the source depth and z_E the extrapolated boundary where the fluence goes to zero. Typically $z_E = 2AD$ where A is a coefficient to take into account the refractive index mismatch at the surface of the medium but for simplicity we will consider $A = 1$ and $z_E = 2D$.
Substituting the Green's function in the integral we obtain:

$$\Phi_e(\vec{r},t) = \int \frac{\mu_{sR} v v_e}{(16\pi^2 D D_e v v_e)^{3/2}} \frac{1}{(t'(t-t'))^{3/2}} \exp\left\{-\frac{x'^2+y'^2}{4Dvt'} - \mu_a vt'\right\} \times \\ \times \exp\left\{-\frac{(x-x')^2+(y-y')^2}{4D_e v_e(t-t')} - \mu_{abe} v_e (t-t')\right\} \times \\ \times \left[\exp\left\{-\frac{(z'-z_0^+)^2}{4Dvt'}\right\} - \exp\left\{-\frac{(z'-z_0^-)^2}{4Dvt'}\right\}\right] \times \\ \times \left[\exp\left\{-\frac{(z-z_1^+)^2}{4D_e v_e(t-t')}\right\} - \exp\left\{-\frac{(z-z_1^-)^2}{4D_e v_e(t-t')}\right\}\right] \mathrm{d}x'\mathrm{d}y'\mathrm{d}z'\mathrm{d}t' \tag{2.9}$$

where

$$z_0^+ = z_S \\ z_0^- = -z_S - 2z_E \\ z_1^+ = z' \\ z_1^- = -z' - 2z_E \tag{2.10}$$

In principle, equation (2.9) gives the Raman signal according to our model, nevertheless the integral has no analytical solution and would require a multiple numerical integration over four variables in order to be computed. Since this goes beyond our computational capabilities, we will introduce some approximations to obtain a simpler expression.
We will then consider $D_e = D$, $\mu_{abe} = \mu_{ab}$ and $v_e = v$. That means Raman photons, after

generation, will propagate seeing the same properties of the material as Rayleigh photons. This approximation is similar to the simplified heuristic model for Diffuse Raman but, since we followed a more rigorous calculation based on DE, we should obtain better results. With this approximation equation (2.9) becomes:

$$\begin{aligned}\Phi_e(\vec{r},t) = \int \frac{\mu_{sR}v^2}{(16\pi^2D^2v^2)^{3/2}} \frac{1}{(t'(t-t'))^{3/2}} \exp\left\{-(\mu_{ab}+\mu_{sR})vt + \mu_{sR}vt'\right\} \times \\ \times \exp\left\{-\frac{x'^2+y'^2}{4Dvt'} - \frac{(x-x')^2+(y-y')^2}{4Dv(t-t')}\right\} \times \\ \times \left[\exp\left\{-\frac{(z'-z_0^+)^2}{4Dvt'}\right\} - \exp\left\{-\frac{(z'-z_0^-)^2}{4Dvt'}\right\}\right] \times \\ \times \left[\exp\left\{-\frac{(z-z_1^+)^2}{4Dv(t-t')}\right\} - \exp\left\{-\frac{(z-z_1^-)^2}{4Dv(t-t')}\right\}\right] \mathrm{d}x'\mathrm{d}y'\mathrm{d}z'\mathrm{d}t'\end{aligned} \tag{2.11}$$

Thanks to the approximation it is now possible to integrate with respect to the variables x' and y'.
The corresponding integrals are of the type

$$\int_{-\infty}^{+\infty} \exp\{-aX^2 - b(c-X)^2\}\mathrm{d}X = \sqrt{\frac{\pi}{a+b}} \exp\left\{-\frac{abc^2}{a+b}\right\} \tag{2.12}$$

with

$$\begin{aligned} a &= 1/4DVt' \\ b &= 1/4Dv(t-t') \\ c &= x \end{aligned} \tag{2.13}$$

so we arrive at:

$$\begin{aligned}\Phi_e(\vec{r},t) = \frac{\mu_{sR}}{16\pi^2D^2t} \exp\left\{-\frac{x^2+y^2}{4Dvt} - \mu_a vt\right\} \int \frac{\exp\left\{\mu_{sR}vt'\right\}}{\sqrt{t'(t-t')}} \times \\ \times \left[\exp\left\{-\frac{(z'-z_0^+)^2}{4Dvt'}\right\} - \exp\left\{-\frac{(z'-z_0^-)^2}{4Dvt'}\right\}\right] \times \\ \times \left[\exp\left\{-\frac{(z-z_1^+)^2}{4Dv(t-t')}\right\} - \exp\left\{-\frac{(z-z_1^-)^2}{4Dv(t-t')}\right\}\right] \mathrm{d}z'\mathrm{d}t'\end{aligned} \tag{2.14}$$

The remaining integral in the variables z' and t' cannot be solved analytically but we can proceed with a numerical calculation. z' has to be integrated in the interval $(0, +\infty)$ while the interval for t' is $(0, t)$.
To further simplify the calculations, before the numerical integration, we switch to the reflectance, according to the following formula (from Partial Current Boundary Condi-

tions):

$$R(\rho,t)=\frac{1}{2A}\Phi(\rho,z=0,t) \tag{2.15}$$

This allows eliminating the dependence on z and highlighting the source-detector distance $\rho=\sqrt{x^2+y^2}$. The final result is:

$$\begin{aligned}R_e(\rho,t)=\frac{\mu_{sR}}{16\pi^2D^2t}\exp\left\{-\frac{\rho^2}{4Dvt}-\mu_a vt\right\}\int_0^{+\infty}\int_0^t\frac{\exp\{\mu_{sR}vt'\}}{\sqrt{t'(t-t')}}\times\\ \times\left[\exp\left\{-\frac{(z'-z_0^+)^2}{4Dvt'}\right\}-\exp\left\{-\frac{(z'-z_0^-)^2}{4Dvt'}\right\}\right]\times\\ \times\left[\exp\left\{-\frac{(-z')^2}{4Dv(t-t')}\right\}-\exp\left\{-\frac{(z'+2z_E)^2}{4Dv(t-t')}\right\}\right]\mathrm{d}z'\mathrm{d}t'\end{aligned} \tag{2.16}$$

This formula gives the power per unit surface of Raman signal emerging from a point placed at a distance ρ from the source after a time t.
The numerical results have been compared to that obtained from the simplified heuristic model of Diffuse Raman.

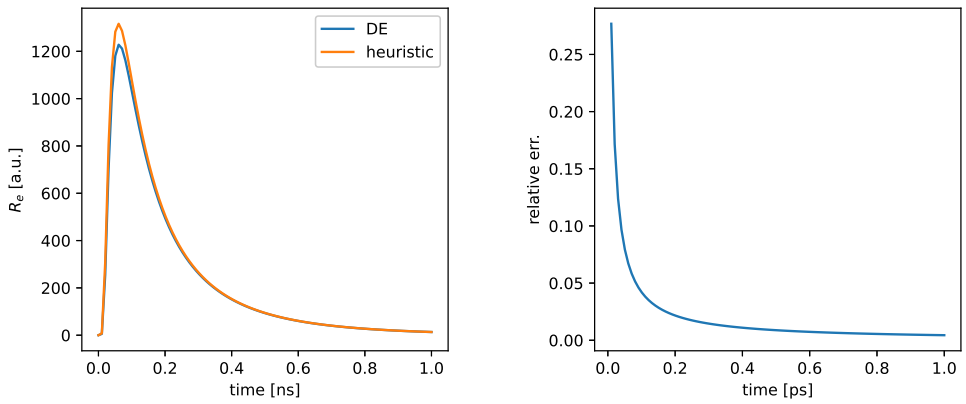

Figure 2.2: Numerical simulation of Raman reflectance with $\mu_a=0.1cm^{-1}$, $\mu_s'=10cm^{-1}$, $\rho=0.5cm$ (on the left) and relative error between the two models (on the right)

It is possible to see that, as expected, the two models give almost the same result. In particular, the simplified heuristic model slightly overestimates the signal with respect to the DE based model, especially at early times. This can be justified by the fact that, being a direct derivation from Rayleigh fluence, the heuristic model does not consider a further diffusion of Raman photons after their generation which delays and decreases the signal.

2.2. Calculation of generation depth of Raman photons

A very important information in Diffuse Raman measurements is the depth at which Raman photons are generated. In fact, as Raman photons bring the information about the chemical composition of the layer in which they are generated, a precise quantification of the depth with respect to other measurement parameters such as time or source-detector distance is essential to get a precise stratigraphy of the sample.
Since no references in literature were found about this topic, for the first time, using the model we have just described in section 2.1 and taking inspiration from reference [29], we developed an approach to determine the depth at which detected Raman photons were generated according to their time-of-flight and the source-detection distance used during measurements.
We will now present the calculations of this approach.
The arrival point of the following calculations will be the probability density function $f(z,t)$ of detected Raman photons with respect to their generation depth z and time-of-flight t. This function allows then to easily calculate the average generation depth of detected Raman photons z_{avg}.
Similarly to reference [29], the probability density function can be calculated as

$$\begin{aligned} f(z,t) &= \frac{1}{R_e(\rho,t)} \frac{R_e(\rho,t;z_{gen}=z+dz) - R_e(\rho,t;z_{gen}=z)}{dz} = \\ &= \frac{1}{R_e(\rho,t)} \frac{\mathrm{d}R_e(\rho,t;z_{gen}=z)}{\mathrm{d}z} \end{aligned} \tag{2.17}$$

The physical meaning of equation (2.17) is that we are calculating how much the reflectance $R_e(\rho,t)$ (equivalent to the detected signal) is influenced by the Raman generation at depth z. This value must then be normalized with respect to all the photons detected, namely the reflectance calculated in section 2.1.1, in order to obtain the desired probability density function.
Therefore, our approach consists in calculating the reflectance of Raman signal $\mathrm{d}R_e(\rho,t;z_{gen})$ when the Raman generation occurs only is an infinitesimal layer of thickness $\mathrm{d}z$ at depth $\bar{z}$ in a semi-infinite medium, as shown in figure 2.3.
To implement this approach we use the same diffusion equations of the model described in section 2.1 but, in order to limit the Raman generation to a single depth z we multiply by a delta function $\delta(z-\bar{z})$ the source term of the second equation.
As excitation source we will consider for simplicity a point-like instantaneous illumination.

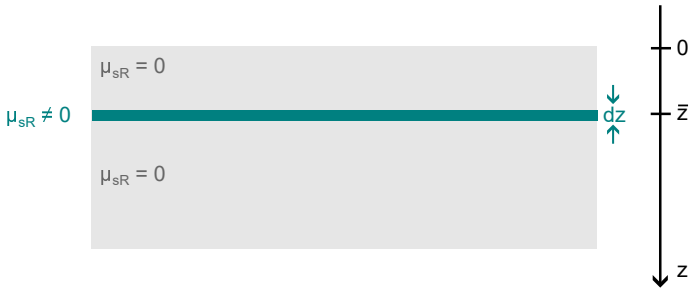

Figure 2.3: Schematic representation of the approach used in our calculation about the generation depth of detected Raman photons

These assumptions give the following two diffusion equations:

$$\begin{cases} \left(\frac{1}{v}\frac{\partial}{\partial t} - D\nabla^2 + \mu_a\right)\Phi(\vec{r},t) = \delta(\vec{r})\delta(t) & \text{(2.18a)} \\ \left(\frac{1}{v_e}\frac{\partial}{\partial t} - D_e\nabla^2 + \mu_{ae}\right)\Phi_e(\vec{r},t) = \mu_{sR}\Phi(\vec{r},t)\delta(z-\bar{z}) & \text{(2.18b)} \end{cases}$$

The solution for Raman signal can be calculated with the same passages of section 2.1.1, however there is a little difference in equation (2.6). In fact, the presence of $\delta(z'-\bar{z})$ makes the integral with respect to z' collapse to the function evaluated in $\bar{z}$ and let us to directly obtain $\mathrm{d}\Phi_e(x,y,\bar{z},t)$, namely the contribution to $\Phi_e(x,y,z,t)$ from the Raman photons generated at the depth $\bar{z}$.

$$\begin{aligned} \mathrm{d}\Phi_e(x,y,\bar{z},t) &= \mu_{sR}\int G_e(\vec{r},\vec{r'},t,t')G(\vec{r'},t')\delta(z'-\bar{z})\mathrm{d}x'\mathrm{d}y'\mathrm{d}z'\mathrm{d}t' = \\ &= \mu_{sR}\int G_e(x,x',y,y',z,\bar{z},t,t')G(x',y',\bar{z},t')\mathrm{d}x'\mathrm{d}y'\mathrm{d}t' \end{aligned} \tag{2.19}$$

The functions for G and G_e are (see equation (2.7)):

$$\begin{aligned} G(x',y',\bar{z},t') = \frac{v}{(4\pi Dvt')^{3/2}}\exp\left\{-\frac{x'^2+y'^2}{4Dvt'} - \mu_a v t'\right\}\times \\ \times\left[\exp\left\{-\frac{(\bar{z}-z_0^+)^2}{4Dvt'}\right\} - \exp\left\{-\frac{(\bar{z}-z_0^-)^2}{4Dvt'}\right\}\right] \end{aligned} \tag{2.20}$$

$$\begin{aligned} G_e(x,x',y,y',z,\bar{z},t,t') = \frac{v_e}{(4\pi D_e v_e(t-t'))^{3/2}}\exp\left\{-\frac{(x-x')^2+(y-y')^2}{4D_e v_e(t-t')}\right\}\times \\ \exp\left\{-\mu_{abe}v_e(t-t')\right\}\left[\exp\left\{-\frac{(z-\bar{z})^2}{4D_e v_e(t-t')}\right\} - \exp\left\{-\frac{(z+\bar{z}+2z_E)^2}{4D_e v_e(t-t')}\right\}\right] \end{aligned} \tag{2.21}$$

Substituting (2.20) and (2.21) in (2.19), using the approximation $D_e = D$, $\mu_{abe} = \mu_{ab}$ and $v_e = v$ and integrating with respect to x' and y', one obtains:

$$\begin{aligned} \mathrm{d}\Phi_e(x,y,\bar{z},t) = \frac{\mu_{sR}}{16\pi^2 D^2 t}\exp\left\{-\frac{x^2+y^2}{4Dvt} - \mu_a v t\right\}\int \frac{\exp\left\{\mu_{sR} v t'\right\}}{\sqrt{t'(t-t')}}\times \\ \times\left[\exp\left\{-\frac{(\bar{z}-z_0^+)^2}{4Dvt'}\right\} - \exp\left\{-\frac{(\bar{z}-z_0^-)^2}{4Dvt'}\right\}\right]\times \\ \times\left[\exp\left\{-\frac{(z-\bar{z})^2}{4Dv(t-t')}\right\} - \exp\left\{-\frac{(z+\bar{z}+2z_E)^2}{4Dv(t-t')}\right\}\right]\mathrm{d}t' \end{aligned} \tag{2.22}$$

The integral with respect to t' has no analytical solution so it has to be computed numerically. Before doing that we finish our calculation switching to the reflectance thanks to equation (2.15).

$$\begin{aligned} \mathrm{d}R_e(\rho,t) = \frac{\mu_{sR}}{16\pi^2 D^2 t}\exp\left\{-\frac{\rho^2}{4Dvt} - \mu_a v t\right\}\int_0^t \frac{\exp\left\{\mu_{sR} v t'\right\}}{\sqrt{t'(t-t')}}\times \\ \times\left[\exp\left\{-\frac{(\bar{z}-z_0^+)^2}{4Dvt'}\right\} - \exp\left\{-\frac{(\bar{z}-z_0^-)^2}{4Dvt'}\right\}\right]\times \\ \times\left[\exp\left\{-\frac{(-\bar{z})^2}{4Dv(t-t')}\right\} - \exp\left\{-\frac{(-\bar{z}-2z_E)^2}{4Dv(t-t')}\right\}\right]\mathrm{d}t' \end{aligned} \tag{2.23}$$

Dividing this last expression by the total reflectance $R_e(\rho,t)$ we calculated in section 2.1.1, we have finally the probability density function $f(z,t)$.

$$\begin{aligned} f(z,t) = \frac{\int_0^t \frac{\exp\left\{\mu_{sR} v t'\right\}}{\sqrt{t'(t-t')}}\left[\exp\left\{-\frac{(z-z_S)^2}{4Dvt'}\right\} - \exp\left\{-\frac{(z+z_S+2z_E)^2}{4Dvt'}\right\}\right]\times}{\int_0^{+\infty}\int_0^t \frac{\exp\left\{\mu_{sR} v t'\right\}}{\sqrt{t'(t-t')}}\left[\exp\left\{-\frac{(z'-z_S)^2}{4Dvt'}\right\} - \exp\left\{-\frac{(z'+z_S+2z_E)^2}{4Dvt'}\right\}\right]\times} \\ \times\left[\exp\left\{-\frac{(-z)^2}{4Dv(t-t')}\right\} - \exp\left\{-\frac{(z+2z_E)^2}{4Dv(t-t')}\right\}\right]\mathrm{d}t' \\ \times\left[\exp\left\{-\frac{(-z')^2}{4Dv(t-t')}\right\} - \exp\left\{-\frac{(z'+2z_E)^2}{4Dv(t-t')}\right\}\right]\mathrm{d}z'\mathrm{d}t' \end{aligned} \tag{2.24}$$

The function $f(z,t)$ has been evaluated for different values of depth z and time t. The result obtained is shown in figure 2.4 .

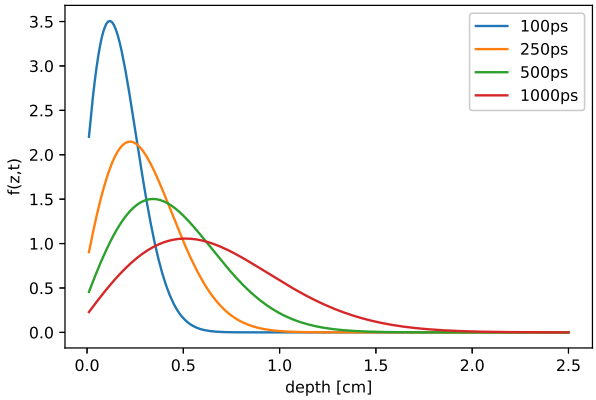

Figure 2.4: Probability density function for generation depth of Raman photons with $\mu_a = 0.1cm^{-1}$ and $\mu_s' = 10cm^{-1}$, calculated for different times t

The average depth of generation of Raman photons can now be calculated as the average value of z weighed by the probability function $f(z,t)$.

$$z_{avg}(t) = \langle z \rangle(t) = \int z f(z,t) \mathrm{d}z \tag{2.25}$$

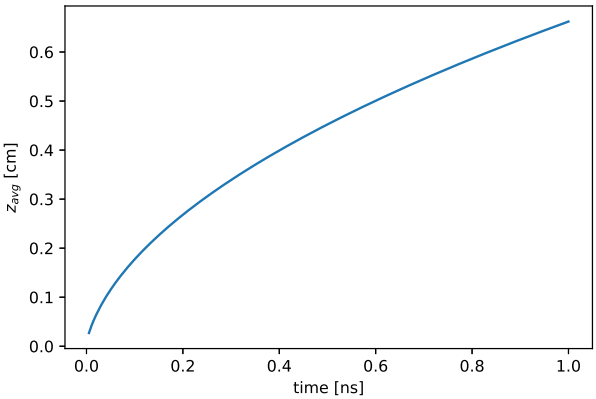

Figure 2.5: Average generation depth of Raman photons with respect to detection time in a medium with $\mu_a = 0.1cm^{-1}$ and $\mu_s' = 10cm^{-1}$

It is possible to note that, as expected, a higher time-of-flight of the photons yields a higher generation depth. This justifies the fact that by time gating a TD Diffuse Raman measurement it is possible to select the signal coming from deep layers and obtain the Raman spectrum of different layers in our sample. Moreover, thanks to these calculations, we have now the possibility to quantify the depth of each layer according to the selected time gate.

2.2.1. Simulations of Raman signal of a bilayer

With the calculations done in section 2.2, we simulated the Raman signal of a Diffuse Raman measurement on a bilayer. For simplicity we considered the same optical properties for each layer, but we supposed that the Raman spectrum of depths $z > d$ is different than that of depths $z < d$.

Figure 2.6: Bilayer medium considered for the simulation

Given these hypothesis, the Raman signal coming from the top layer and the Raman signal coming from the bottom layer can be respectively calculated as:

$$R_e^{TOP}(\rho,t) = R_e(\rho,t)\int_0^d f(z,t)\mathrm{d}z \tag{2.26a}$$

$$R_e^{BOTTOM}(\rho,t) = R_e(\rho,t)\int_d^{+\infty} f(z,t)\mathrm{d}z \tag{2.26b}$$

The results obtained are shown in figure 2.7.

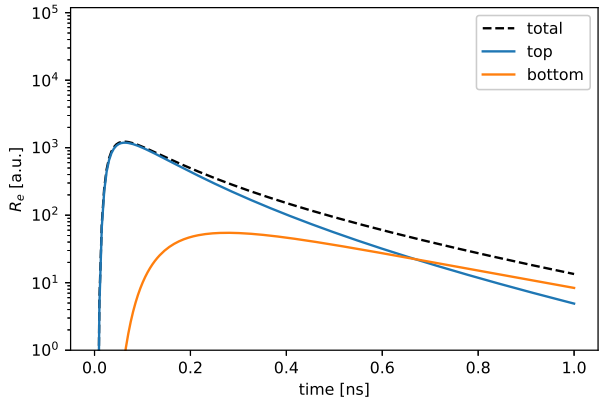

Figure 2.7: Simulation of Diffuse Raman signal from top and bottom layers in a bilayer medium $\mu_a = 0.1cm^{-1}$, $\mu_s' = 10cm^{-1}$, $\rho = 0.5cm$, $d = 0.5cm$

It is possible to see that the signal of the bottom layer is delayed with respect to that of

the top layer because of the longer diffusion of photons in the medium. Moreover, note that after 0.6 ns the signal of the bottom layer starts to prevail with respect to that of the top one. This is in agreement with our previous calculations on the average generation depth with respect to time: in fact, looking at figure 2.5, it can be noted that at a time of 0.6 ns the expected average generation depth reaches 0.5 cm thus after this time the detected signal will come mainly from the bottom layer rather than from the top layer. Further insight about this theoretical model will be given in chapter 4 when these numerical simulations will be used to interpret experimental data.

3 | TD-DIRS System

In this chapter we present the instrumentation for Time Domain Diffuse Raman Spectroscopy (TD-DIRS) that has been improved and used during this thesis work.
At a very high level it is possible to identify four main parts in our system:

- a laser source which provides the light to excite the sample;
- illumination optics to deliver light to the surface of the sample;
- collection optics to collect light from the sample and select only Raman scattered photons;
- a spectrometer which allows the measurement of the Raman spectrum.

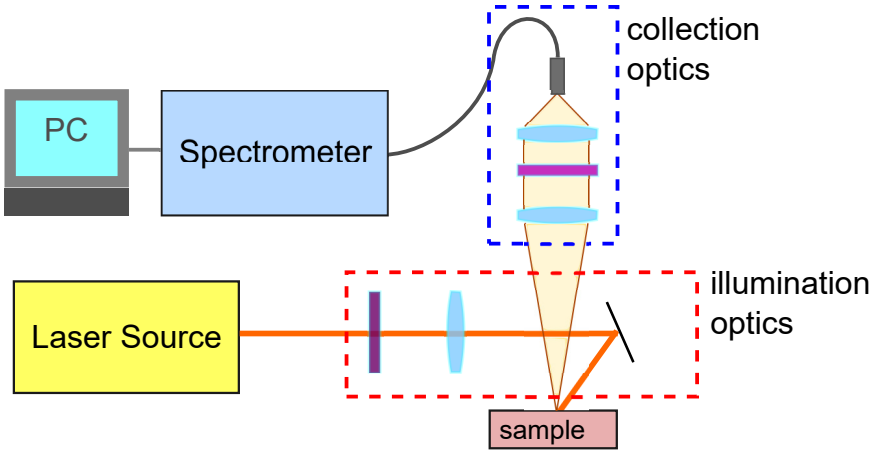

Figure 3.1: Schematic drawing of the instrumentation

In the following sections each part will be described in detail and, at the end, an explanation of the procedures required to take a measurement will be reported.

3.1. Laser source

The light source of our instrumentation is a custom made Ti:Sapphire (Ti:Al_2O_3) laser which can work both in CW and in active mode-locking (ML) regime with a tunable

wavelength.
The scheme of the laser is represented in figure 3.2.

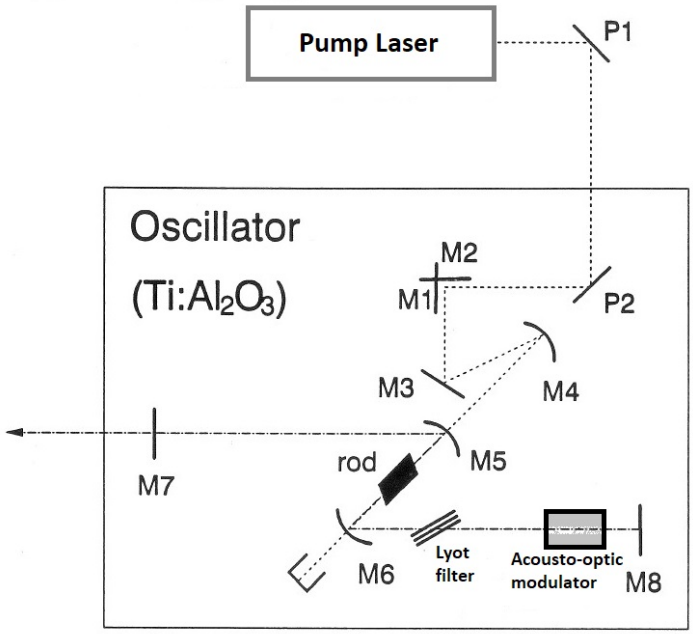

Figure 3.2: Scheme of the Ti:Sapphire laser

The Ti:Al_2O_3 crystal is pumped by a semiconductor laser (Verdi G-10 by Coherent) that provides a CW light beam at a wavelength of 532 nm with an adjustable power between 0.01 W and 10 W.
The optical cavity is a modification of the Model 3900S laser by Spectra Physics. In fact, the original cavity, initially designed to operate only in CW, has been lengthened and an acousto-optic modulator has been inserted to make possible the mode-locking regime [30]. The acousto-optic modulator (ML-50Q by IntraAction) is built with a quartz crystal in which a compression wave is produced by piezoelectric elements working with a signal from a radiofrequency generator. The modulation frequency from the radiofrequency generator is set to 50MHz in order to obtain a train of pulses with a repetition rate of 100MHz. That is because the standing wave pattern generated in the crystal, which modulates the cavity losses for the mode-locking regime, has a doubled frequency with respect to the external modulation frequency.
A cooled water refrigeration system keeps the Ti:Al_2O_3 crystal and the quartz crystal of the acousto-optic modulator at a stable temperature of about 16°C to ensure heat dissipation and a constant behavior of the laser.
The wavelength tunability is possible thanks to a Lyot filter made of three birefringent foils of quartz. This filter has a bandwidth of 40 GHz and allows selecting a precise

oscillation mode and wavelength of the Ti:Sapphire laser. Thanks to this feature we have the possibility to select a desired excitation wavelength for Raman scattering and we can easily align the spectrometer without other instruments.
A characterization of the Ti:Sapphire laser has been done at the beginning of the thesis work in order to be sure of its performances, before its use for Diffuse Raman Spectroscopy measurements. As we will see from the characterization measurements reported in the next subsections, this light source is ideal for Diffuse Raman Spectroscopy because it has:

- high power which is helpful in dealing with the low efficiency of Raman scattering;
- narrow spectral bandwidth which limits the spreading of Raman spectral features due to the excitation source;
- short pulses which allow a high temporal resolution in Time Domain measurements.

3.1.1. Slope efficiency

As a first step for the characterization of the Ti:Sapphire laser we evaluated the slope efficiency. At first the laser was carefully aligned and cleaned. Then, the laser wavelength was fixed at 800 nm and the output power of the laser was measured with a thermopile connected to a powermeter for different powers of the pump beam. The data has been plotted (figure 3.3) and the slope efficiency, defined as the angular coefficient of the straight line of the laser output power with respect to the power of the pump, has been calculated (table 3.1). The same procedure allowed also obtaining an estimation of the threshold power,

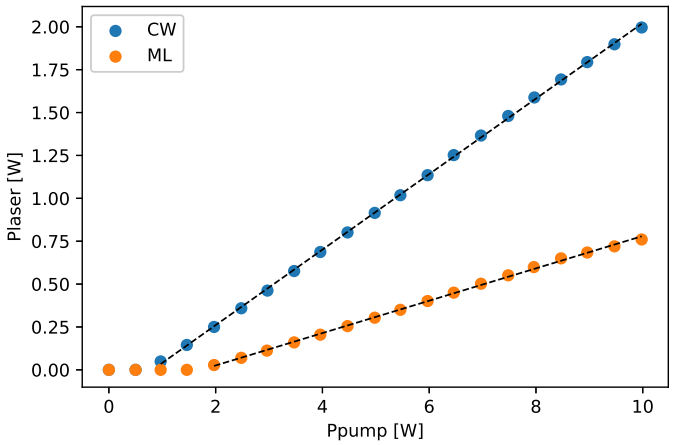

Figure 3.3: Slope efficiency plot of the Ti:Sapphire laser

namely the minimum pump power needed to start the laser action. The measurement was taken with the laser both in CW and in mode-locking regime (considering that in

mode-locking regime we measure the average power because the thermopile is not sensible to fast variations of laser pulses).

	CW	ML
Slope Efficiency [-]	0.22	0.09
Threshold Power [W]	0.8	1.7

Table 3.1: Slope efficiency and threshold power for the Ti:Sapphire laser

From these measurements it is possible to note that our Ti:Sapphire laser shows a good linearity until the maximum power of the pump laser meaning that no saturation phenomena in the crystal occur. We reached a maximum power of almost 2 W in CW and 0.76 W in ML, however as default operation mode we decided to keep lower pump powers for safety reasons.
The values obtained in these measurements are very important because, since the slope efficiency depends on the alignment and the cleaning of the laser, they can be used as a reference to check the status of the laser every time it is turned on.

3.1.2. Tunability curve

Since our Ti:Sapphire laser is tunable, meaning that its emission wavelength can be controlled precisely, we verified its tunability range and the output power stability with the wavelength. The output power was measured with a thermopile connected to a powermeter while the wavelength was monitored with a spectrometer (USB2000 by Ocean Optics). The data obtained for both CW and ML regimes have been plotted in a power versus wavelength curve, also called tunability curve.

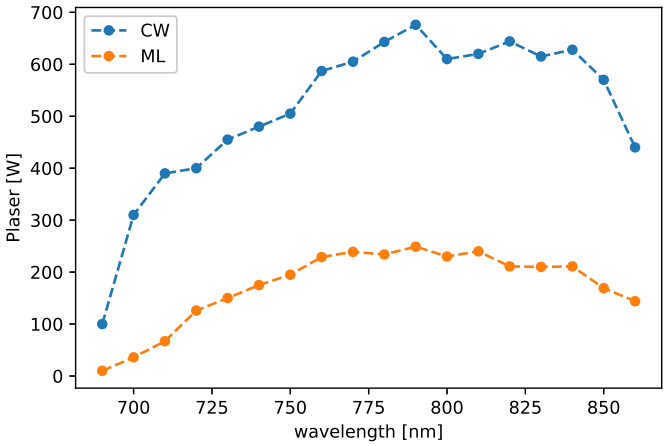

Figure 3.4: Tunability curve of the Ti:Sapphire laser

The tunability range is 700 – 860 nm. However, the most efficient working region of the laser is between 760 nm and 840 nm since the output power decreases near to the limits of the tunability range. This decrease is due to the reduction of reflectivity of the mirrors in laser cavity which increases the cavity losses thus reducing the slope efficiency and increasing the threshold power. At a certain point the reflectivity is so low that the laser action cannot occur.
Since the emission spectrum of Ti:Al_2O_3 crystal extends from 600 nm to 1100 nm, it is possible to obtain a laser action even outside the tunability range we verified. In fact, there are other two sets of mirrors, which can be mounted in the cavity, allowing the laser to work in the ranges 650 – 800 nm and 850 – 1000 nm.
However the performances of these two other sets of mirrors were not tested by us because the ideal spectral range for Diffuse Raman Spectroscopy is 740 – 840 nm. Indeed, at lower wavelengths there would be a greater contribution of fluorescence which contaminates Raman signal, while at higher wavelengths there would be an increased absorption by human tissue which hampers the application of our instrument to in vivo medical measurements.

3.1.3. Spectral bandwidth

To calculate the spectral bandwidth of the Ti:Sapphire laser, we measured the spectrum of the laser beam with a spectrometer (USB2000 by Ocean Optics). The result is reported in figure 3.5.

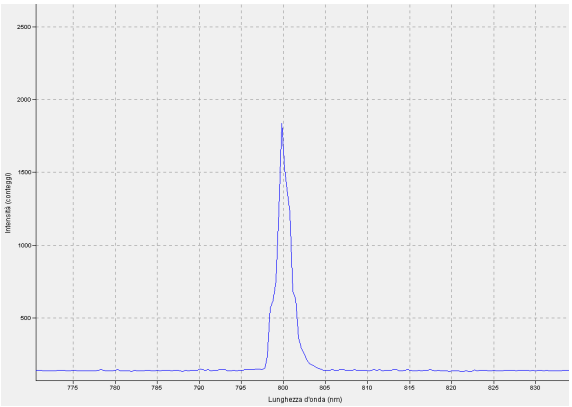

Figure 3.5: Spectrum of Ti:Sapphire laser measured with USB2000 spectrometer

However, the real spectral bandwidth is much narrower than the observed one which is limited by the spectrometer resolution. In fact, considering that our laser should give nearly Fourier limited Gaussian pulses, the spectral bandwidth can be estimated to be about 0.01 nm.

$$\begin{aligned} &\Delta\tau_p\Delta\nu = 0.441 \\ &\Delta\tau_{p(measured)} = 80\text{ps} \\ &\Delta\nu_{(estimated)} = 5.5\text{GHz} \rightarrow \Delta\lambda = \frac{\lambda^2}{c}\Delta\nu = 0.01\text{nm} \end{aligned} \tag{3.1}$$

This assumption finds a further confirmation from the measurements of the laser spectra with our spectrometer we will describe later. In fact, the bandwidth is lower than that observed with the USB2000 spectrometer and still limited by the spectral resolution of our spectrometer. Thus we can affirm that the laser bandwidth is certainly lower than 0.1 nm.

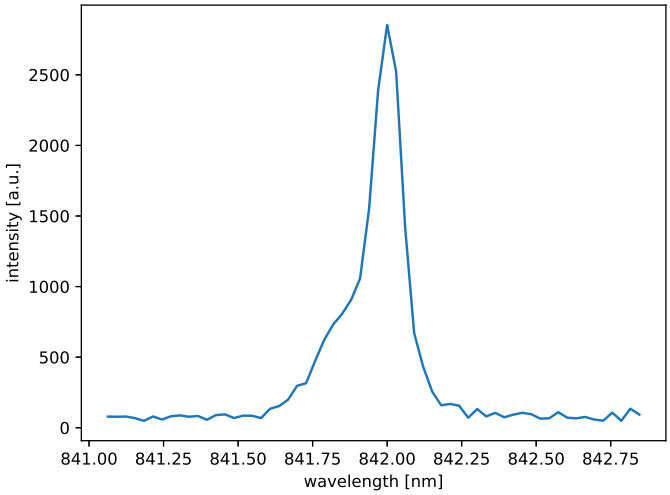

Figure 3.6: Spectrum of Ti:Sapphire laser measured with the spectrometer presented in chapter 3

A so narrow bandwidth is ideal for Raman spectroscopy because it does not contribute to broadening of Raman peaks.

3.1.4. Characterization of the pulse

With the Ti:Sapphire laser in mode-locking regime, we did a rough characterization of the pulses. In particular we measured the pulse duration (calculated as full width at half maximum - FWHM) and the average power for different intensities of the radiofrequency wave (carrier) in the acousto-optic modulator. The pulse shape and the FWHM were retrieved with a time correlated single photon counting detection scheme that we will describe in a following section, while the average power was measured with a thermopile

connected to a powermeter.

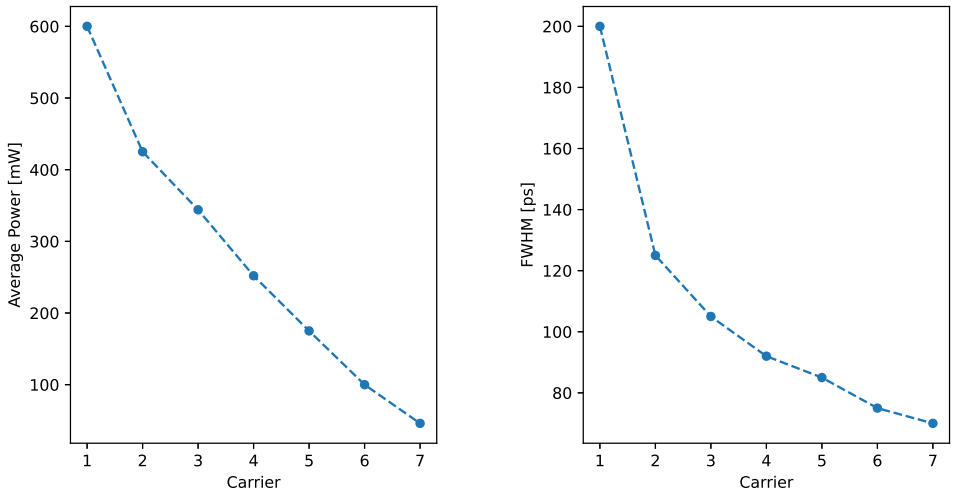

Figure 3.7: Average output power and pulse duration of the Ti:Sapphire laser with respect to the variation of mode-locking intensity (carrier)

It is possible to note that both the average power and the pulse duration decrease by increasing the modulation intensity. In fact, as the acousto-optic modulator modulates the cavity losses to make the laser working in mode-locking regime, if its modulation intensity is increased, the average losses will be greater but the ML will be more effective and the pulse duration and quality will be better. We measured a minimum pulse duration of 70 ps at level 7 of modulation intensity. Increasing further the carrier intensity the losses are too high and the laser action is stopped.
However, to have a best trade off between pulse duration and power, we chose to keep as default the carrier intensity at level 4 thus obtaining a pulse of 90 ps with an average power of 0.2 W. This pulse duration is sufficient to have a good temporal resolution and comparable to typical values in the field of Diffuse Optics.

3.1.5. Stability

As last measure for the characterization of our Ti:Sapphire laser we verified its stability in mode-locking regime. Pulse shapes were recorded every 1 s for one hour with a time correlated single photon counting detection scheme and then for each pulse we calculated three figures of merit: the number of photons counts at the peak, the barycenter position in time (barycenter is defined as $b = \int tI(t)\mathrm{d}t / \int I(t)\mathrm{d}t$) and the full width at half maximum (FWHM). These quantities are relevant because they give an indication of the stability respectively of peak power, repetition rate and pulse duration of our mode-locked laser.

The data were put together with those coming from a thermocouple which measured the temperature of the water in the cooling system during the whole measurement period.
This procedure has been repeated two times: the first one (STABILITY1) when the laser was just turned on and the second one (STABILITY2) when the laser has been working for more than one hour.
It is possible to see that during the STABILITY1 measurement the laser has not yet reached its equilibrium since the temperature of the coolant is still decreasing and the figures of merit are rather unstable showing a variation over one hour of about 30% for the peak power, 1% for the pulse position and 7% for the pulse duration.
Instead, during the STABILITY2 measurement we can affirm that the laser reached its equilibrium as the temperature of the coolant is constant and also the figures of merit show a good stability with variations over one hour of 10% for peak power, less than 1% for pulse position and 5% for pulse duration.

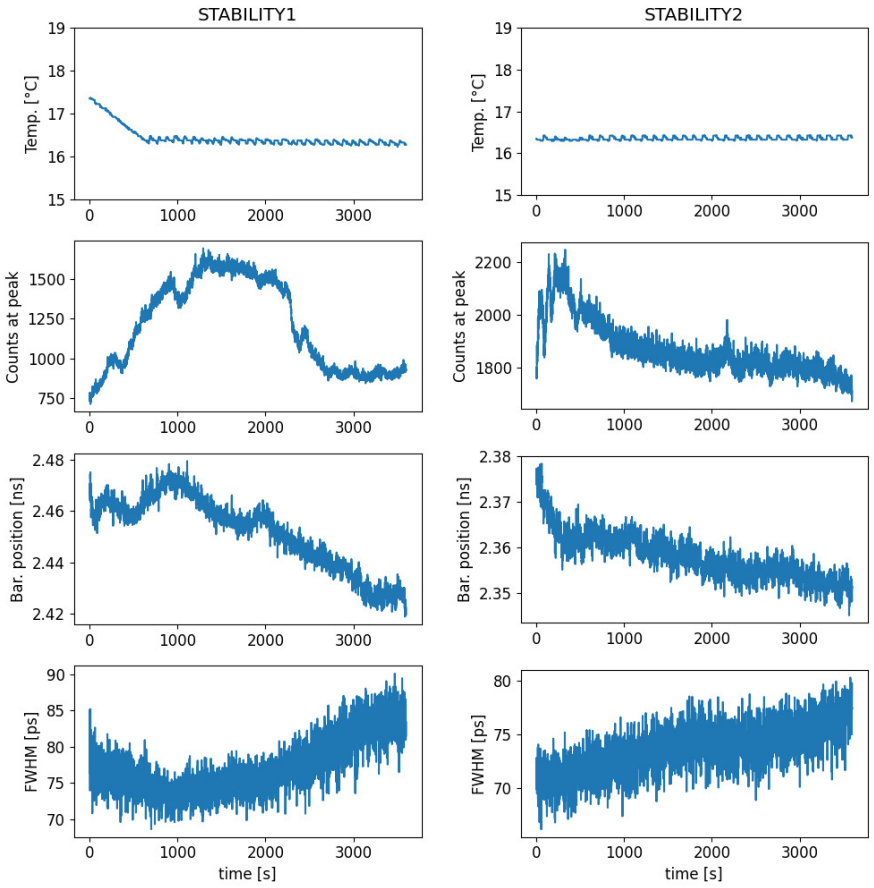

Figure 3.8: Stability measurements of Ti:Sapphire laser

Then, we can conclude that in order to obtain a stable behavior of the laser we need to turn it on at least 30 minutes before the measurements.

3.2. Illumination optics

After the output coupler of the Ti:Sapphire laser, the light beam pass through some optical elements before being delivered to the surface of the sample.
As first element we have an adjustable attenuator which allows regulating the power effectively shone on the sample in order to avoid the saturation of the detector.
Then, the laser beam is coupled to an optical fiber which guides it towards the sample. At the output of the fiber the beam is collimated, thanks to a fiber coupler, and passes through a bandpass filter (BP780-10 by Thorlabs) which removes any unwanted wavelength different than the one selected for excitation (780 nm) from the spectrum of impinging light.
At this point, we can use two different illumination schemes:

- a **point illumination scheme** in which the collimated beam is focused by a lens and reflected towards the sample surface by a mirror. The spot obtained has a radius of less than 1 mm;
- a **ring illumination scheme**, like that of inverse-SORS, in which the beam passes through an axicon (AX255 by Thorlabs) that makes it ring-shaped and then a mirror reflects the ring towards the sample surface. Changing the position of the axicon with respect to the image plane it is possible to vary the radius of the ring from 10 mm to 5 mm (these limits come from the mechanical setup of the instrumentation).

(a) point illumination (b) ring illumination

Figure 3.9: (a) point illumination scheme, (b) ring illumination scheme. In orange we have the illumination region while in blue the collection region

3.3. Collection optics

To collect light from the sample we use a non-contact approach with a custom-made probe. The optical scheme of the probe is represented in figure 3.10 (note that in reality the orientation is vertical).

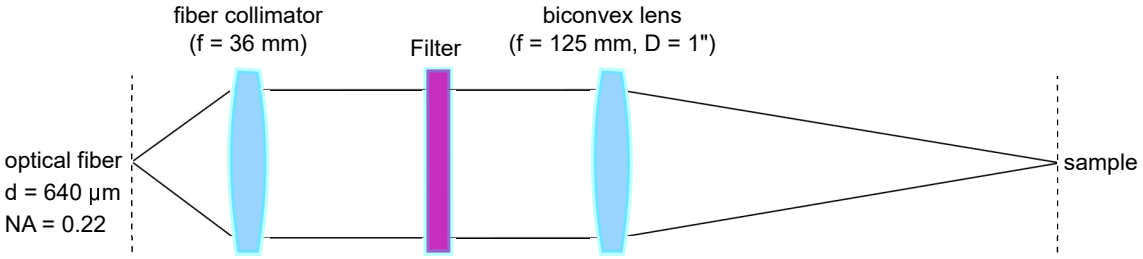

Figure 3.10: Optical scheme of the probe

The choice of this configuration is due mainly to three scopes.
Firstly, the non-contact approach enables an easy access to the sample guaranteeing its modification such as the addition or removal of layers of other materials during the testing of the instrumentation. For this reason, in the optical design we ensured that the distance between the first lens and the image plane was at least 10 cm.
Secondly, the optical system of the probe allows an easy insertion and removal of a long pass filter (FELH800 by Thorlabs) to suppress the Rayleigh scattered light from the collected light and keep only the Raman-Stokes photons.
And, at last, the probe, according to the lenses mounted, allows freely selecting the diameter of the collection spot on the sample. In our design we wanted a collection spot larger than the fiber core without reducing too much the numerical aperture. For this reason we have chosen a lens with a focal length f = 125 mm thus we obtain a magnification factor of 3.4, meaning that the collection spot has a diameter of 2.2 mm (since the optical fiber core has a diameter of 640 µm) and a collection numerical aperture of 0.06.
A commercial fiber collimator (F810SMA-780 by Thorlabs) couples the collected light to a round-to-linear seven fiber bundle (BFL200LS02 by Thorlabs) which guides light from the probe to the spectrometer.

3.4. Spectrometer

The spectrometer of our instrumentation, designed on the model of that described by Berto et al. in the reference [31], is based on a reflective dispersion grating, a single pixel camera and a time correlated single photon counting (TCSPC) detection method. This scheme gives us the big advantage of collecting both the spectrum and the temporal behavior of the signal. In fact, for Time Domain Diffuse Raman Spectroscopy we need to measure the spectrum of the signal as well as its temporal behavior that, by means of time gating, makes possible the selection of Raman signal coming from different depths of the sample.

The scheme of the spectrometer is reported in figure 3.11.

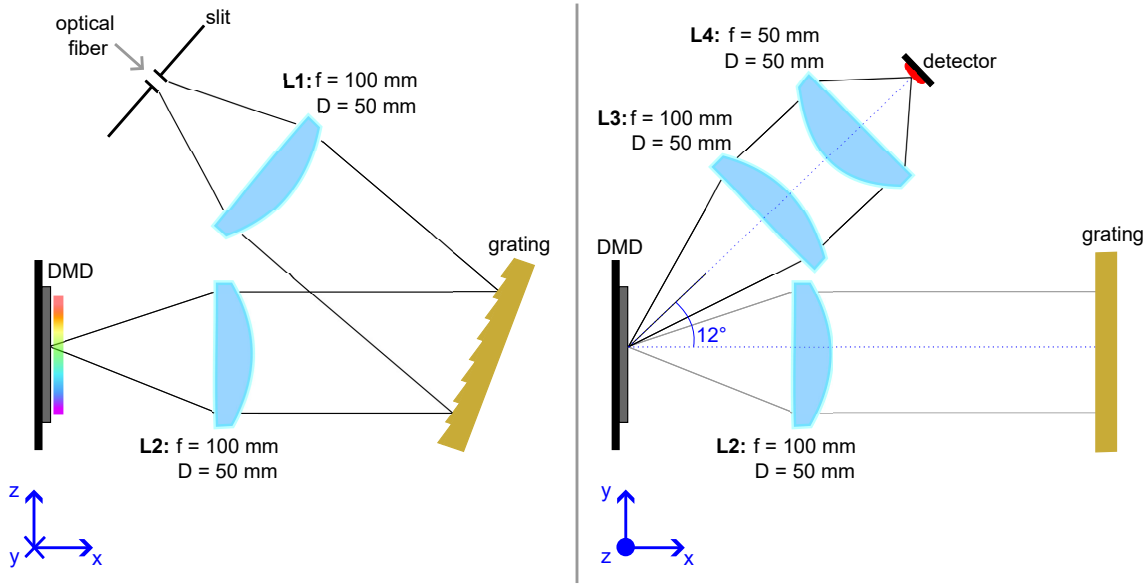

Figure 3.11: Scheme of the spectrometer

The light exiting the optical fiber coming from the probe passes through a slit and enters the spectrometer. A first optical system, composed of two lenses and a reflective dispersion grating (GR50-1208 by Thorlabs), is used to collimate the light exiting the slit, spatially separate the different wavelengths of the collected light and create an image in which different wavelengths are focused at different heights on the image plane. The magnification of this optical system is 1 so on the image plane we get a 1:1 copy of the entrance slit of the spectrometer. The design of this system requires to minimize all aberrations (spherical, astigmatism, chromatic) and also field curvature since all the wavelengths should be focused with the minimum spot possible independently of the height on the image plane. A 0.65-inch (14.5 mm x 8 mm) digital micromirror device (DMD – DLP6500 by Texas Instruments) is positioned on the image plane, after the second lens. The DMD has an array of 1920 x 1080 micromirrors, each one with a size of 7.5 µm x 7.5 µm, that can be singularly tilted with an angle of either +12° or -12° with respect to the normal to the surface of the device. This device is positioned so that the light coming from the lens impinges perpendicularly to its surface and one direction of reflection points towards the detector while the other one directs light away from the instrumentation. Since the rotation axis of each micromirror is parallel to the diagonal of the entire surface, The DMD is mounted with an orientation of 45° as in figure 3.12.
A second optical system, composed of two lenses, is interposed between the DMD and the detector. In fact, since the reflected light from the DMD is diverging, we need to make it converging in order to focus it on the detector. Moreover, we need a magnification factor

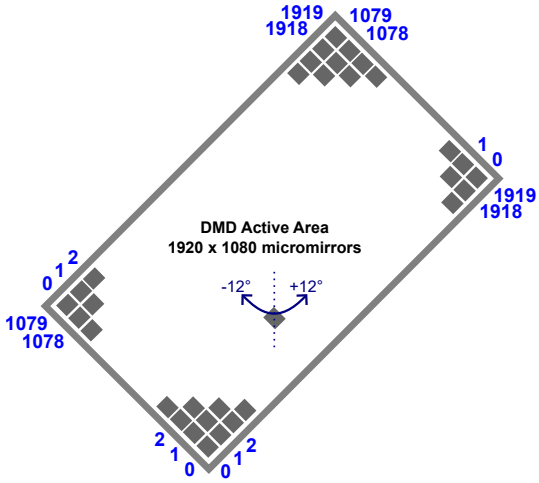

Figure 3.12: Scheme of the DMD with pixel indexing

less than 0.367 to be able to make the whole image of the DMD fit on the smaller active area (3 mm x 3 mm) of the detector.
The detector is a hybrid detector (HPM100-50 by Beker & Hickl) with a GaAs photocathode connected to a time correlated single photon counting board (SPC-130 by Beker & Hickl). This type of detector integrates the technology of both a photomultiplier tube and an avalanche diode enabling the detection of very low signals thanks to a quantum efficiency of 10%, a reduced noise (dark count rate = 500 counts/s) and high temporal resolution (130 ps).
This second part of the spectrometer (DMD + detector) is as a TCSPC single pixel camera to collect the image of the spectrum dispersed on the DMD by the dispersion grating and its temporal evolution.
Further details about the spectrometer will be presented in next sections.

3.4.1. Working principles

Before describing the operation modes of our spectrometer, we recall in this section some theoretical concepts about the techniques of single pixel imaging and time correlated single photon counting on which the spectrometer is based.

Single pixel imaging

Single pixel imaging is a technique, directly derived from the theories of signal compression, which had its first implementation in 2008 in a single pixel camera by Duarte et al. [32]. This technique consists in capturing the image of an object by decomposing it in many different patterns with different weights. With a reconstruction process in which

each pattern is multiplied by its weight and combined to the other ones, it is possible to reconstruct the image of the object.

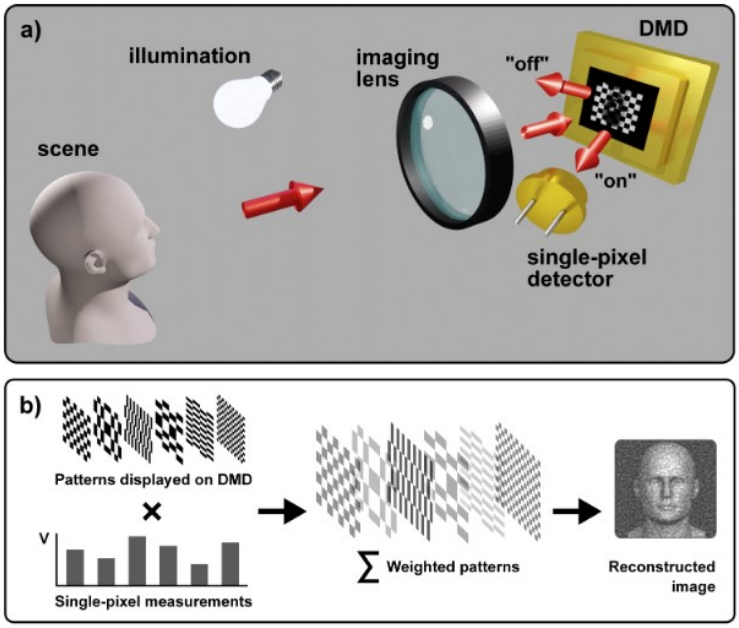

Figure 3.13: Single pixel imaging (structured detection) setup (a) and image reconstruction workflow (b) [33]

Mathematically, each weight $y[m]$ associated with a pattern $P[m]$ is equivalent to the inner product between the image x and the pattern.

$$y[m] = \langle P[m], x \rangle \tag{3.2}$$

This operation is repeated for each of the M selected patterns from the set of patterns $\{P[m]\}$, thus leading to the M components vector y, which is what we measure. Note that this process is equal to a matrix multiplication so the image can be reconstructed by matrix inversion.

$$y = Mx \rightarrow x = M^{-1}y \tag{3.3}$$

Since a N x N pixel image is compressed into M patterns, so being captured with less sampling M $<$ N and data, this technique is also called compressive sensing or sub-Nyquist acquisition.
A further improvement, called super sub-Nyquist acquisition, instead, exploits only a subset of Q $<$ M patterns from the set $\{P[m]\}$ for capturing the image. Also in this case, provided that the image is sparse, it is possible to reconstruct the image exploiting some minimization algorithms during reconstruction.

In our spectrometer, the DMD acts as a spatial light modulator to generate the patterns needed for collecting the image of the spectrum created on its surface by the dispersion grating. In the next section we will describe the patterns we use as well as the reconstruction approaches we adopted.

TCSPC

Time correlated single photon counting (TCSPC) is a technique which allows to measure the shape of a light pulse. The instrumentation for TCSPC (all contained in the Becker & Hickl SPC-130 board with exception of the detectors) consists of two single photon counting (SPC) lines connected to a time to amplitude converter (TAC).

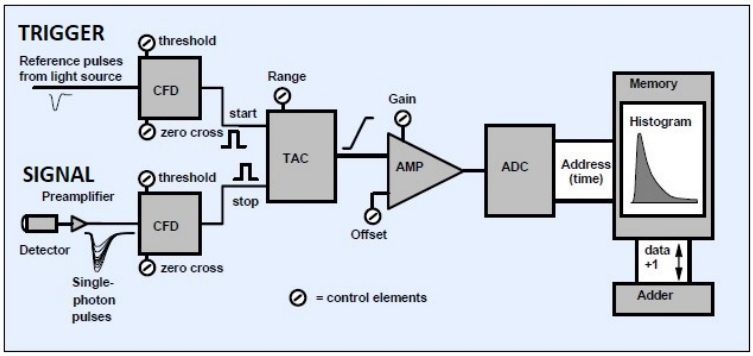

Figure 3.14: Components of a TCSPC line (from [34])

Each SPC line is able to detect when a single photon hits the detector: in fact, the detector generates a pulse every time a photon impinges on its active area, then this pulse is amplified (if needed) and finally detected by a constant fraction discriminator. The two SPC lines, denominated trigger and signal, respectively give a start and stop signal to the TAC. The TAC is basically a capacitor that, being charged, allows to measure the time between the two events and make it readable by electronics by converting it to a voltage. Correspondingly to the amount of time measured, a memory location is incremented and, after collecting a lot of photons, at the end of the acquisition it is possible to reconstruct a histogram of the number of photon counts vs their arrival time.
Provided that the light intensity is sufficiently low, so that it is unlikely for the detector to detect more than one photon per excitation pulse, the histogram is equal to the pulse shape.
In our instrumentation the signal line is that coming from the HPM100-50 detector of the spectrometer while the trigger comes from a SiPM detector which detects the pulse right after the output coupler of the laser where a beam splitter separates 5% of the laser beam towards this detector.

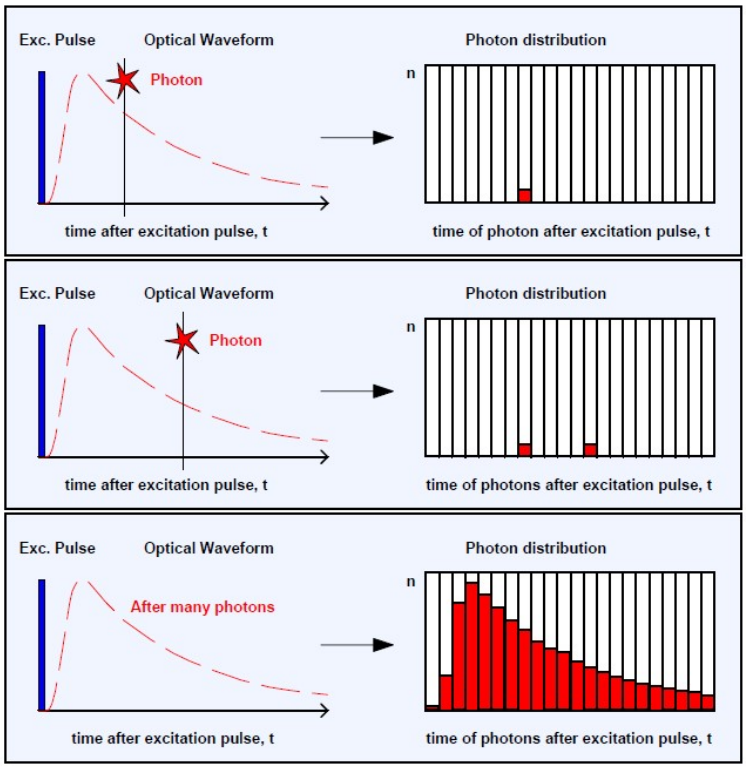

Figure 3.15: Working principle of TCSPC (from [34])

3.4.2. Operation modes

Our spectrometer can work in many modalities according to the pattern created on the DMD:

Monochromator mode / Raster Scan: in this mode a single line of the DMD is activated (mirrors oriented towards the detector) at time. This allows reconstructing the spectrum by measuring the intensity for each wavelength, namely we do a raster scan of the spectrum. The width in pixels of the line and the region where the raster scan is performed can be selected so that it is possible to adjust the resolution and the spectral range of the spectrometer.

Multiplex mode: in this mode we do a single pixel imaging, degenerate along one dimension, in which the pixels of the DMD are activated according to particular patterns derived from Hadamard-Walsh matrices. These matrices, usually indicated with H, are particular square matrices, whose entries are either 1 or -1, obtained with a recursive construction, called Sylvester construction, thus defined:

$$H_{2^n} = \begin{bmatrix} H_{2^n-1} & H_{2^n-1} \\ H_{2^n-1} & -H_{2^n-1} \end{bmatrix} \text{ with } H_1 = [1] \tag{3.4}$$

$n = 0, 1, 2, \cdots$ and 2^n is the order of the matrix that is equal to the size (N X N).
Each H matrix fulfills the following useful properties:

- $H = H^T = H^{-1}$;
- Rows (or equivalently columns) are mutually orthogonal.

Since the rows of a H matrix are orthogonal, they represent a set of N bases, called Hadamard bases, that can be used to decompose a generic vector. This operation is known as Hadamard transform and it works like a discrete Fourier transform.
Exactly Hadamard bases are employed, in this modality, as patterns for the collection the spectrum. Actually, we use a little modification of the original Hadamard so each entry h_{ij} is modified as:

$$\hat{h}_{ij} = \frac{h_{ij} + 1}{2} \tag{3.5}$$

Thus each -1 in Hadamard matrices becomes a 0. This preserves all the properties of original Hadamard matrices we mentioned but makes the generation of the patterns and the reconstruction of the spectrum easier. An example of patterns generated from a Hadamard matrix of order 16 is reported in figure 3.16.

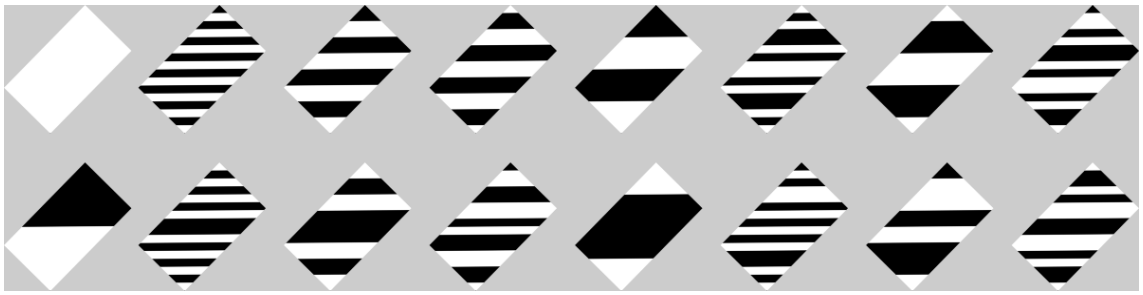

Figure 3.16: Example of the 16 patterns obtained from Hadamard matrix of order 16

The Hadamard bases are projected along the direction of dispersion of the grating creating a series of striped patterns. It is possible to define the region where to generate the pattern and the order N of the basis so to select the spectral range and the spectral resolution. Moreover, there is the possibility to order the patterns in a particular way, named cake-cutting ordering, described in reference [35], which allows a super sub-Nyquist acquisition (this function has been implemented and tested but not used during measurements).
Note that, since half entries of each H matrix are 0 and half are 1, each line is active for the 50% of the total measurement time so more signal is collected with respect to monochromator mode in which each line is active only for a time equal to total measurement time / number of lines. Nevertheless, in multiplex mode we measure the Hadamard

transform of the spectrum so we need a reconstruction process to get the real spectrum. The details of reconstruction will be presented in section 3.5.3.

Imaging mode: in this mode the imaging capability of the single pixel camera is fully exploited in order to retrieve an image of the light spot on the DMD. The patterns for imaging are derived from the Hadamard bases described in the previous mode but with a different disposition. In fact, each Hadamard basis of order N is reshaped in a ($\sqrt{N}$ x $\sqrt{N}$) matrix as shown in figure 3.17. Note that in this way the usable Hadamard

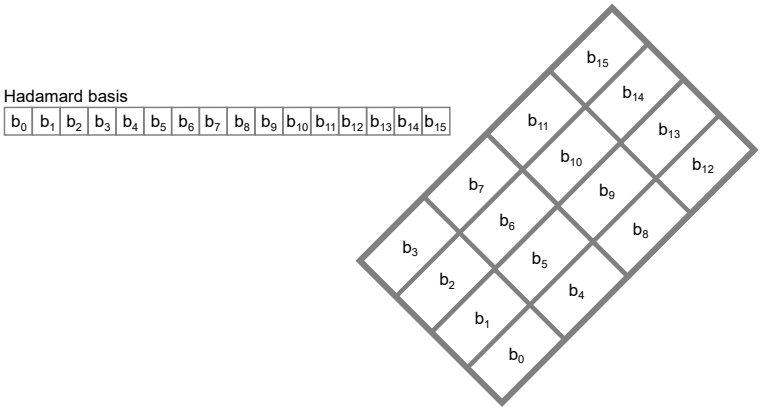

Figure 3.17: Reshape of Hadamard basis in the pattern for the DMD

matrices are only those for which $\sqrt{N}$ is an integer number. The order of the matrix also defines the resolution of the image: the higher order, the better resolution. This mode also offers the possibility to zoom on the image and reconstruct only a partial region. Moreover, the cake-cutting ordering can be applied enabling super sub-Nyquist acquisition. The measurement thus obtained needs to be elaborated to retrieve the actual image (see section 3.5.3 for further details). This mode has been developed during this thesis work in order to be able to achieve a precise alignment of the spectrometer even without the use of a beam profiler (further details about the alignment will be given in section 3.5.1).

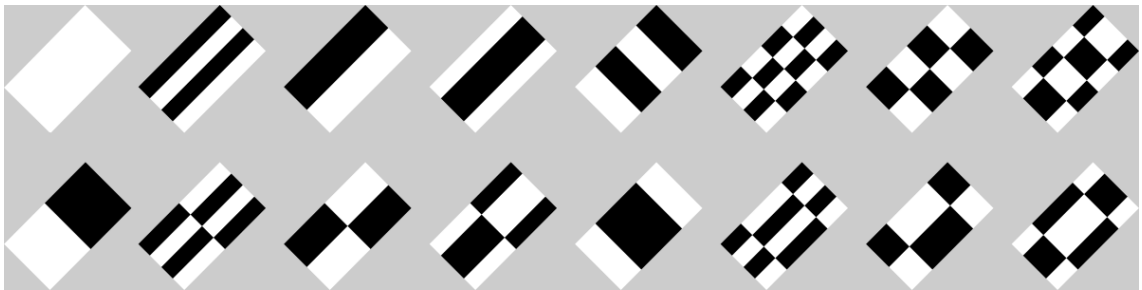

Figure 3.18: Example of the 16 patterns for Imaging Mode

3.4.3. Control system

All the patterns described above are generated by a program written by us in C language. The DMD is connected to its own driver and evaluation board (DLPLCR65EVM and DLPLCRC900EVM by Texas Instruments) that communicate with a computer through a USB interface exploited by our program to upload the patterns for the DMD. We use the "patterns on the fly" mode (see DLPC900 Programmers' Guide [36]), meaning that an entire sequence of the patterns we want to project on the DMD is uploaded at once on the internal memory of the evaluation board and then that sequence is run at a start command. Each pattern is a 1-bit depth bitmap image in which bits 0 and 1 correspond respectively to an orientation of -12° and +12° of the corresponding micromirror in the entire array. The images are encoded with enhanced Run-Length encoding (e-RLE) algorithm before being uploaded on the internal memory of the board in order to decrease their size on the memory. With these settings it is possible to reach a minimum exposure time for the single pattern of 105 µs and upload a maximum number of 512 patterns in multiplex mode. (Note this limitation is given by the RAM of the computer which saturates when we try to generate the patterns corresponding to 1024 Hadamard bases)
A synchronization by means of a trigger signal between the DMD and the TCSPC board automatically controls the start of the acquisition of a single temporal curve at the change of the pattern.
During the thesis work, in addition to the improvements and extensions to this program with respect to the previous version, we integrated it, using DLL libraries, in an existing program called TRS used in many laboratories of Politecnico di Milano.
Moreover, the Python code needed to reconstruct measurements has also been included in the TRS program using Python-C API functions [37] to run a Python script from the C program and share data between the two running processes.
The block diagram of the control software is shown in figure 3.19.
The main program is TRS which controls the workflow of the measurement procedures from the setting of the measurement parameters to the acquisition with the TCSPC board and the saving of raw data.
Before a measurement the TRS program calls the functions of the DMD control program contained in DLLs. There are two DLLs corresponding to the two main parts of the DMD control program. The first one, called *getBasis*, generates the bitmap images of the patterns according to the selected operation mode. The second part, called *dmd*, handles each passage which involves a communication between the computer and the DMD such as the uploading of patterns and the commands to start/stop the sequence of patterns.
Once the DMD is set it is possible to run the acquisition from the TRS program.

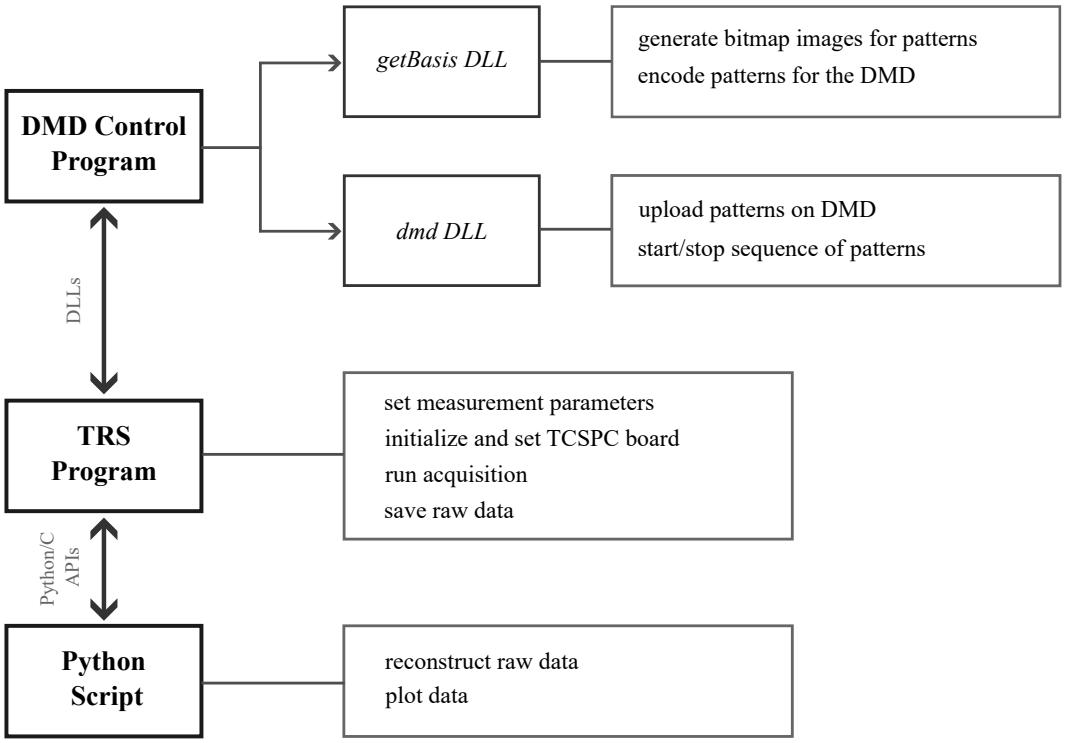

Figure 3.19: Block diagram of the control software

When a complete cycle of a sequence of patterns is completed, the Python script for reconstruction is executed thanks to Python/C APIs. According to the operation mode selected, raw data are reconstructed and plotted in a 2D map and a spectrum.
At the end, TRS takes control again to save data and to do another repetition of the measurement or to conclude the measurement.
Note that, since the Python script is independent of the TRS program, it is possible to modify it so to change the reconstruction process or the style of the plots without changing the source code of TRS.
This integration of different programs makes the usage of the instrumentation faster and easier, since only one program is needed, and allows a quasi-real time reconstruction of measurements needed when the spectrometer is used in Imaging mode for its alignment.

3.4.4. Characterization and performances

In this section are reported some calculations and measurement done in order to characterize the system and know its performances before the usage for measurements.

Spectral range

The spectral range of our spectrometer is limited by the size of the DMD. In fact, we are able to collect the spectrum imaged by the grating only on the surface covered by micromirrors of the DMD. Using the imaging mode and changing the wavelength of our tunable Ti:Sapphire laser we identified the range of wavelengths that fall onto the surface of the DMD. The spectral range experimentally verified is 60 nm corresponding to 800 cm^{-1}. Actually, the collected spectrum suffers of vignetting so the collection efficiency at the borders of the DMD is lower than in the middle and the effective spectral range is slightly lower than that measured. This fact is due to the lenses which are too small to correctly collect the angled rays from the dispersion grating and the DMD.
The spectral range of our spectrometer is small compared to that of usual Raman spectrometers: that means we need to know a priori the Raman spectral features we want to observe and then align the spectrometer in order to collect those wavelengths. In fact, by moving the DMD and changing the inclination of the dispersion grating, it is possible to align our spectrometer in a different spectral region and observe different Raman features. To increase the spectral range we should change the dispersion grating and choose one with less grooves/mm (actual 1200). However, this would reduce the resolution of our spectrometer making more difficult the separation of very near Raman peaks.

Spectral resolution

The best spectral resolution our instrument could potentially reach is fixed by the size of a single micromirror on the DMD and can be obtained dividing the spectral range previously measured by the number of micromirrors lines on which the spectrum is imaged. Since the DMD is oriented diagonally, the spectrum falls only on 2160 of the 3000 diagonal one-micromirror lines thus the resolution can be calculated as:

$$\frac{(spectral\,range)}{2160} = 0.027\text{nm/px} \tag{3.6}$$

However, there are many factors which make difficult the achievement of this value.
The first one is the width of the line of micromirrors activated at each time. In monochromator mode this parameter can be manually selected while in multiplex mode it is defined by the order of the Hadamard basis used. Knowing the linewidth of activated micromirrors, the spectral resolution is given by the following formula:

$$\frac{(spectral\,range)}{2160} * linewidth = \frac{(spectral\,range)}{2160} * \frac{3000}{\#(HadamardBases)} \tag{3.7}$$

In table 3.2 we reported the linewidths and the spectral resolutions corresponding to the number of bases used in multiplex mode.

#Bases	linewidth	resolution [nm]
32	93	2.583
64	46	1.278
128	23	0.639
256	11	0.306
512	5	0.139

Table 3.2: Limit of spectral resolution corresponding to the micromirrors linewidth

The second factor which limits the spectral resolution is the entrance slit of the spectrometer. Since the optical system creates a 1:1 image of the entrance slit onto the DMD, the minimum spot possible has the same size of the entrance slit. Thus, in this case the value of spectral resolution can be obtained as:

$$\frac{(slit\,size)}{7.5\mu m} * \frac{(spectral\,range)}{2160} \tag{3.8}$$

We are using a slit of 100 µm so this value is equal to 0.36 nm.
The third limiting factor for the spectral resolution is due to the alignment of the lenses in the spectrometer. In fact, if the lenses are not precisely placed we will have aberrations or a magnification greater than 1, thus the spot on the DMD will be larger than that expected. Note that this factor cannot be calculated and depends only on our skill in aligning the optical components.
In conclusion, the spectral resolution can be estimated taking the largest value obtained from the formulas above but the actual resolution must be measured experimentally.
We have measured experimentally the resolution (FWHM) obtained with the fiber bundle plus the slit and we tested the best resolution we were able to obtain using a monomode fiber with a core diameter of 4.4 µm (thus the slit does not limit the spot size). Both measurements were taken in the raster scan mode with a linewidth of 2 micromirrors.
The results are shown in figure 3.20.
In the first case we obtained a value of 0.8 nm while in the second case 0.1 nm.
Comparing the experimental values with the estimations from the formulas above we can affirm that the actual resolution is mostly limited by non-idealities or not enough precision in the optical system.
However this is still a good resolution, comparable to that of commercial Raman spectrometers. It is possible to improve the actual resolution by mounting a narrower slit. Nevertheless, this would increase the losses and reduce the detectable signal. A trade

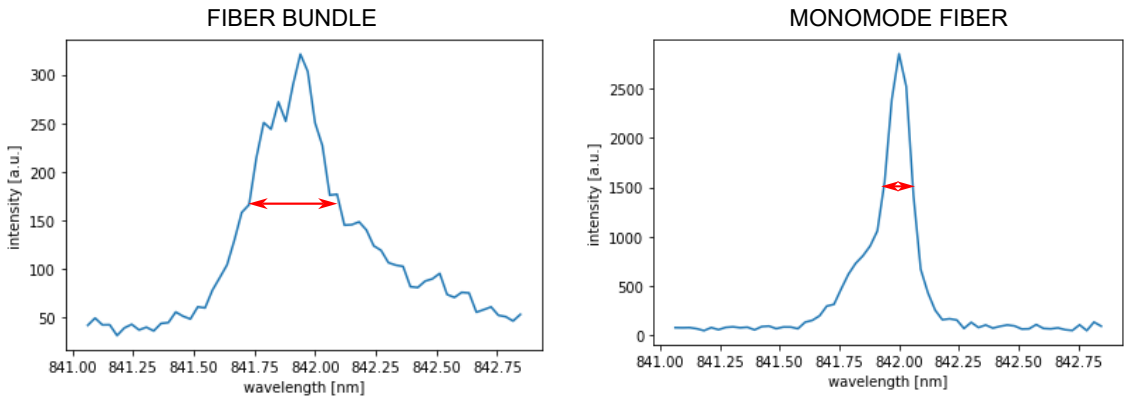

Figure 3.20: Experimental measurements of spectral resolution

off between spectral resolution and signal intensity has to be found. In fact, we want a high spectral resolution in order to distinguish the narrow and sometimes dense peaks of Raman spectra but without losing much intensity since Raman signal is low yet before entering the spectrometer.

Spectral efficiency

To experimentally measure the spectral efficiency of our spectrometer, defined as the ratio of the power at the detector and the input power with respect to the wavelength, we have to measure a flat spectrum, thus we can obtain directly from a measurement the spectral efficiency. For this measurement we used a white light signal from a lamp which has a nearly flat spectrum. The measure obtained, namely the spectral efficiency, is shown in figure 3.21.

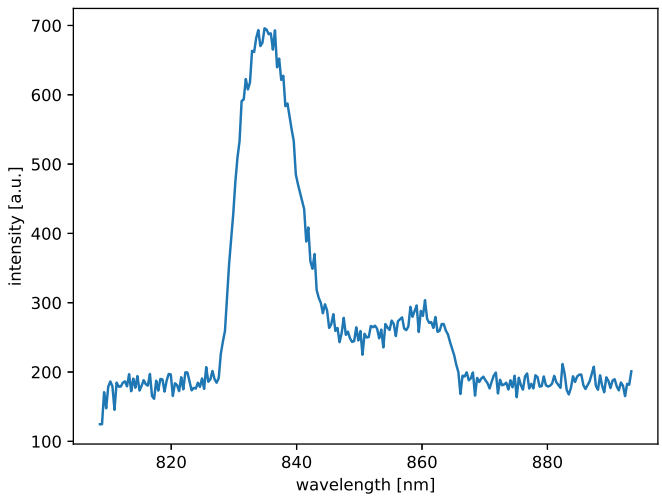

Figure 3.21: Spectral efficiency of our spectrometer

In general the best condition is to have a flat spectral efficiency so to detect all the wavelengths with the same efficiency thus preserving the relative difference between peaks of the original spectrum. Yet, it is clear that our spectrometer does not have a flat spectral efficiency at all. This fact is probably due to some vignetting caused by the lenses limited aperture and some not perfect alignment of all the elements of the spectrometer from the grating to the detector. However, this is not a drastic problem since it is possible to normalize the collected spectrum with respect to the spectral efficiency so to compensate the different efficiency for each wavelength.
Nevertheless, this normalization process has not been applied to the measurements taken in this thesis because in many cases it did not give a correct compensation of the spectral efficiency probably caused by the poor precision of the spectral efficiency measurement. In fact, we cannot be sure that the spectrum of the lamp used was perfectly flat to ensure a correct normalization.

Power Efficiency

Using a thermopile connected to a powermeter, with the laser in CW to have sufficient power, we measured the power of the light beam at many intermediate positions of the spectrometer. This measurement allows us to determine the efficiency of the spectrometer, defined as the ratio of the power reaching the detector and the power before the entrance slit of the spectrometer, as well as to get knowledge of the most critical parts where losses are greater.

position	**elements involved**	**power [mW]**	**eff.** (P_i/P_{i-1})
0) before fiber bundle	/	363	/
1) before entrance slit	fiber bundle	300	0.826
2) on DMD surface	slit + L1 + grating + L2	37	0.123
3) on detector surface	DMD + L3 + L4	13	0.351

Table 3.3: Power measured at different points of the spectrometer

The total efficiency (P_3/P_1) is 4.3%.
That is a very low value not helpful to detect the low signal of Raman scattering.
Most of the losses come from the slit and the reflective dispersion grating. However, this is unavoidable. In fact, the slit is necessary to keep a high resolution to detect Raman peaks. Instead, concerning the grating, we can exploit only the light from the first order of diffraction while the light of 0-th order or successive orders is completely lost.

Stability

To check the stability of our spectrometer, we measured repetitively the laser spectrum (assumed to be stable) for one hour. The measurement was taken using the monomode fiber with 4.4 µm core so to obtain the narrowest peak possible in the spectrum. The spectrometer was in the Raster scan mode with 32 lines of 2 pixels width centered on the peak of the spectrum and a single pattern exposition time of 0.1 s. The obtained spectra have been superimposed on the same graph in figure 3.22. Moreover, we calculated the position of the maximum for the spectrum of each measurement.

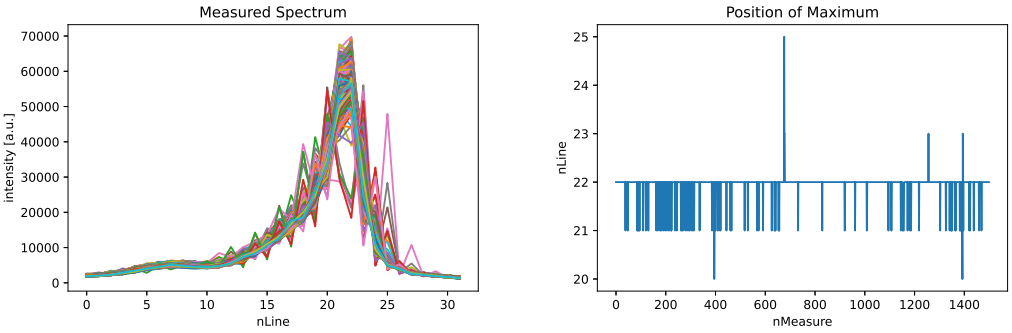

Figure 3.22: Spectra for all the measurements (on the left), position of the maximum of the spectrum for each measurement (on the right)

It is possible to note that in general our spectrometer has a good stability as the peak in the spectrum falls almost always in the same position with deviations of 2 pixels which, according to our calculations on spectral resolution, corresponds about to 0.06 nm. However, in some measurements both the peak position and the shape of the spectrum changed. We noticed that this fact is due to vibrations which influence the mechanical part comprising the first part of the spectrometer (fiber + slit + L1), thus also the image on the DMD is affected by vibrations. This problem can surely be solved by a more stable mechanical mounting for these optical elements.

3.5. Measurement procedures

In this section the procedures needed to obtain a measurement are presented. We start from the alignment of the spectrometer, then we will move to more frequent procedures, needed before every measurement, and in conclusion we will present how to reconstruct raw data in order to obtain the Raman spectrum and its temporal evolution with gating and depth profiling.

3.5.1. Alignment

Since, as we have seen, our spectrometer has a narrow spectral range, we need firstly to properly select the spectral region we are interested in. For example, in our case we wanted to see the Raman peak of marble ($CaCO_3$) at 1080 cm^{-1} then, being the excitation wavelength $\lambda = 780$ nm, we know that the spectrometer needs to be aligned so to collect a wavelength of 850 nm. To do that we exploit the tunability of our Ti:Sapphire laser setting its wavelength to $\lambda = 850$ nm.
Now it is possible to proceed with the alignment with the following operations:

- Alignment of the fiber with the entrance slit: the linear end of the fiber bundle must have the same orientation of the slit. To do that we have to rotate the fiber until the transmitted power after the slit is maximized.
- Alignment of the dispersion grating: the dispersion grating must be tilted so that the diffracted beam goes parallel to the optical table and passes through the center of the lens before the DMD.
- Alignment of the DMD: the DMD must be placed so that the spot focused by the lens is at the center of its surface. Moreover the device has to be tilted so that, when all mirrors are active, light goes next to the first lens and can be completely collected by the second lens.
- Alignment of the detector: the lenses in front of the detector must be placed in order to collect all the light coming from the DMD and the active area of the detector has to be placed in the image plane of this optical system.

After these operations, the alignment needs then to be refined.
The first lens and the longitudinal position of the DMD have to be adjusted such that aberrations are reduced, the spot on the DMD is minimized and the maximal spectral resolution can be achieved. For this operation we can exploit the imaging mode of the DMD and the real time reconstruction of the image integrated in the TRS program. This allows a visualization similar to that of a beam viewer (see figure 3.23).
Although our instrument has a lower resolution and a lower refresh rate (1 image every about 3 s) with respect to a beam viewer, it has the big advantage of using directly the DMD. In fact, if we use a beam viewer, we will position it in the place of the DMD to optimize the spot but when the DMD will be set again in its position, the spot on its surface will be different than that observed on the beam viewer because of this repositioning.
In conclusion, as last step to refine the alignment, the position of the detector must be adjusted by maximizing the number of photons counted by the TCSPC board when all

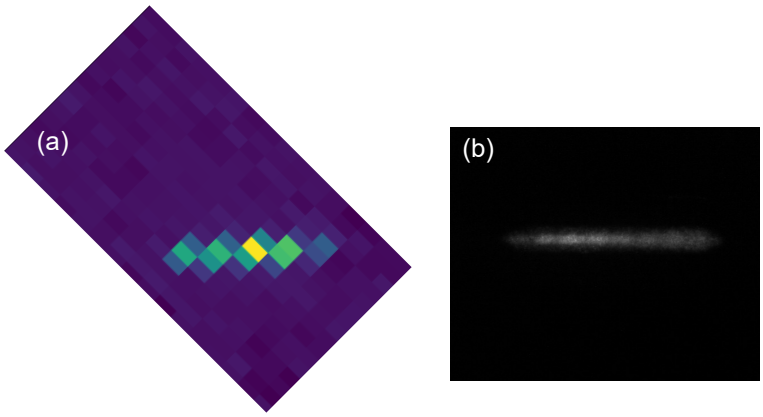

Figure 3.23: Comparison between the image of the spot on the DMD obtained with our system (a) and a beam viewer (b)

mirrors of the DMD are active. Then, as a further control, it is possible to input a white light in the spectrometer and use again the imaging mode to verify the region of the DMD seen by the detector.
These alignment procedures must be repeated whenever we want to change the spectral region observed by the spectrometer.

3.5.2. Measurement

As a first step to obtain a measurement we need to place the sample under the probe and adjust the probe to the correct position. In fact, firstly, the surface of the sample must be on the conjugate plane of the input the fiber connected to the probe, secondly, the collection region and the illumination one must be centered the one with respect to the other. In particular for point illumination the collection spot of the probe and the illumination spot must be on the same point while for the ring illumination scheme the collection region must be at the center of the annular illumination (see figure 3.9). We exploited a diode laser (PDL 800 by PicoQuant) inserted in the probe from the fiber side to center the collection region of the probe and the illumination region.
Once the probe is in the correct position the measurement parameters can be set on the TRS program. It is possible to choose the mode of the DMD, the settings about the patterns, the exposition time t_{exp} for each pattern of the DMD and the number of repetitions n_{rep} for a single measurement. The total time of measurement can be calculated as $t_{exp} \times \#(Patterns) \times n_{rep}$.
All the raw data are saved to a binary file while during the measurement, thanks to the integration of the reconstruction code in the TRS program, it is possible to see a preview of the reconstruction of the last repetition done.

3.5.3. Reconstruction

From the measurement we have raw data, namely the time behavior of the signal for each single pattern shown on the DMD. If we are using the raster scan mode, raw data show directly the spectrum and its time evolution as in figure 3.25, while if we are using the multiplex mode raw data are similar to figure 3.24 and a reconstruction process is needed to retrieve the original spectrum.

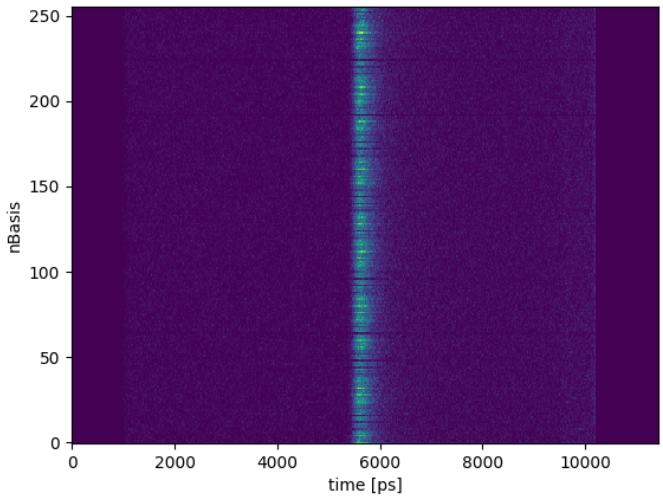

Figure 3.24: Raw data, multiplex mode (sample: marble)

In this case, the original image of the spectrum created on the surface of the DMD by the diffraction grating is obtained applying the inverse Hadamard transform to raw data. In particular, the vector containing raw data $\mathbf{x}$ has to be multiplied by the inverse Hadamard matrix H^{-1} in order to obtain the reconstructed data $\mathbf{y}$. Since $H^{-1} = H$ we have:

$$\mathbf{y} = H^{-1}\mathbf{x} = H\mathbf{x} \tag{3.9}$$

Actually we use a least square minimization algorithm to calculate the vector $\mathbf{y}$:

$$\min \|\mathbf{y} - H\mathbf{x}\|_2 \tag{3.10}$$

This allows a more robust reconstruction which can work even in the case the number of measurements is smaller than the number of bases of the Hadamard matrix (super sub-Nyquist acquisition).
This procedure must be repeated for each temporal slot so to obtain a 2D map in which the y axis is for the spectrum while the x axis is for the time, like that in figure 3.25.

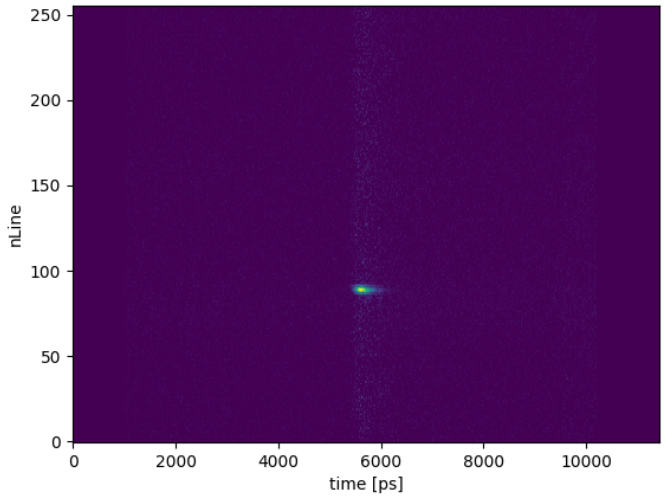

Figure 3.25: Reconstructed data: 2D map

It is possible then to do different analysis.
By summing the temporal signal over a time gate one obtains the Raman spectrum of the sample. It is possible to freely choose the length of the time gate and its position. Choosing a very long gate including all the signal as in figure 3.26 one obtains a CW measurement like in SORS. While selecting different time gates enables the visualization of the Raman spectrum of different depths in the sample, as will be shown in experimental measurements in chapter 4.

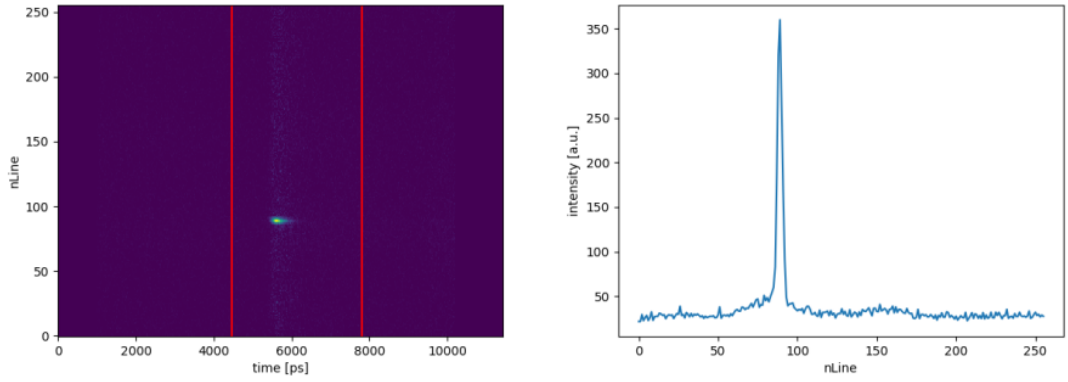

Figure 3.26: Reconstructed data: 2D time gating and spectrum

By slicing the 2D map in the horizontal direction it is possible to view the temporal behavior of a specific wavelength, or equivalently Raman shift, as in figure 3.27.

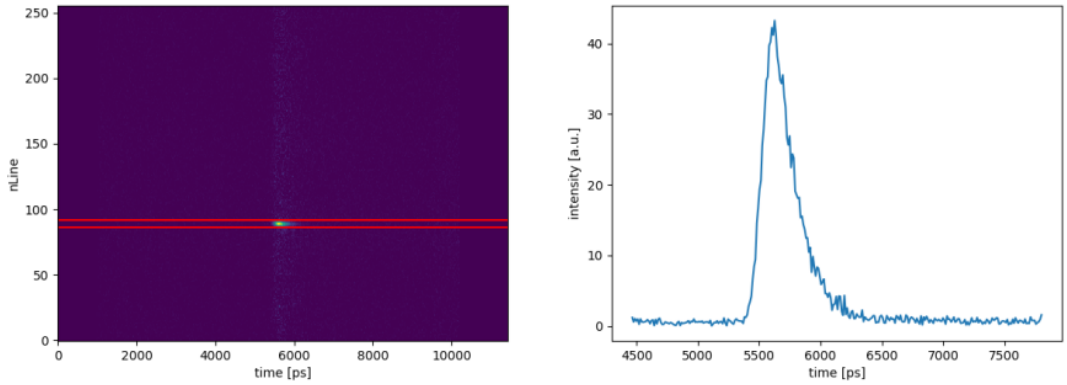

Figure 3.27: Reconstructed data: 2D slicing and time evolution

During our experimental activity we noticed a critical point of the reconstruction process for multiplex mode. In fact, in some measurements we observed very narrow spikes, consisting of one single point, appearing in the spectrum. We found out that these spikes are present when the measured spectrum is almost flat, thus the detected intensity for different patterns has a very small change, and the detected intensity for each pattern has a decreasing trend. These conditions give in fact a line with a negative slope for the measurement before reconstruction which is responsible of the appearance of the spikes, as shown in figure 3.28 (note that in this measure the spectral efficiency is different because of a different alignment of the spectrometer).

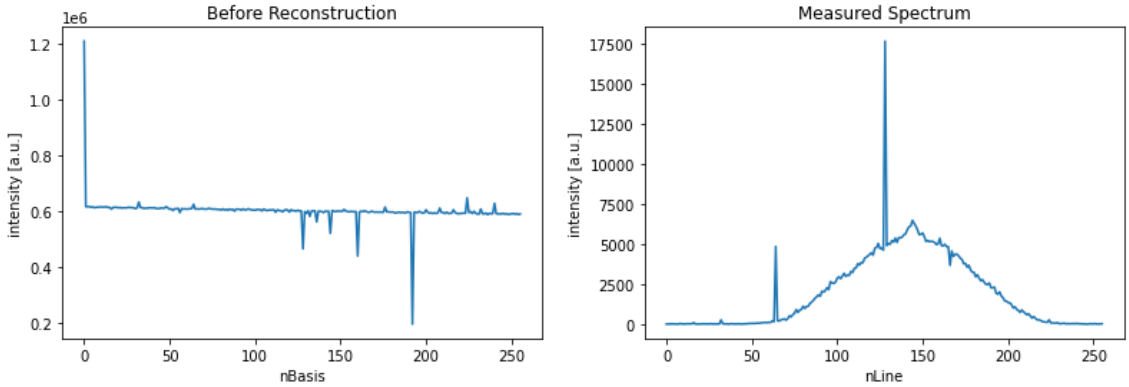

Figure 3.28: Presence of spikes in a measurement

To prove this assumption we considered a signal made of a line with a negative slope (obtained from a linear interpolation of the measurement) to which we applied the inverse Hadamard transform, as we do in the reconstruction process of measurements. From figure 3.29, it is possible to note that it is exactly this behavior of the signal which gives the same spikes observed during measurements.

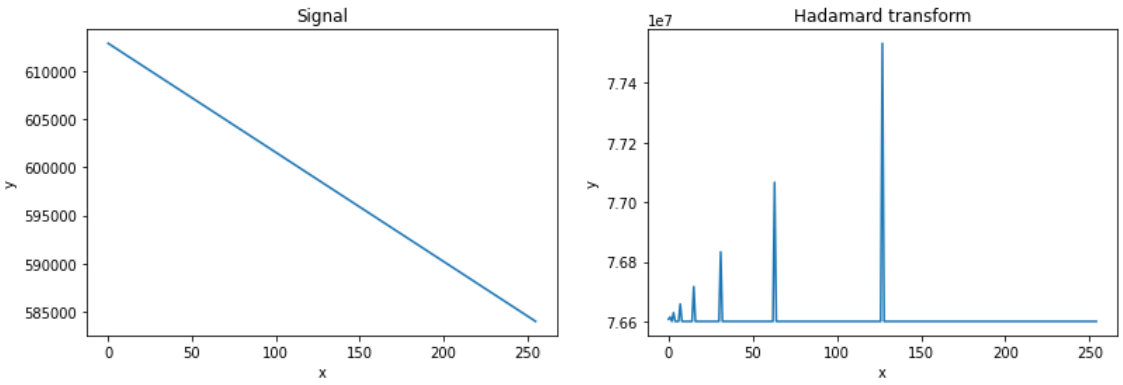

Figure 3.29: Demonstration of the origin of spikes

We noted also that similar spikes are generated if the signal is subjected to a sudden decrease, like a step.
We attributed the origin of these spikes to a decrease in time of the laser power which, as a consequence, gives the decreasing behavior of the detected intensity with respect to the sequence of patterns.
These artifacts are very critical in our case since the peaks can be misinterpreted as Raman peaks. As a solution, we saw that, by means of a linear fit, it is possible to add a correction at the measurement before the reconstruction in order to straighten the line. Otherwise we can reduce the exposition time for the single pattern t_{exp} and increase the number of repetitions n_{rep} to keep the same total measurement time, in this way the effect of the decrease of laser power on the measurement is greatly reduced and the spikes disappear. This last one is the best solution because it avoids modifying the measurement so one should adopt this, but, if the measurement has already been taken and cannot be repeated, the first method must be used.
Note that if the measured spectrum, instead, has intense and pronounced peaks, the problem of the spikes does not present because the detected intensity for each pattern is very different and even if the laser power decreases during the measurement its effect is not visible.

3.5.4. Calibration

Only missing thing is now the calibration of the spectrometer which is needed to correctly assign a scale of wavelengths or Raman shifts to the x axis of the spectrum.
This procedure can be done in two different ways.
If we need an axis with the wavelengths, it is possible to exploit the laser tunability to calibrate the spectrometer. In fact, taking many measurements of the laser spectrum,

each one with a different wavelength, we can identify the positions of the peak for each wavelength and obtain an axis scale by a linear interpolation of these data.

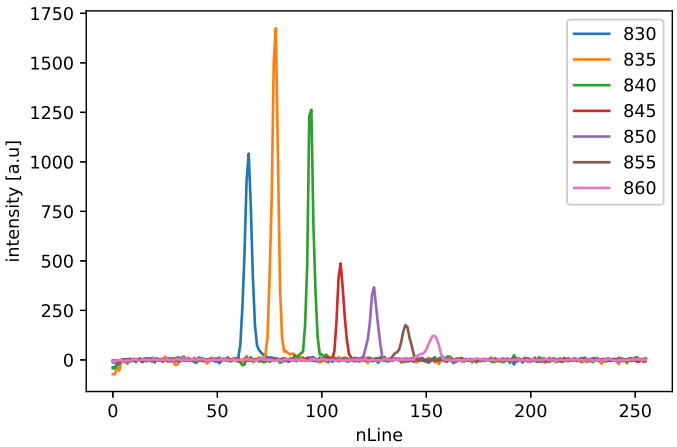

Figure 3.30: Calibration exploiting laser tunability

If we need an axis with the Raman shifts, we can calibrate the spectrometer using known Raman peaks. For example, in our case we used the Raman peaks of Marble ($CaCO_3$) at 1080 cm^{-1} and of Hydroxyapatite ($Ca_{10}(PO_4)_6(OH)_2$) at 960 cm^{-1}. Taking one measure of the Raman spectrum for each sample allows identifying the positions of these two peaks and obtain a scale for the axis of the spectrum by a linear interpolation of these data.

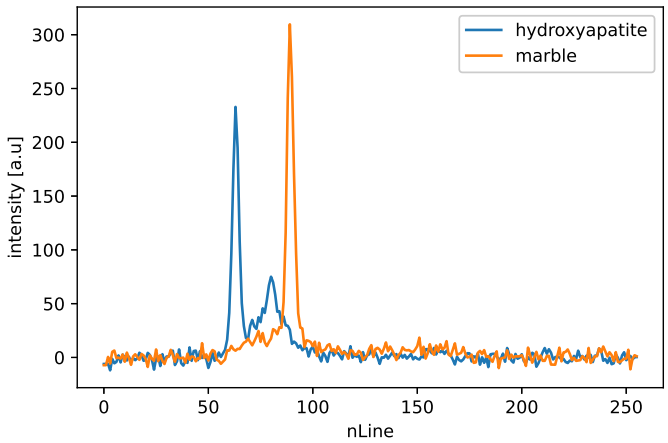

Figure 3.31: Calibration exploiting known Raman peaks

The calibrations obtained from the two methods are substantially equivalent. The link between them is given by the conversion from wavelength to Raman shift that can be done thanks to equations (1.10) and (1.11) once the excitation wavelength is known. The choice

of one or the other method depends on the spectral range observed and the availability of samples for which the Raman spectrum is known even though it is better to choose the method which gives directly the wanted axis without the need of a conversion.

4 | Experimental Measurements

After having characterized our spectrometer, we tested its performances by measuring Raman spectra of some samples. In this chapter we present and analyze these measurements comparing them to reference measurements and interpreting them with theoretical elements. We will start from measurements of homogeneous materials to verify the capability of our instrument to correctly collect a Raman spectrum and then we will move to measurements of bilayer materials in order to demonstrate the efficiency of our TD Diffuse Raman Spectrometer in doing depth profiling of multilayered materials. Moreover, the measurements concerning the bilayer material will be exploited to validate the calculations about generation depth of Raman photons done in section 2.2. At the end of the chapter a test of an in vivo measurement is also reported.

4.1. Samples description

Before showing the experimental results, we report in this section some important details about all the samples employed during the measurements we are going to analyze in the following.
We have four samples:

- **Marble**: this sample consists in a small block of marble, a metamorphic rock made of carbonate minerals, mostly calcite ($CaCO_3$) and dolomite $(CO_3)_2$. The interesting thing for us is that these minerals have a narrow and intense Raman peak at 1080 cm^{-1} which is easily detectable by Raman spectrometers.
- **Hydroxyapatite powders**: this material is a natural mineral with chemical composition $Ca_{10}(PO_4)_6(OH)_2$. This mineral exhibits a narrow and intense Raman peak at 960 cm^{-1} which makes also this material easily detectable by Raman spectrometers.
- **Silicone/PDMS**: this sample consists in slabs with different thicknesses made of a silicone polymer (Polydimethylsiloxane – PDMS) with addition of black ink and titanium oxide to obtain a precise absorption and scattering coefficient. These

samples have been exploited mainly to build the bilayers.

- **Bone**: bone tissue is also a good candidate to be easily detected by Raman spectrometers. In fact, it is composed of 65 – 70 % of hydroxyapatite in a collagen matrix, so it is expected to give nearly the same signal of hydroxyapatite. In our case we used a raw pork rib that has been cleaned to expose the bone tissue.

4.2. Measurement protocols

We define now the protocols followed for every measurement.
There are two protocols each for one of the two types of measurements done: monolayer homogeneous medium and bilayer medium.
The **protocol for monolayer measurements** has the scope to just collect the Raman spectrum of the sample, thus we use only a point illumination scheme ($\rho = 0$). Each measure is taken in the multiplex mode with 256 Hadamard bases, 1 repetition and 0.5 s of single pattern exposure time (the total measurement time is 128 s). In the measurement of the PDMS sample the number of repetitions was increased to 15 due to the lower Raman signal of this material.
The **protocol for bilayer measurements** is aimed at demonstrating the depth profiling capability of TD-DIRS depending on the variation of illumination setup, optical parameters (scattering) of the sample and thickness of the top layer. For this reason we fixed the measurement settings to: spectrometer in multiplex mode with 256 Hadamard bases, 15 repetitions and 0.5 s of single pattern exposure time (the total measurement time is 32 minutes). And we repeated the measure for: two different illumination setups (point illumination scheme $\rho = 0$, ring illumination scheme $\rho = 5$ mm); three different scattering coefficients (5 cm^{-1}, 10 cm^{-1}, 15 cm^{-1}) and two top layer thicknesses (0.5 cm, 1 cm).
In both protocols the laser power on the sample is of 70 mW and the excitation wavelength is 780 nm.

4.3. Monolayer measurements

In this section we show the measured Raman spectrum for each sample described in section 4.1. Each measurement is compared to a Raman spectrum of the same material taken from a reference or with a different instrument in order to validate the capability of our spectrometer to correctly collect a Raman spectrum. Note that since the material is homogeneous and we are not interested in depth profiling we will take a large time gate to include all the signal (time gate is shown by vertical red lines in the 2D map).

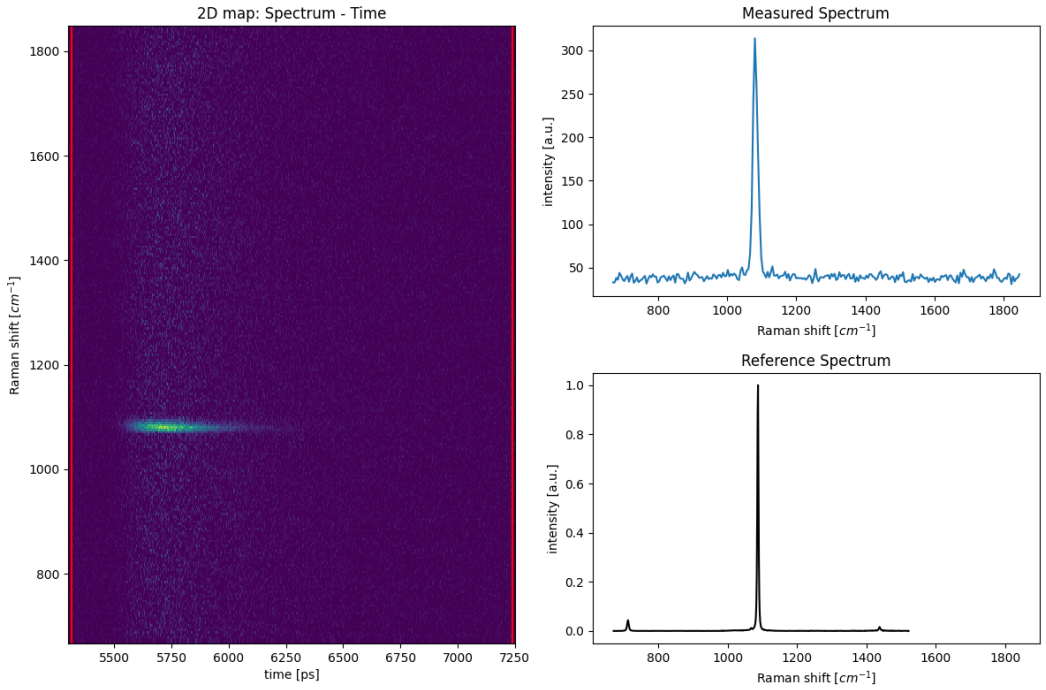

Figure 4.1: Monolayer measurement. Sample = MARBLE (Reference spectrum from rruff.info)

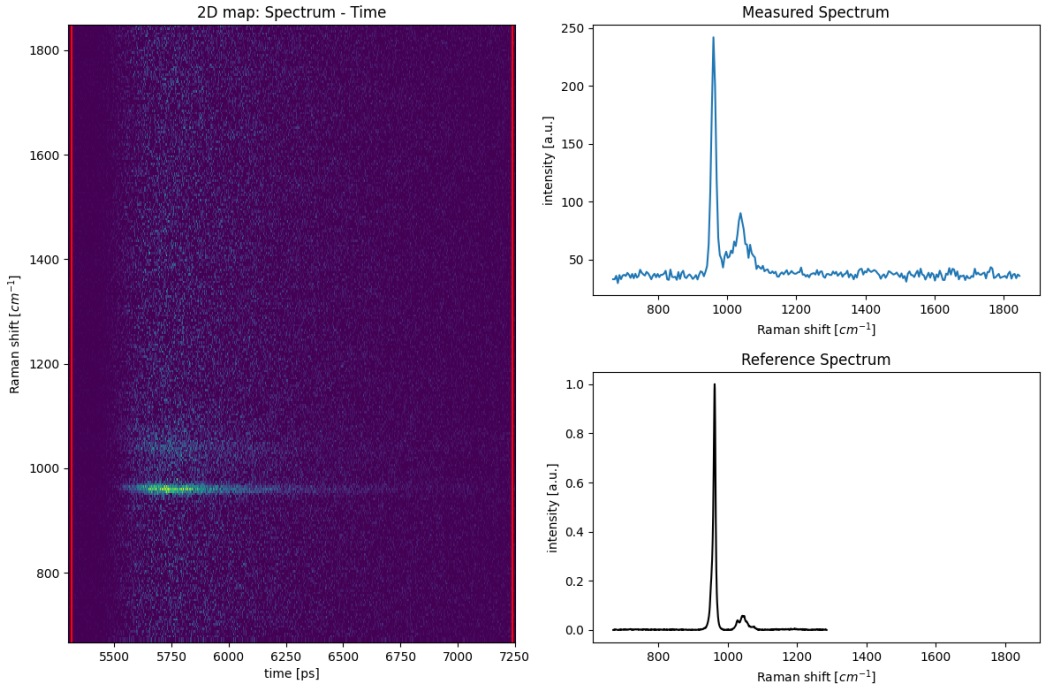

Figure 4.2: Monolayer measurement. Sample = HYDROXYAPATITE (Reference spectrum from rruff.info)

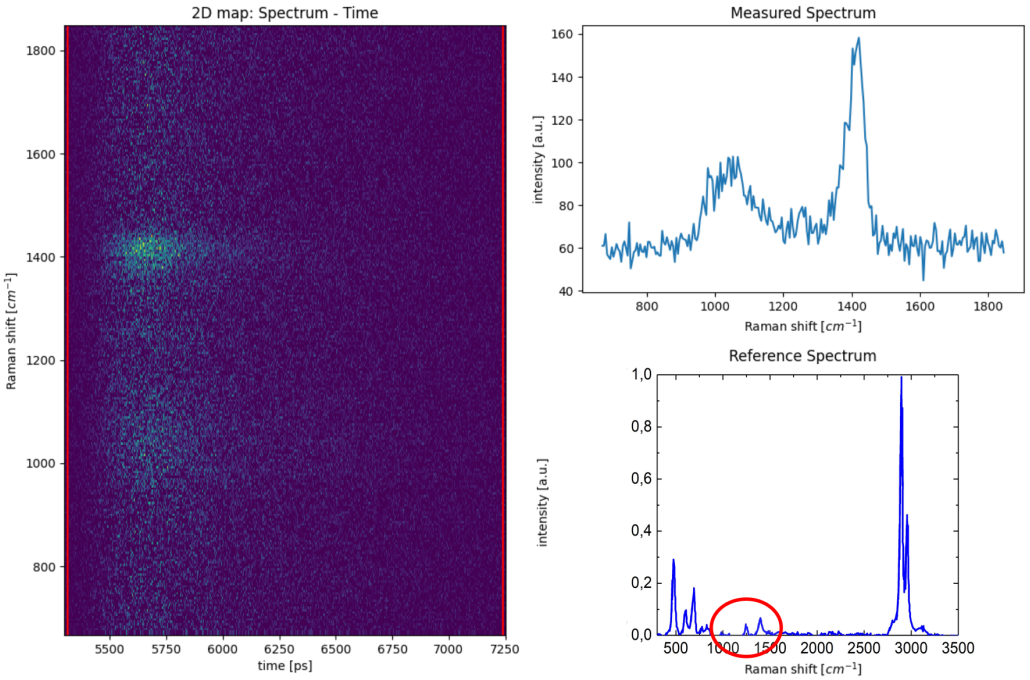

Figure 4.3: Monolayer measurement. Sample = SILICONE (Reference spectrum from ramanlife.com)

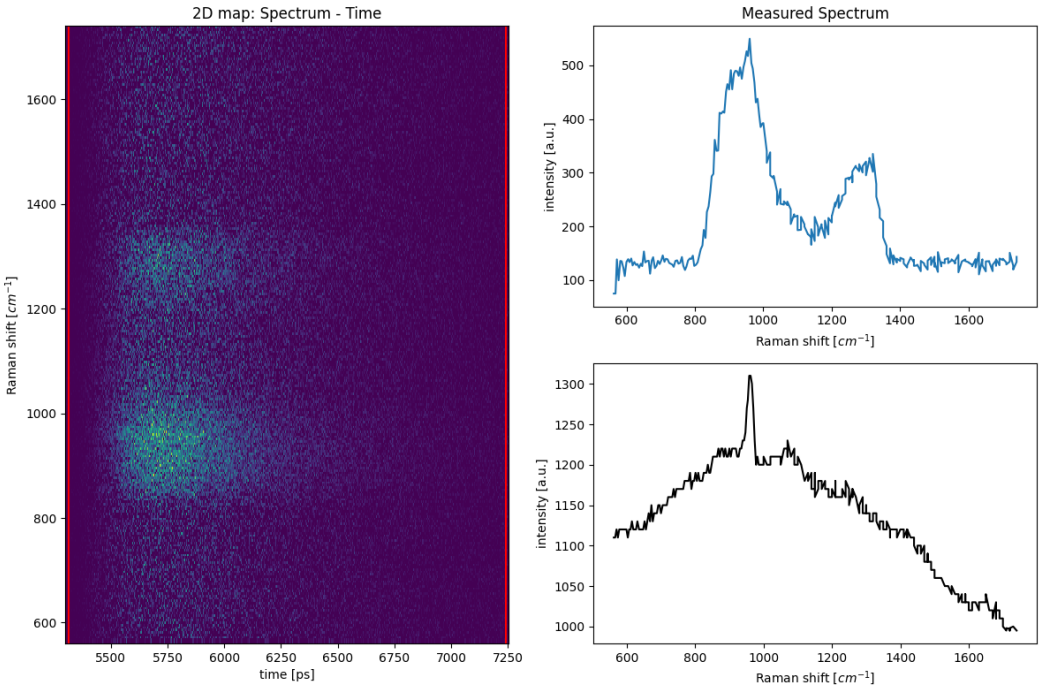

Figure 4.4: Monolayer measurement. Sample = BONE (Reference spectrum collected with a Raman spectrometer setup at Politecnico di Milano)

It is possible to see that our spectrometer was able to correctly collect the Raman spectrum of all the samples. Nevertheless, we can observe some small issues.

If we look at the spectrum of hydroxyapatite (figure 4.2), we can see a little difference between the measurement and the reference considering the ratio of the two peaks. This difference is caused by the spectral efficiency of our instrument. In fact, looking at figure 3.21 we can see that the peak at 960 cm-1 falls in a region with lower efficiency with respect to the other peak.

If we consider the spectrum of PDMS (figure 4.3), we can see that because of the limited spectral range of our spectrometer we were not able to capture completely all the peaks. Moreover, we have to remark that since these Raman peaks have a low intensity, the total measurement time had to be increased in order to obtain this measurement.

In the case of the bone spectrum (figure 4.4), we can see instead that the Raman peak of hydroxyapatite is well reproduced, as it is in the correct position, but it is barely visible. That is because the other components of the bone create some fluorescence which covers the Raman signal. Note that this effect is not present in the other samples because the materials they are made of exhibit no fluorescence in this spectral region. In the next section we will see how to improve this measurement by rejecting the fluorescence signal.

4.4. Fluorescence rejection by time gating

As we have seen from the measurement done on the bone, fluorescence can be a big obstacle during measurements of Raman spectra. In fact, as explained in section 1.1.2, fluorescence generates light with a lower wavelength than the excitation one as also Raman scattering does.
Nevertheless, there is a big difference between the two phenomena: the photon conversion of Raman scattering is instantaneous while fluorescence occurs after some observable delay from the absorption event because the transitions between molecular energy levels are not instantaneous in this case. Measuring in Time Domain, we have the big advantage to exploit this difference to isolate the Raman signal from that of fluorescence. In fact, by time gating it is possible in principle to select some time slots in which only Raman signal is present and retrieve a pure Raman spectrum.

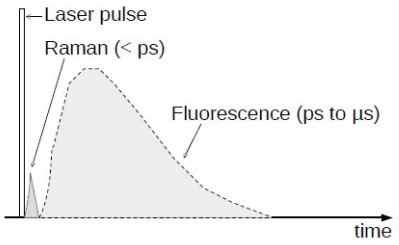

Figure 4.5: Time evolution of Raman and fluorescence signals (from [2])

If we look at the 2D map of our bone measurement, it is possible to note that the signal corresponding to the hydroxyapatite peak at 960 cm^{-1} reaches the detector earlier than the other detected signal.

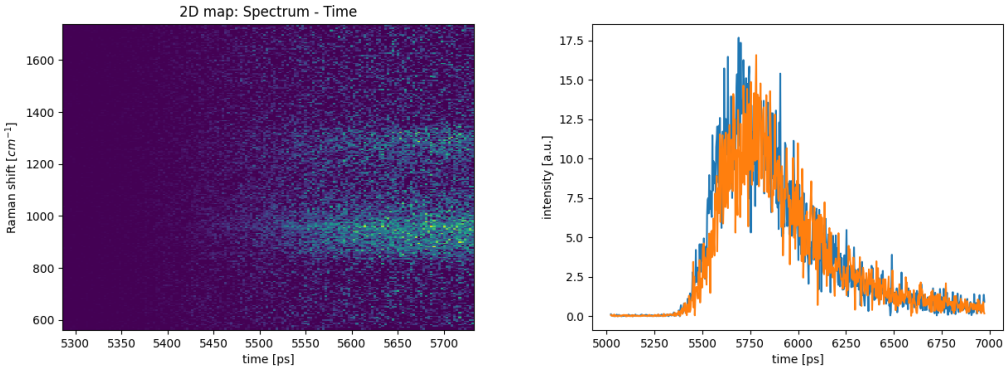

Figure 4.6: Zoom on the 2D map of the bone measurement and time behavior of the signal of 960 cm^{-1} (blue) and 900 cm^{-1} (orange)

We select then only the signal in a time gate of 140 ps at the rising edge of the pulse.

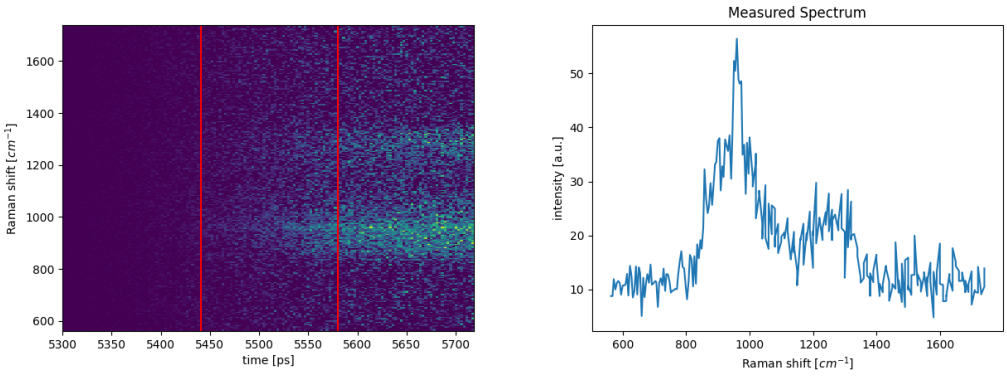

Figure 4.7: Time gated measurement of bone

Doing this procedure we have improved the Raman spectrum: rejecting some fluorescence, the Raman peak of hydroxyapatite is more visible than in the ungated measurement (figure 4.4). However, we have not been able to obtain a pure Raman spectrum and remove completely fluorescence. That is because the light diffusion in the material mixes up Raman signal and fluorescence thus the two signals are not completely separated in time and a simple time gating is not able to remove all fluorescence from the spectrum.

4.5. Bilayer measurements

Once we verified that our spectrometer is able to correctly provide Raman spectra, we moved forward by using it for its real scope: Time Domain Diffuse Raman Spectroscopy. We made then a bilayer medium by using the silicone slabs put on top of the marble block and we took measurements by varying the illumination scheme (point illumination scheme $\rho = 0$, ring illumination scheme $\rho = 5$ mm), the scattering coefficient of the silicone slab (5 cm^{-1}, 10 cm^{-1}, 15 cm^{-1}) and the thicknesses of the silicone slab (0.5 cm, 1 cm). In total we have 12 measurements.

In this section we will show these measurements and we will give only a descriptive interpretation while in the next section we will use a more quantitative approach in order to interpret some of these measurements in light of our calculations on the generation depth of Raman photons.

In the next two pages are collected the Raman spectra (without time gating) obtained from the 12 measurements. On the columns we have different top layer thicknesses while on rows we have different scattering coefficients. Each page instead refers to a different illumination setup.

	thickness = 0.5 cm	thickness = 1 cm
$\mu_s' = 5cm^{-1}$	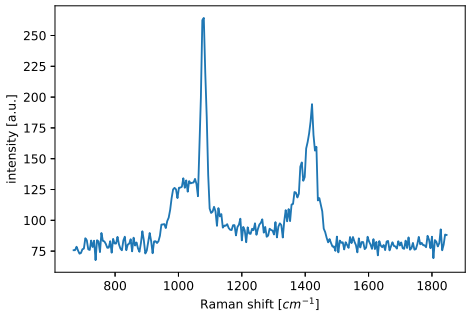	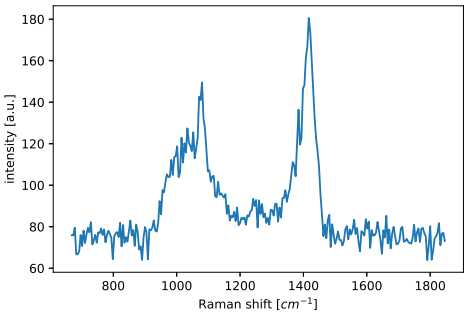
$\mu_s' = 10cm^{-1}$	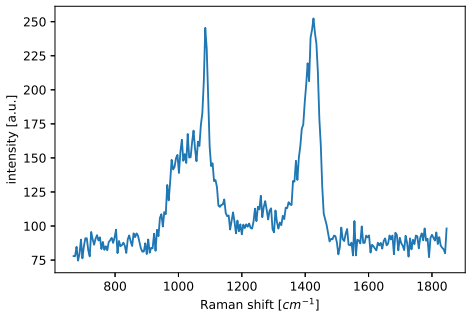	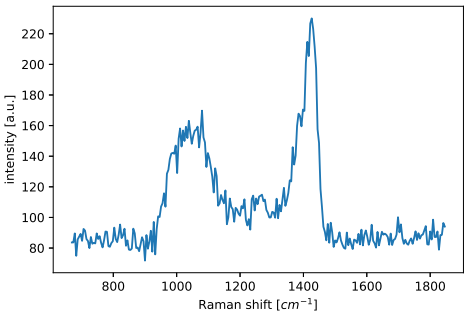
$\mu_s' = 15cm^{-1}$	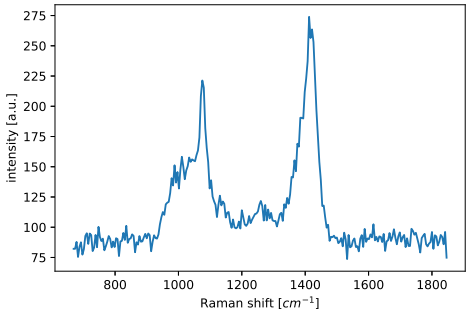	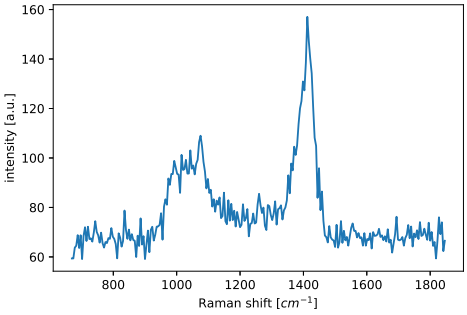

Table 4.1: Bilayer measurements $\rho = 0$ (point-illumination)

	thickness = 0.5 cm	thickness = 1 cm
$\mu_s' = 5cm^{-1}$	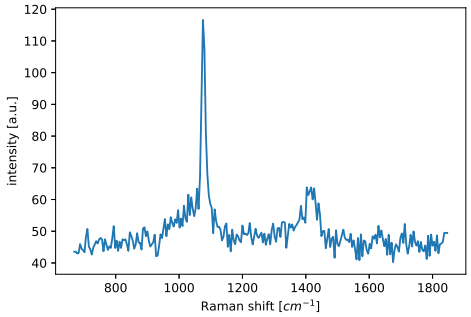	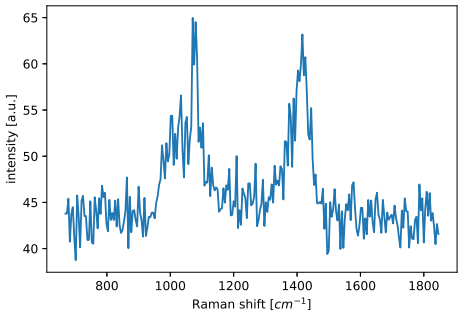
$\mu_s' = 10cm^{-1}$	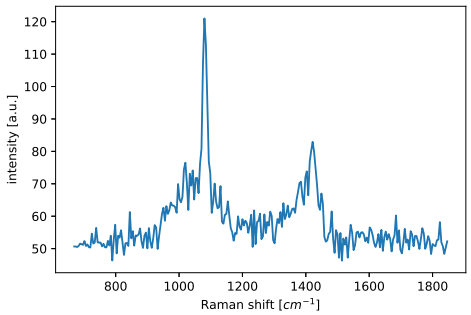	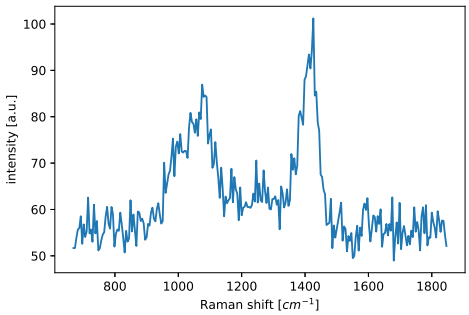
$\mu_s' = 15cm^{-1}$	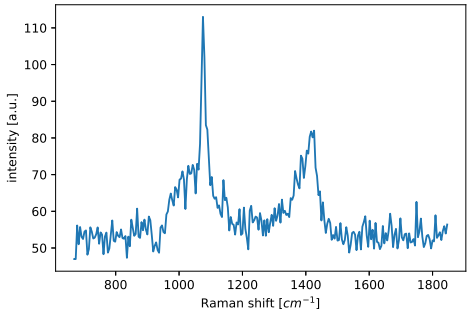	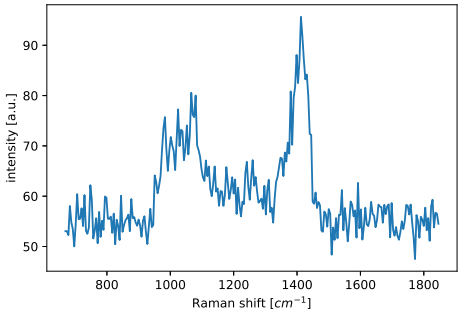

Table 4.2: Bilayer measurements $\rho = 5mm$ (ring-illumination)

We will now analyze the effect on the measurements of each variable we changed.

Effect of illumination scheme

Looking at the measurements it is possible to note that the change in illumination scheme varies the weight of the bottom layer with respect to the top layer in the measured spectrum. In particular, increasing the source-detector distance (from $\rho = 0$ to $\rho = 5$ mm), the Raman peak of marble at 1080 cm^{-1} (bottom layer) becomes much more evident with respect to the Raman peak of PDMS at 1400 cm^{-1} (top layer).
To interpret these results, we have to consider that since we are not doing time gating, thus integrating in time all the signal, our measurements are equivalent to SORS measurements. It makes sense then that by increasing the source-detector distance we select photons which come from deep layers of the material so the signal of the bottom layer becomes more evident than the signal of the top layer.
Moreover, looking at the 2D maps of two measurements of the same sample differing only for the illumination setup, it can be noted that the time evolution is substantially the same: meaning that the illumination setup has no effect on the time scale of the measurements.

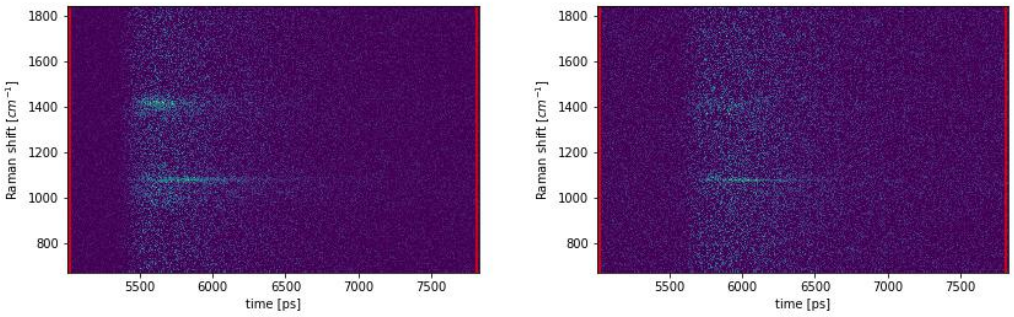

Figure 4.8: 2D map comparison of measure with $\mu_s' = 5cm^{-1}$, $th = 0.5cm$, $\rho = 0$ (on the left) and measure with $\mu_s' = 5cm^{-1}$, $th = 0.5cm$, $\rho = 5mm$ (on the right)

Thus it is possible to choose the point illumination scheme (which allows also collecting more signal) for a pure TD-DIRS approach and the ring-illumination in the case of a hybrid approach SORS + TD-DIRS to have a better selection of the bottom layer.

Effect of scattering

As the scattering coefficient of the top layer increases, we note that the spectrum of the top layer becomes more predominant with respect to the spectrum of the bottom layer: the Raman peak of PDMS increases while the peak of marble decreases. It seems then

that the average depth of collected photons shifts towards the surface of the bilayer thus giving the prevalence of the top layer spectrum.
This fact can be qualitatively explained considering that when the scattering increases, the photons are more diffused in the material so less photons reach the bottom layer to be converted by Raman scattering and less Raman generated photons of the bottom layer can reach the surface to be detected.

Effect of top layer thickness

From the measurements we can observe that the thickness of the top layer mostly influences the detection of the bottom layer. In fact, the intensity of the Raman peak of PDMS is nearly unchanged when the thickness of the silicone slab is increased while the peak of marble is subjected to a substantial decrease in intensity.
The reason of this behavior is that, by adding material on top of the bottom layer, excitation photons are more likely to be absorbed before reaching the bottom layer thus leading to a decrease in Raman photon generation and generated Raman photons are more likely to be absorbed before reaching the surface of the sample and being detected. Instead, the photon propagation in the top layer remains unchanged thus giving an independence of the intensity of the top layer spectrum from its thickness.
Also looking at the time evolution, it is possible to spot some differences when the thickness of the top layer is increased.

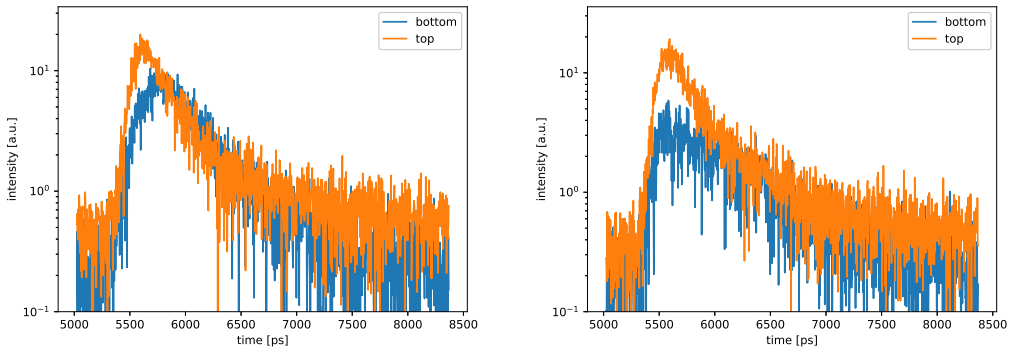

Figure 4.9: Time evolution comparison of measurements: $\mu_s' = 5cm^{-1}$, $th = 0.5cm$, $\rho = 0$ (on the left) and $\mu_s' = 5cm^{-1}$, $th = 1cm$, $\rho = 0$ (on the right)

We can see from figure 4.9 that the time evolution of the top layer is unchanged while the time evolution of the bottom layer shows a longer tail when the thickness of the top layer is greater. This fact is consistent with the longer diffusion of photons in the top layer when its thickness is increased.

Effect of time gating

We will now explore the effect of time gating on the measurements we presented before. With time gating we mean that, to obtain the spectrum, only a small temporal slot on the distribution of photon times of flight curve is selected and integrated. Since as we saw in chapters 1 and 2, times encodes depth, with this passage it is possible in principle to isolate the Raman spectrum of different layers of the sample.
We chose three time gates with the same duration of 200 ps: an early gate comprising the rising edge of the signal, a middle gate at the center of the pulse (225 ps after the starting point of the first gate) and a late gate placed on the tail of the temporal curve (450 ps after the starting point of the first gate).

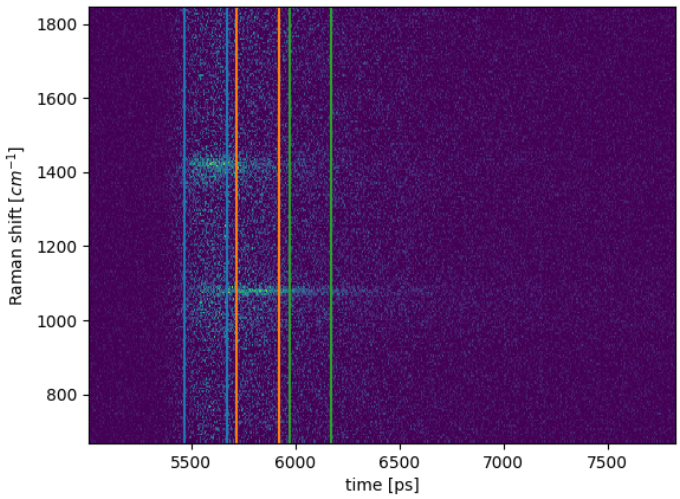

Figure 4.10: Time gates applied to the measurements

In the following two pages are reported the results of this analysis with the same organization as before: on the columns we have different thickness of the top layer, on the rows we have different values of the absorption coefficient and the two pages refer to different illumination setups.

	thickness = 0.5 cm	thickness = 1 cm
$\mu_s' = 5cm^{-1}$	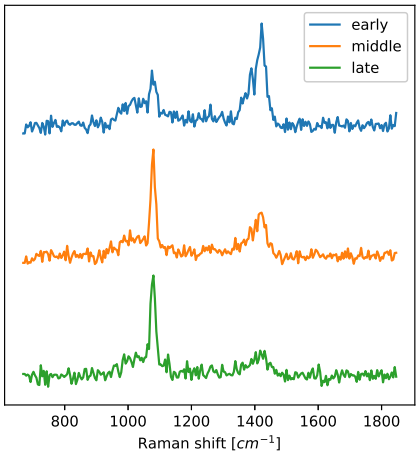	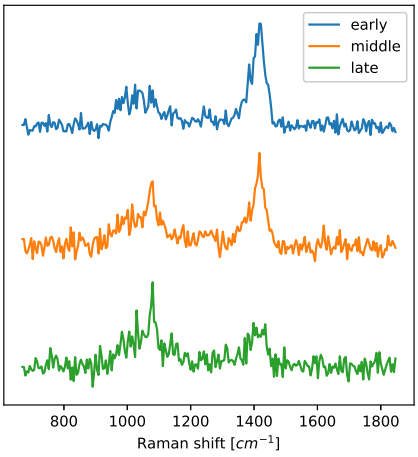
$\mu_s' = 10cm^{-1}$	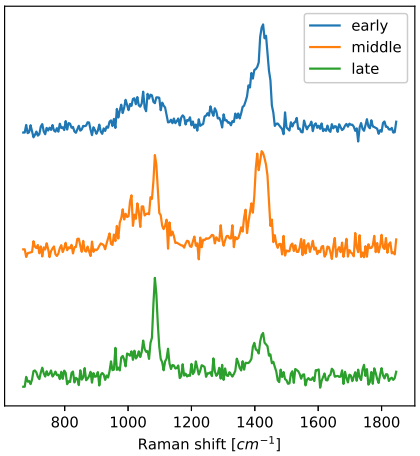	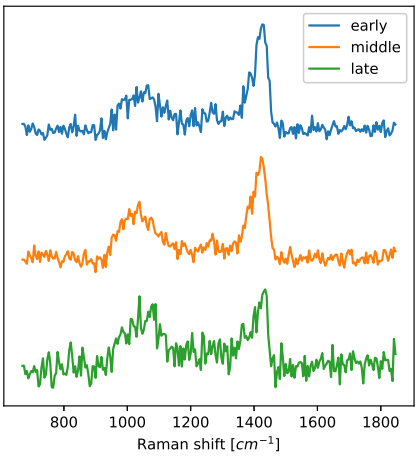
$\mu_s' = 15cm^{-1}$	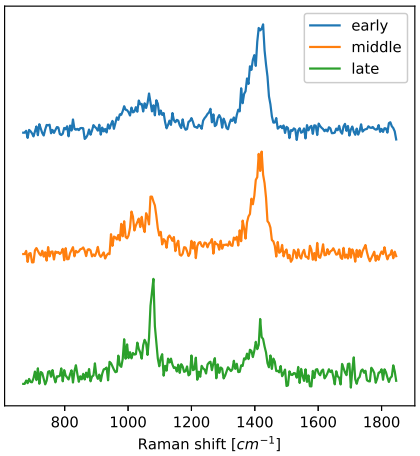	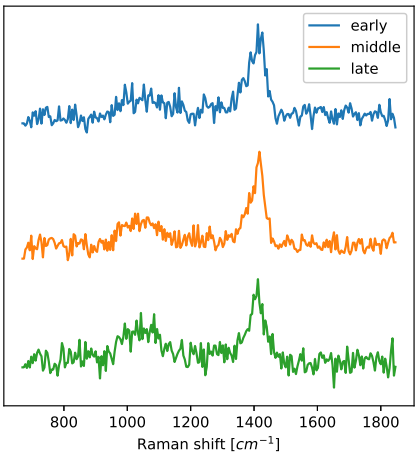

Table 4.3: Time gated bilayer measurements $\rho = 0$ (point-illumination)

	thickness = 0.5 cm	thickness = 1 cm
$\mu_s' = 5cm^{-1}$	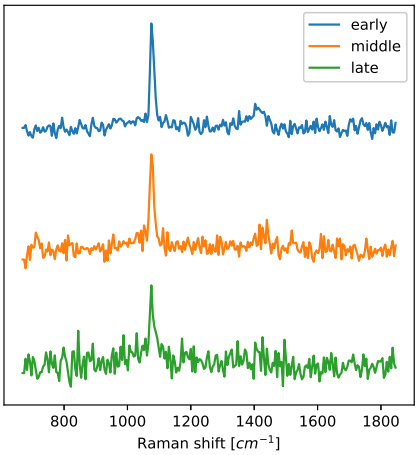	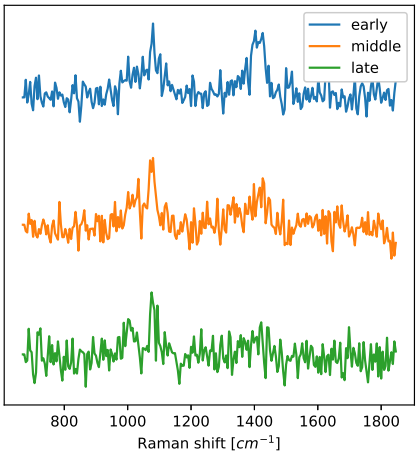
$\mu_s' = 10cm^{-1}$	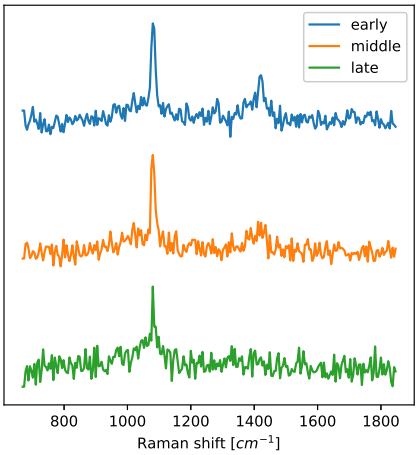	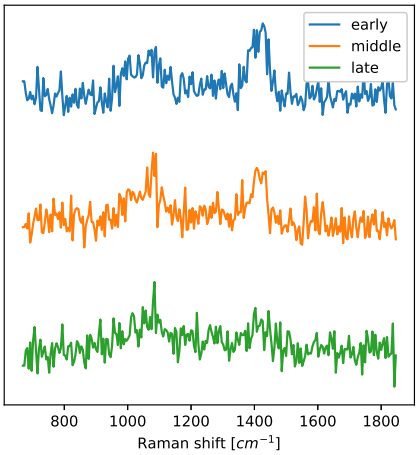
$\mu_s' = 15cm^{-1}$	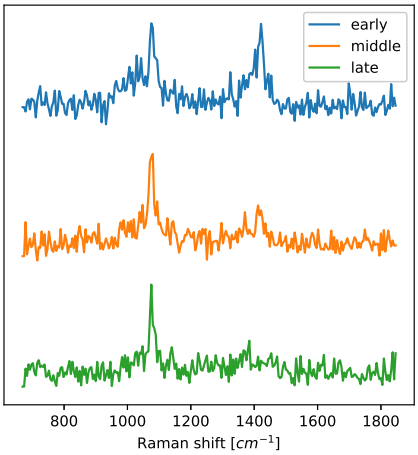	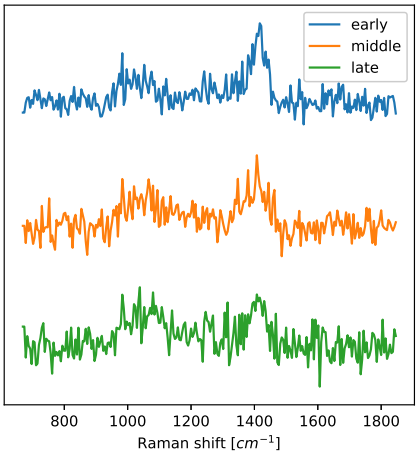

Table 4.4: Time gated bilayer measurements $\rho = 5mm$ (ring-illumination)

Looking at the figures in the tables 4.3 and 4.4 it is possible to see that our TD-DIRS spectrometer is actually capable of isolating the Raman signal coming from different depths of the sample thanks to time gating. In fact, in most of the graphs the spectrum obtained with the early time gate is characterized mostly by the contribution of the Raman peak of PDMS (top layer) while in the spectrum obtained with the late gate we can see mostly the contribution of the Raman peak of marble (bottom layer).
It is possible to note that all the other effects of the illumination scheme, the scattering coefficient of the top layer and the top layer thickness previously described are still valid. We can observe that in the cases of high scattering (10 cm^{-1}, 15 cm^{-1}) and large thickness (1 cm) the signal of the Raman peak is too low to be distinguishable. Maybe a increase of the time gate duration is needed in those cases to consider more signal and obtain a better spectrum. Moreover, in none of the measurements we have been able to completely isolate the spectrum of the top layer and the bottom layer one. Indeed, the time gates we chose are general and thought to fit to all measurements.
Nevertheless, if we consider a single measurement, the TCSPC acquisition allows us to select whatever time gate, so it is possible to find the best time gate to optimize the spectrum or to obtain a complete (or almost complete) isolation of the two spectra of the bilayer.

4.6. Interpretation of the bilayer measurements with the theoretical model

We will try in this section to use the calculations done about the generation depth of Raman photons to interpret the bilayer measurements. In particular our aim is to verify the link between the photon detection time and the average generation depth of detected Raman photons.
In order to experimentally distinguish the generation depth of Raman photons we will use the bottom layer. In fact, we know that photons generated for Raman scattering in the marble block can come only from a depth greater than the thickness of the top layer (silicone slab).
Our theoretical model requires the knowledge of the optical parameters of the top layer. For this reason, in order to be more precise, we measured the absorption and scattering coefficients of the silicone slabs used as samples with the instrumentation of reference [38]. In fact, the reference values of μ_a and μ_s' are valid only at a wavelength of 700 nm while our signal is at longer wavelengths (850 nm). The results obtained for each sample are shown in figure 4.11.

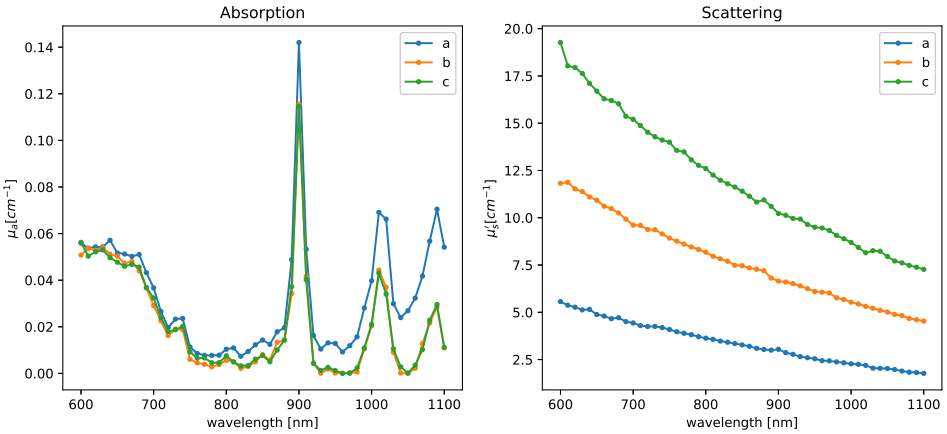

Figure 4.11: Absorption and scattering spectrum for the three silicone slab samples: (a) $\mu_s' = 5cm^{-1}$, (b) $\mu_s' = 10cm^{-1}$, (c) $\mu_s' = 15cm^{-1}$

We will use then in our calculations $\mu_a = 0.01$ cm^{-1} and $\mu_s = (3.5, 7.5, 11.5)$ cm^{-1}.
These parameters allow obtaining three probability distributions for the generation depth of Raman photons, each one refers to a different scattering coefficient and equivalently to a different sample. With these probability functions it is possible to calculate the average generation depth of Raman photons in function of the detection time for each sample. The results are shown in table 4.5.

Note that from these graphs we can see some confirmations to the explanations about the effect of the top layer scattering coefficient reported in section 4.5. In fact, it is clear that increasing the scattering coefficient the probability function shifts towards smaller values of depth: meaning that we will have a greater contribution of the superficial layers on the detected photons as we have seen in experimental measurements.
However, in order to better compare the theoretical model with the experimental measurements, also with a quantitative approach, we simulated each measurement with the same procedure followed in section 2.2 and we analyzed the obtained time evolution after its convolution with the temporal instrument response function (detected laser pulse shape).
In tables 4.6 and 4.7 each experimental measurement is placed side by side to the corresponding simulation. Every temporal curve is normalized so to cancel the differences in peak intensities and concentrate on the temporal shape.

	probability function	average depth
$\mu_s' = 5cm^{-1}$	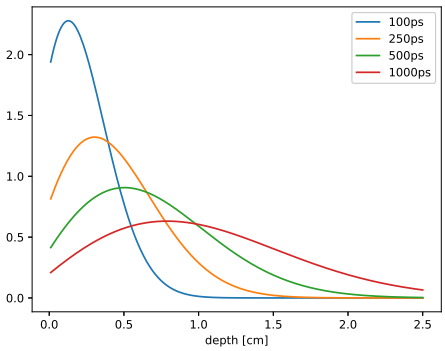	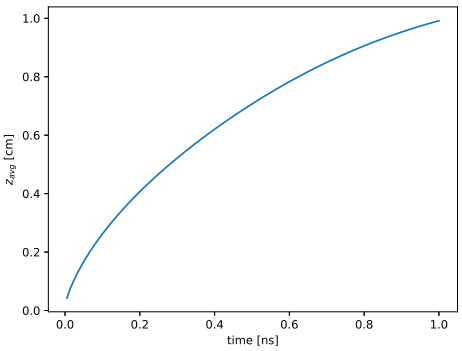
$\mu_s' = 10cm^{-1}$	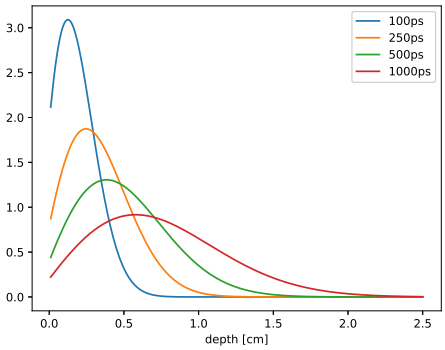	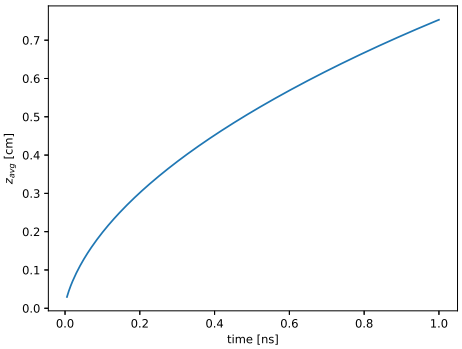
$\mu_s' = 15cm^{-1}$	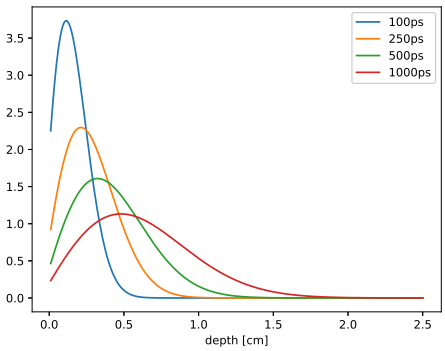	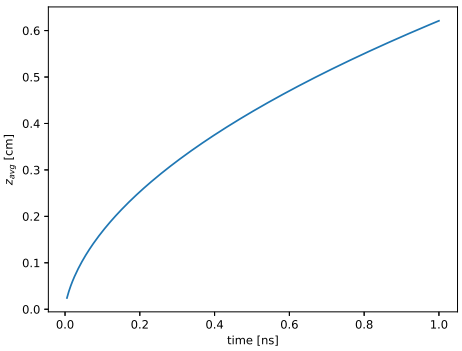

Table 4.5: Probability density functions and average generation depth for each sample

	experimental	simulation
$\mu_s' = 5cm^{-1}$	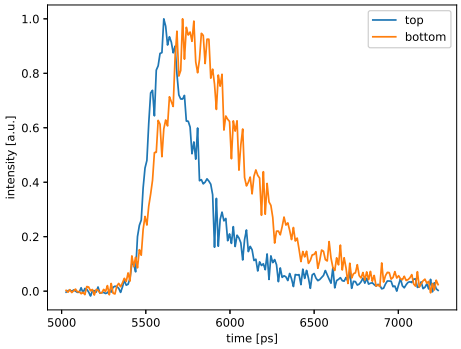	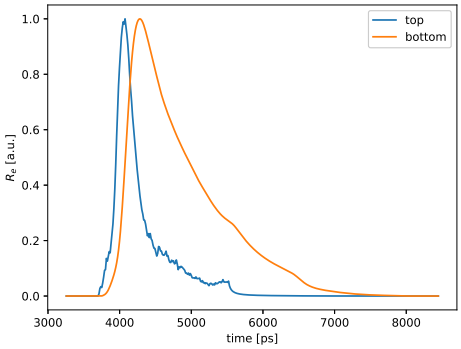
$\mu_s' = 10cm^{-1}$	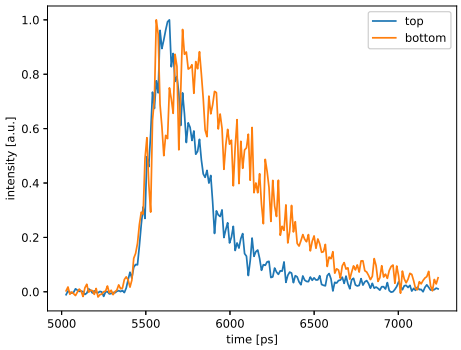	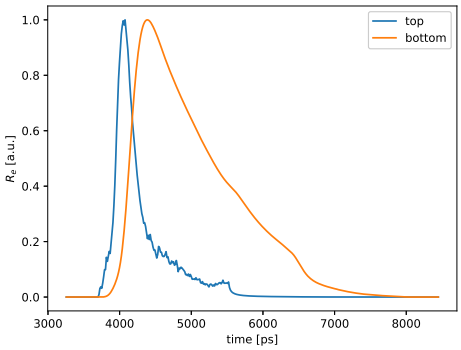
$\mu_s' = 15cm^{-1}$	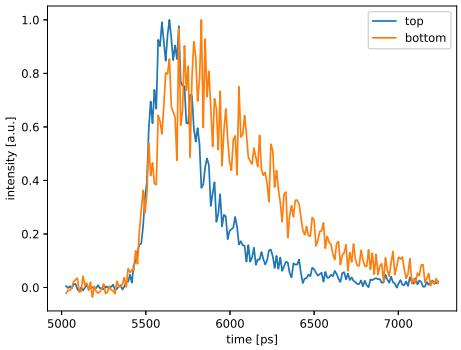	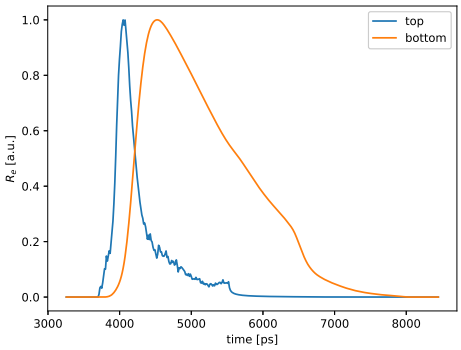

Table 4.6: Comparison between experimental measurements and simulations (top layer thickness = 0.5 cm)

	experimental	simulation
$\mu_s' = 5cm^{-1}$	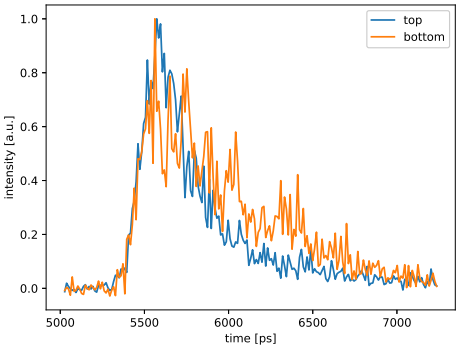	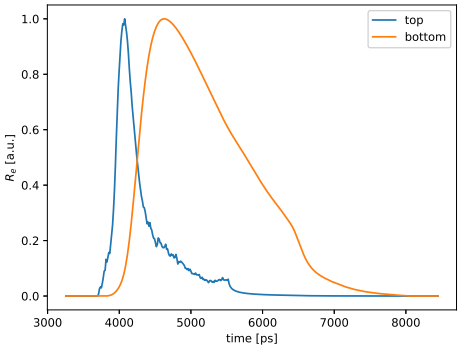
$\mu_s' = 10cm^{-1}$	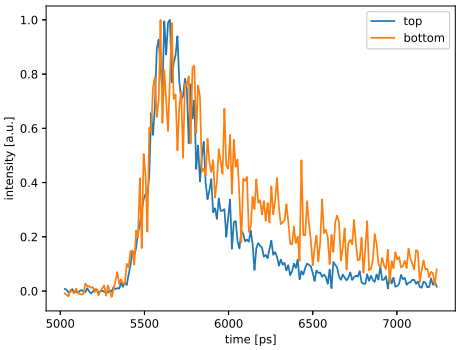	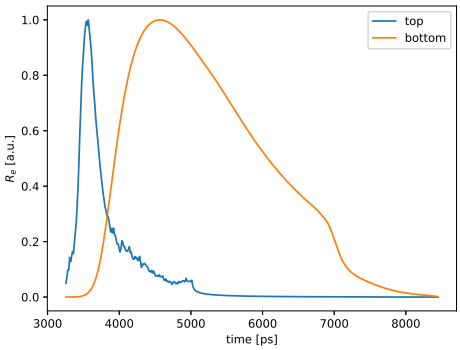
$\mu_s' = 15cm^{-1}$	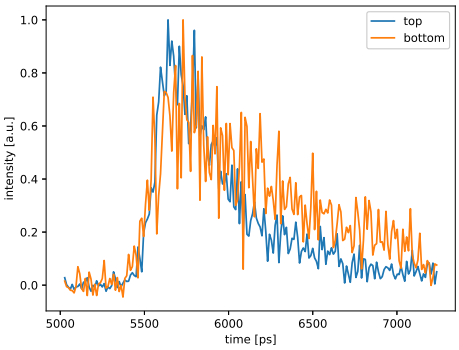	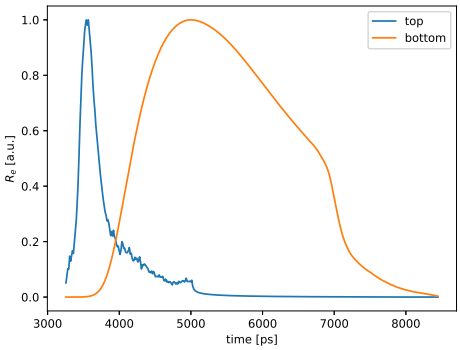

Table 4.7: Comparison between experimental measurements and simulations (top layer thickness = 1 cm)

From a qualitative point of view, it can be noted that the simulations reproduce well the time evolution of the signal. In fact, we see the presence, both in simulations and in experimental data, of a delay between the bottom layer signal and the top layer one and of a time in which the signal of the bottom layer starts to prevail with respect to the signal of the top layer.
From a quantitative point of view, we had to choose a parameter to do a fair comparison between the experimental measurements and the simulations. We decided to use the temporal distance between the barycenter of the top layer signal and the barycenter of the bottom layer signal. Indeed, this parameter, is insensible to the differences in intensities of the signals due to the effect of non-flat spectral efficiency. The obtained values are reported in table 4.8.

	thickness = 0.5 cm		**thickness = 1 cm**	
$\mu_s'[cm^{-1}]$	$\Delta t_{exp}[ps]$	$\Delta t_{sim}[ps]$	$\Delta t_{exp}[ps]$	$\Delta t_{sim}[ps]$
5	231	540	259	779
10	240	658	288	968
15	279	755	325	1100

Table 4.8: Differences between the barycenter position of bottom layer and top layer

It is possible to see that the theoretical model overestimates the analyzed time difference in all cases. In fact, superimposing a simulation to a experimental measurement we observe that the simulation gives a longer delay and a higher tail in the bottom layer signal than those observed.

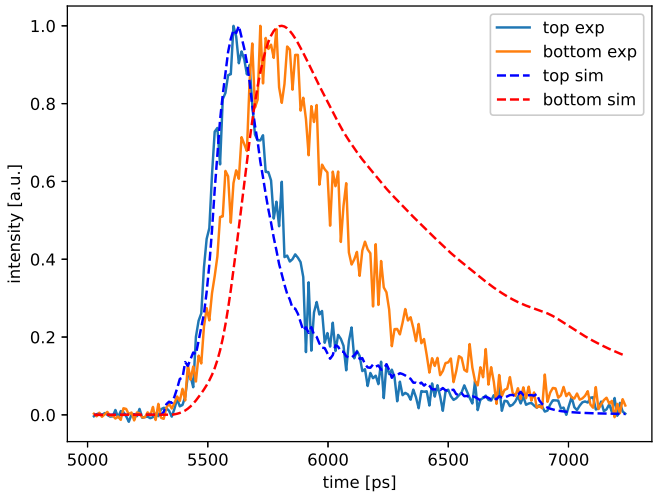

Figure 4.12: Superposition of a simulation to a experimental measurement $\mu_s' = 5cm^{-1}$, top layer thickness = 0.5 cm

However, it must be considered that our model adopts a big approximation which does

not reflect the reality: we are modelling the sample as a homogeneous medium so we are not considering the interface between top layer and bottom layer and the difference of optical properties of the two media. Hence, the discrepancies between the experimental measurements and the simulations are probably due to this approximation.
In conclusion, we can affirm that our developed theoretical model could be plausible as, although the quantitative differences, it predicts the correct behavior of the Raman signal. Nevertheless, we cannot declare its validity since our experimental data are not sufficient. We should in fact have had data for more values of the top layer thickness in order to make a more complete comparison but this was not possible due to the unavailability of such samples and because for large thicknesses of the top layer the signal is too low to give reliable values.

4.7. In vivo measurements

Since the ultimate goal of our instrumentation is its application for in vivo measurements, as final experiment with our instrumentation, we tested if it was possible to do an in vivo measurement of bone tissue. In fact, in principle, thanks to TD-DIRS we could be able to isolate the Raman spectrum of hydroxyapatite contained in bone tissue in a non-invasive through-skin measurement.
We took then a measurement on a finger with a point illumination scheme. The choice of this sample is not casual but stems from the consideration that the skin layer on a finger is very thin and should allow an easy detection of the bone tissue underneath. Moreover, the same measurement has been demonstrated to give successful results with SORS technique [39].
The measurement parameters were: multiplex mode with 256 Hadamard bases, 5 repetitions with a single pattern exposure time of 0.5 s for a total measurement time of 10.5 minutes. The laser power on the sample was of 50 mW distributed over a spot with a radius of 0.5 cm in order to avoid damages to the skin.
The results obtained are shown in figure 4.13.

We can see that, considering the non-uniform spectral efficiency (figure 3.21), the obtained spectrum is flat and no narrow Raman peak of hydroxyapatite is visible, even in the 2d map. This fact is due to the presence of fluorescence which covers the Raman signal hindering its detection. However, in this case it is more difficult to suppress fluorescence with the method discussed in section 4.4: even by time gating, we have not been able to see some signal of the Raman peak of bone tissue. Indeed, on the time scale there will be a Raman signal from the top layer followed by a Raman signal from the bottom layer

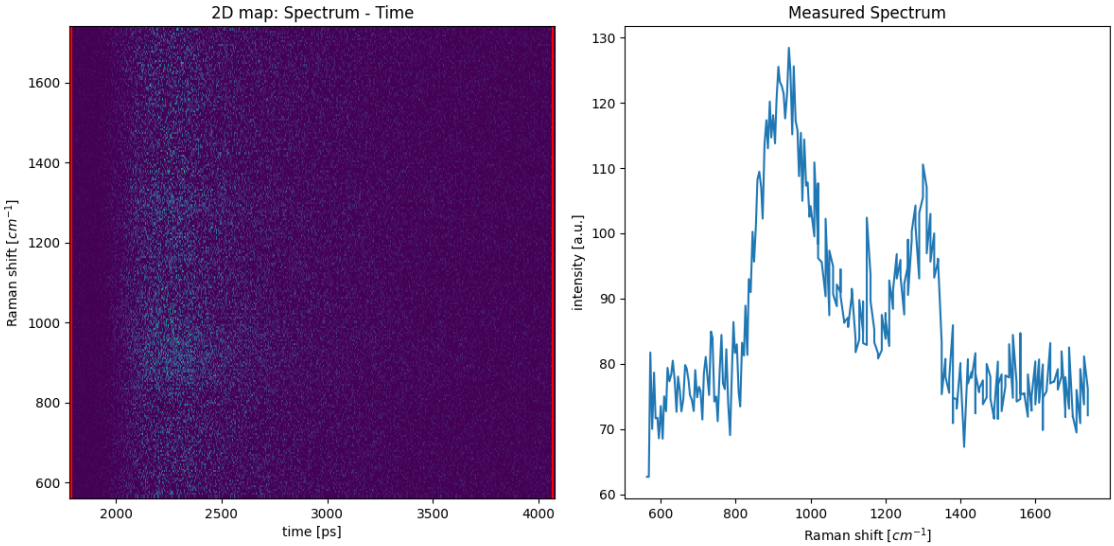

Figure 4.13: In vivo measurement of bone tissue

and a fluorescence signal, all mixed up by the effect of scattering. So, the Raman signal of the bone tissue it is expected to be completely hidden in the fluorescence signal.
In addition, the low detected intensity due to the low illumination power worsens the signal which is affected by visible noise.
In conclusion, our instrument is not still ready to be used for in vivo measurements.

5 | Conclusions

All the works faced during this thesis produced some interesting and new results we will now collect and summarize in this chapter.

Concerning the work on the theoretical models for the description of Diffuse Raman, we were able to find a new approach which allowed us to calculate the probability density function of detected Raman photons with respect to their generation depth and detection time and to determine the average generation depth of detected Raman photons with respect to their detection time. Moreover, with this model we managed to obtain the simulation of a measurement on a bilayered sample. The results obtained are qualitatively consistent with our expectations and experimental observations.

Concerning the instrumentation, we were able to bring some improvements which made easier its usability and increased its precision. In particular, we introduced a new operation mode (imaging mode) and we integrated all the program code needed to set up, run and reconstruct a measure in a single software with a nearly real time response (refresh rate 0.3 Hz). Both these functions allowed to reach a better alignment of the spectrometer and a resolution of 0.8 nm.

Concerning the experimental measurements, we were able to measure monolayered samples and bilayered samples. In the case of monolayered samples we successfully obtained the Raman spectrum in most of the measurements. Moreover, measuring a raw bone, we observed the capability of time gating in rejecting part of the fluorescence covering Raman signal. In the case of bilayered samples we encountered some difficulties due to the low detected signal, however, we managed to observe the effect of some experimental variables (source-detector distance, scattering coefficient, thickness of the top layer and time gating) on the measurement itself. In addition, by comparing the bilayer measurements with the simulations obtained from the theoretical model we could affirm that the results are qualitatively the same but we have some quantitative differences between the simulations and the experimental data.

In light of these results we can identify some future perspectives:

- Validation of our theoretical model: our theoretical model for the determination of the generation depth of Raman photons could be verified with Monte Carlo simulations or/and better experimental measurements and eventually refined by removing some approximations in order to simulate more realistic situations
- Improvement of the system: the instrumentation could be further improved with the aim of obtaining a flatter spectral efficiency and a higher detected signal. In particular, this last goal is the most critical since, if reached, enables to obtain better measurements and eventually decrease the measurement time. A higher detected signal could be obtained by means of an optimization of the collection optics. However, this optimization is not immediate since it has to be done considering the generation and propagation of Raman photons inside the sample until its surface
- Investigations on fluorescence rejection by time gating: a further analysis about the rejection of fluorescence could be done in order to find a method for suppression of fluorescence in the case of bilayered samples and isolate the Raman spectrum. This study is also useful for the in vivo application of the system
- In vivo application: this is the ultimate goal of our system, however, in order to reach it we must overcome the obstacles of the low detected signal and of the presence of fluorescence. Once we have done it, it is likely that our system will be able to provide also in vivo measurement

Bibliography

[1] Irving J. Bigio and Sergio Fantini. *Quantitative Biomedical Optics: Theory, Methods, and Applications*. Cambridge Texts in Biomedical Engineering. Cambridge University Press, 2016.

[2] Fabrizio Martelli, Tiziano Binzoni, André Liemert, Samuele Del Bianco, and Alwin Kienle. *Light Propagation through Biological Tissue and Other Diffusive Media: Theory, Solutions, and Validations*. SPIE, 2022.

[3] P. Matousek, I. P. Clark, E. R.C. Draper, M. D. Morris, A. E. Goodship, N. Everall, M. Towrie, W. F. Finney, and A. W. Parker. Subsurface probing in diffusely scattering media using spatially offset raman spectroscopy. *Applied Spectroscopy*, 59:393–400, 2005.

[4] Pavel Matousek. Inverse spatially offset raman spectroscopy for deep noninvasive probing of turbid media. *Applied Spectroscopy*, 60:1341–1347, 8 2006.

[5] P. Matousek and A. W. Parker. Bulk raman analysis of pharmaceutical tablets. *Applied Spectroscopy*, 60:1353–1357, 12 2006.

[6] Nicholas Stone, Karen Faulds, Duncan Graham, and Pavel Matousek. Prospects of deep raman spectroscopy for noninvasive detection of conjugated surface enhanced resonance raman scattering nanoparticles buried within 25 mm of mammalian tissue. *Analytical Chemistry*, 82:3969–3973, 5 2010.

[7] Nicholas Stone, Marleen Kerssens, Gavin Rhys Lloyd, Karen Faulds, Duncan Graham, and Pavel Matousek. Surface enhanced spatially offset raman spectroscopic (sesors) imaging – the next dimension. *Chemical Science*, 2:776–780, 3 2011.

[8] Claudia Conti, Chiara Colombo, Marco Realini, Giuseppe Zerbi, and Pavel Matousek. Subsurface raman analysis of thin painted layers. *Applied Spectroscopy*, 68:686–691, 6 2014.

[9] Bernhard Zachhuber, Christoph Gasser, Engelene T.H. Chrysostom, and Bernhard

Lendl. Stand-off spatial offset raman spectroscopy for the detection of concealed content in distant objects. *Analytical Chemistry*, 83:9438–9442, 12 2011.

[10] Alejandra Arroyo-Cerezo, Ana M. Jimenez-Carvelo, Antonio González-Casado, Anastasios Koidis, and Luis Cuadros-Rodríguez. Deep (offset) non-invasive raman spectroscopy for the evaluation of food and beverages – a review. *LWT*, 149:111822, 9 2021.

[11] William Parker. Scanner for spatially offset raman spectroscopy. *US Patent: US9880099B2*, 2018.

[12] Sanathana Konugolu Venkata Sekar, Sara Mosca, Andrea Farina, Fabrizio Martelli, Paola Taroni, Gianluca Valentini, Rinaldo Cubeddu, and Antonio Pifferi. Frequency offset raman spectroscopy (fors) for depth probing of diffusive media. *Optics Express*, 25, 3 2017.

[13] P Matousek, N Everall, M Towrie, and A W Parker. Depth profiling in diffusely scattering media using raman spectroscopy and picosecond kerr gating. *APPLIED SPECTROSCOPY*, 59, 2005.

[14] Freek Ariese, Heleen Meuzelaar, Marleen M. Kerssens, Joost B. Buijs, and Cees Gooijer. Picosecond raman spectroscopy with a fast intensified ccd camera for depth analysis of diffusely scattering media. *Analyst*, 134:1192–1197, 6 2009.

[15] S. Konugolu Venkata Sekar, S. Mosca, S. Tannert, G. Valentini, F. Martelli, T. Binzoni, Y. Prokazov, E. Turbin, W. Zuschratter, R. Erdmann, and A. Pifferi. Time domain diffuse raman spectrometer based on a tcspc camera for the depth analysis of diffusive media. *Opt. Lett.*, 43(9):2134–2137, May 2018.

[16] Jere Kekkonen, Jan Nissinen, and Ilkka Nissinen. Depth analysis of semi-transparent media by a time-correlated cmos spad line sensor-based depth-resolving raman spectrometer. *IEEE Sensors Journal*, 19:6711–6720, 8 2019.

[17] M. Lacerenza, S. K. V. Sekar, A. Farina, G. Valentini, C. D'Andrea, and A. Pifferi. Compressive sensing time-domain raman spectrometer for depth sensing of diffusive media. In *Clinical and Preclinical Optical Diagnostics II*, pages 11074–103. Optica Publishing Group, 2019.

[18] Ingeborg E. Iping Petterson, Patrick Dvoák, Joost B. Buijs, Cees Gooijer, and Freek Ariese. Time-resolved spatially offset raman spectroscopy for depth analysis of diffusely scattering layers. *Analyst*, 135:3255–3259, 11 2010.

[19] Fay Nicolson, Moritz F. Kircher, Nick Stone, and Pavel Matousek. Spatially offset

raman spectroscopy for biomedical applications. *Chemical Society Reviews*, 50:556–568, 1 2021.

[20] Matthew Bloomfield, Darren Andrews, Paul Loeffen, Craig Tombling, Tim York, and Pavel Matousek. Non-invasive identification of incoming raw pharmaceutical materials using spatially offset raman spectroscopy. *Journal of Pharmaceutical and Biomedical Analysis*, 76:65–69, 3 2013.

[21] Charlotte Eliasson and Pavel Matousek. Noninvasive authentication of pharmaceutical products through packaging using spatially offset raman spectroscopy. *Analytical Chemistry*, 79:1696–1701, 2 2007.

[22] William J. Olds, Shankaran Sundarajoo, Mark Selby, Biju Cletus, Peter M. Fredericks, and Emad L. Izake. Noninvasive, quantitative analysis of drug mixtures in containers using spatially offset raman spectroscopy (sors) and multivariate statistical analysis. *Applied Spectroscopy*, 66:530–537, 5 2012.

[23] Nirzari Gupta, Jason D. Rodriguez, and Huzeyfe Yilmaz. Through-container quantitative analysis of hand sanitizers using spatially offset raman spectroscopy. *Communications Chemistry 2021 4:1*, 4:1–9, 9 2021.

[24] Jason Guicheteau and Rebecca Hopkins. Applications of spatially offset raman spectroscopy to defense and security. *SPIE*, 9824:98240G, 5 2016.

[25] Adam P. Lister, William J. Sellors, Chris R. Howle, and Sumeet Mahajan. Raman scattering techniques for defense and security applications. *Analytical Chemistry*, 93:417–429, 1 2021.

[26] C. Conti, A. Botteon, C. Colombo, D. Pinna, M. Realini, and P. Matousek. Advances in raman spectroscopy for the non-destructive subsurface analysis of artworks: Microsors. *Journal of Cultural Heritage*, 43:319–328, 5 2020.

[27] Fabrizio Martelli, Tiziano Binzoni, Sanathana Konugolu Venkata Sekar, Andrea Farina, Stefano Cavalieri, and Antonio Pifferi. Time-domain raman analytical forward solvers. *Optics Express*, 24, 9 2016.

[28] Neil Everall, Thomas Hahn, Pavel Matousek, Anthony W. Parker, and Michael Towrie. Picosecond time-resolved raman spectroscopy of solids: Capabilities and limitations for fluorescence rejection and the influence of diffuse reflectance. *Applied Spectroscopy*, 55:1701–1708, 12 2001.

[29] Fabrizio Martelli, Tiziano Binzoni, Antonio Pifferi, Lorenzo Spinelli, Andrea Farina,

and Alessandro Torricelli. There's plenty of light at the bottom: statistics of photon penetration depth in random media. *Scientific Reports 2016 6:1*, 6:1–14, 6 2016.

[30] Antonio Pifferi and Martino Travagnin. *Sviluppo e caratterizzazione di un laser a titanio in zaffiro in regime continuo e di mode locking.* Tesi di Laurea, 1991.

[31] Pascal Berto, Camille Scotté, Frédéric Galland, Hervè Rigneault, and Hilton B. de Aguiar. Programmable single-pixel-based broadband stimulated raman scattering. *Optics Letters*, 42:1696, 5 2017.

[32] Marco F. Duarte, Mark A. Davenport, Dharmpal Takbar, Jason N. Laska, Ting Sun, Kevin F. Kelly, and Richard G. Baraniuk. Single-pixel imaging via compressive sampling: Building simpler, smaller, and less-expensive digital cameras. *IEEE Signal Processing Magazine*, 25:83–91, 2008.

[33] Graham M Gibson, Steven D Johnson, and Miles J Padgett. Single-pixel imaging 12 years on: a review. *Optics Express*, 28:28190, 2020.

[34] W. Becker. *The bh TCSPC handbook (9th edition).* available on www.becker-hickl.com, 2021.

[35] Wen Kai Yu. Super sub-nyquist single-pixel imaging by means of cake-cutting hadamard basis sort. *Sensors 2019, Vol. 19, Page 4122*, 19:4122, 9 2019.

[36] Texas Instruments. *DLPC900 Programmer's Guide*, 2022.

[37] Python/c api reference manual. `https://docs.python.org/3/c-api/index.html`.

[38] Sanathana Konugolu Venkata Sekar, Alberto Dalla Mora, Ilaria Bargigia, Edoardo Martinenghi, Claus Lindner, Parisa Farzam, Marco Pagliazzi, Turgut Durduran, Paola Taroni, Antonio Pifferi, and Andrea Farina. Broadband (600-1350 nm) time-resolved diffuse optical spectrometer for clinical use. *IEEE Journal of Selected Topics in Quantum Electronics*, 22:406–414, 5 2016.

[39] Pavel Matousek, Edward R C Draper, Allen E Goodship, Ian P Clark, Kate L Ronayne, Anthony W Parker, and A W P Royal. Noninvasive raman spectroscopy of human tissue in vivo. *Applied Spectroscopy*, 60:758–763, 2006.

List of Figures

List of Tables